AD-774 022

STUDY OF LASER-IRRADIATED THIN FILMS

Larry G. DeShazer, et al

University of Southern California

Prepared for:

Air Force Cambridge Research Laboratories
Defense Advanced Research Projects Agency

August 1973

The views and conclusions contained in this document are those of the authors and should not be interpreted as necessarily representing the official policies, either expressed or implied, of the Defense Advanced Research Projects Agency, the United States Air Force, or the United States Government.

AD 774022

DOCUMENT CONTROL DATA - R & D

(Security classification of title, body of abstract and indexing annotation must be entered when the overall report is classified)

1 ORIGINATING ACTIVITY (Corporate author)	2a. REPORT SECURITY CLASSIFICATION
Electronics Sciences Laboratory University of Southern California Los Angeles, California 90007	UNCLASSIFIED
	2b. GROUP N/A

3 REPORT TITLE

STUDY OF LASER-IRRADIATED THIN FILMS

4 DESCRIPTIVE NOTES (Type of report and inclusive dates)

Scientific.   Final.

Approved
12 October 1973

5 AUTHOR(S) (First name, middle initial, last name)

Larry G. DeShazer   Brian E. Newnam
Kang M. Leung   Nabil Al-assini

6 REPORT DATE	7a. TOTAL NO OF PAGES	7b. NO OF REFS
August, 1973	130	42

8a. CONTRACT OR GRANT NO ARPA Order	9a. ORIGINATOR'S REPORT NUMBER(S)
F 19628-71-C-0220 No. 1738	
b. PROJECT NO Task, Work Unit Nos.	USCEE Report 461
c. 1738 n/a n/a DoD Element 61101D	9b. OTHER REPORT NO(S) (Any other numbers that may be assigned this report)
d. DoD Subelement n/a	AFCRL-TR-73-0585

10 DISTRIBUTION STATEMENT

A - Approved for public release; distribution unlimited.

11 SUPPLEMENTARY NOTES	12 SPONSORING MILITARY ACTIVITY
This research was supported by the Defense Advanced Research Projects Agency	Air Force Cambridge Research Laboratories (OP) L.G. Hanscom Field Bedford, Massachusetts 01730

13 ABSTRACT

Laser-induced structural damage to dielectric thin-film coatings was investigated using a TEM_{00} Q-switched ruby laser. This study included mono-, bi-, and multi-layered coatings of the materials TiO_2, SiO_2, ZrO_2, MgF_2, and ZnS on substrates of glass, fused silica, rocksalt and spinel. The samples included coatings for antireflection and reflection at the ruby wavelength and were produced either at USC or by a commercial vendor. Damage threshold energy densities were measured with attention paid to dependences on laser beam spot-size, film material and thickness, substrate condition and incipient scattering of the film. Two major facts about laser damage to thin films were discovered. One fact is that laser-induced scatter, indicative of film break-up, is observed prior to the threshold of spark formation at the film. The other fact is that the damage threshold of the thin-film increases as the laser beam spot-size decreases. A theoretical model was developed which correlated the nature and distribution of coating defects to this spot-size dependence.

DD FORM 1473
NOV 65

KEY WORDS	LINK A		LINK B		LINK C	
	ROLE	WT	ROLE	WT	ROLE	WT
Coating defects						
Damage morphology						
Damage thresholds						
Defect damage						
Defect model						
Electric-field distribution						
Intrinsic damage						
Laser-induced damage						
Laser-induced scatter						
Linear absorption						
Thin film damage						
Truncated gaussian beam optics						

ABSTRACT

Laser-induced structural damage to dielectric thin-film coatings was investigated using a TEM_{00} Q-switched ruby laser. This study included mono-, bi-, and multi-layered coatings of the materials TiO_2, SiO_2, ZrO_2, MgF_2, and ZnS on substrates of glass, fused silica, rocksalt and spinel. The samples included coatings for antireflection and reflection at the ruby wavelength and were produced either at USC or by a commercial vendor. Damage threshold energy densities were measured with attention paid to dependences on laser beam spot-size, film material and thickness, substrate condition and incipient scattering of the film. Two major facts about laser damage to thin films were discovered. One fact is that laser-induced scatter, indicative of film break-up, is observed prior to the threshold of spark formation at the film. The other fact is that the damage threshold of the thin-film increases as the laser beam spot-size decreases. A theoretical model was developed which correlated the nature and distribution of coating defects to this spot-size dependence.

FORWARD

This scientific report describes work performed under
Contract No. 19628-71-C-0220 covering the period between May 14,
1971 and May 13, 1973.

This report was submitted by the authors on 3 September
1973.

TABLE OF CONTENTS

LIST OF FIGURES

LIST OF FIGURES--Continued

xiv

LIST OF TABLES

LIST OF TABLES--Continued

I. INTRODUCTION

Progress in the development and application of high
power lasers is presently limited by catastrophic material failure
induced by laser radiation. Since 1969 an annual symposium,
"Damage in Laser Materials," has been held at the National Bureau
of Standards in Boulder, Colorado and much effort has been directed
towards understanding laser-induced damage processes in transparent
dielectrics. Experiments typically use an intense laser beam, pro-
duced by a high power solid state laser with monitored beam char-
acteristics, to strike a small area of the tested sample. Measure-
ments of damage threshold, in terms of either power density or
energy density for different optical materials, are obtained by using
various diagnostic techniques for the detection. The most frequently
tested specimens are ruby, glass, nonlinear optical crystals, dielec-
tric thin film coatings and ir windows. In solid state laser hosts,
there has been substantial progress in understanding the physics of
damage and in most cases, it can be reduced to a problem of
quality control. However, for dielectric thin-film coatings, the
understanding of the damage mechanisms is tentative and speculative.
As a result, dielectric thin-film coatings are presently one of the
weaker components of high-power laser systems.

The present work has been concerned with the problem
of developing reliable diagnostic tools to study laser-induced damage
phenomena in dielectric thin film coatings, and to understand these
damage processes in terms of some important physical parameters.
The primary purpose of this exploratory research was not so much
to find new coating materials with high damage thresholds, but to
obtain accurate measurements of the thresholds of the best materials
presently used in various coating configurations and with various
laser irradiation conditions. By examining these thresholds for
correlations with the film properties or laser parameters, it was

1.

hoped that the causes of the damage might be revealed.

It was noted in the laser literature that a great amount of the past experimental data were generated with laser sources for which there was inadequate control or knowledge of the laser output, especially the transverse spatial profile of the intensity. At the early stage of this program, a careful generation and characterization of high power pulses from a ruby laser operating in a single transverse and longitudinal TEM_{00} mode was established. This laser was used to obtain accurate measurements, under well-defined conditions, of damage to thin film coatings. In addition, focusing of the single-mode pulses also required special analysis. Equipped with this well-controlled high-power tool, we have directed our attention to the definition of the threshold of damage for dielectric thin film coatings and several detection methods were evaluated. The damage thresholds of a selection of vacuum deposited coatings were measured as a function of several parameters of the laser beam and the coating materials. Many important and significant results were derived from this exploratory study.

In Section II, the experimental setup as well as the laser arrangement with its characteristics will be described. The truncated Gaussian optics related to the focusing beam of the single-mode laser will be also discussed. In addition, the preparation of test specimens which included mono-, bi-, and multi-layered vacuum-deposited coatings of the materials MgF_2, SiO_2, ZrO_2, TiO_2, ZnS, ThF_4 and CeO_2 on substrates of glass, fused silica, rock salt, and spinel will be presented.

One of the important aspects of this program has been the determination of a sensitive and reliable criterion for the onset of damage. We have used four types of detection methods for evaluation. They are: 1) photoelectric detection of the spark; 2) visual observation of laser-induced increases in the weak-signal film scatter; 3) microscopic observation of film breakup; and

I. INTRODUCTION

Progress in the development and application of high
power lasers is presently limited by catastrophic material failure
induced by laser radiation.   Since 1969 an annual symposium,
"Damage in Laser Materials," has been held at the National Bureau
of Standards in Boulder, Colorado and much effort has been directed
towards understanding laser-induced damage processes in transparent
dielectrics.   Experiments typically use an intense laser beam, pro-
duced by a high power solid state laser with monitored beam char-
acteristics, to strike a small area of the tested sample.   Measure-
ments of damage threshold, in terms of either power density or
energy density for different optical materials, are obtained by using
various diagnostic techniques for the detection.   The most frequently
tested specimens are ruby, glass, nonlinear optical crystals, dielec-
tric thin film coatings and ir windows.   In solid state laser hosts,
there has been substantial progress in understanding the physics of
damage and in most cases, it can be reduced to a problem of
quality control.   However, for dielectric thin-film coatings, the
understanding of the damage mechanisms is tentative and speculative.
As a result, dielectric thin-film coatings are presently one of the
weaker components of high-power laser systems.

The present work has been concerned with the problem
of developing reliable diagnostic tools to study laser-induced damage
phenomena in dielectric thin film coatings, and to understand these
damage processes in terms of some important physical parameters.
The primary purpose of this exploratory research was not so much
to find new coating materials with high damage thresholds, but to
obtain accurate measurements of the thresholds of the best materials
presently used in various coating configurations and with various
laser irradiation conditions.   By examining these thresholds for
correlations with the film properties or laser parameters, it was

1.

4) time-dependent observation of laser-induced damage phenomena.
In Section III, a detailed description of these methods and their eval-
uation will be given. Light scattering induced by a low intensity
laser (e.g. , a He-Ne laser) was the most sensitive sign of film
breakup for coatings of low initial scatter. A correlation between
the damage thresholds and diffuse weak-signal scattering of multilayer
reflectors was also established. Time-resolved measurements of
scatter have also shown that the thin-film damage occurred within
the laser pulsewidth of 20 nsec.

In the course of this study, the importance of the
electric field distributions of the tested specimens was demonstrated.
A computer program was set up to calculate the electric field dis-
tribution for all the thin film samples that were tested as discussed
in Section IV. The damage thresholds of thin films were strongly
dependent on the standing-wave patterns of the internal electric fields.
The entrance-face thresholds were equal to or greater than the exit-
face thresholds of thin films. Furthermore, when the laser beam is
incident at an oblique angle, calculation of field distribution indicates
that the power-density for the polarizations parallel and perpendicular
to the plane of incidence are substantially different.

In addition to the study of damage to entrance and
exit-face coatings, the damage threshold energy and power densities
were measured as a function of: (1) laser beam spot-size, (2) pulse-
width of laser beam, (3) transverse mode structure of laser beam,
(4) coating material, (5) single layer thickness of coating, (6) sub-
strate material and, (7) multilayer configuration. One of the most
important results in this study is that the damage threshold of the
thin film increases as the spot-size of the laser beam decreases.
The spot-size is the $1/e^2$ radius of the intensity profile of the TEM_{00}
ruby laser beam. A simple model has been developed in correlating
the nature and distribution of coating defects to this spot-size depen-
dence, e.g., the probability of the laser beam striking a defect site

will be greater for larger spot-sizes, while damage in materials can be distinguished as defect damage and intrinsic damage. The detailed account and experimental confirmation for this model can be found in Section V. Experimental results of other laser parameters discussed in Section VI are tentative.

The experimental results of damage thresholds on varying several coating parameters are given in Section VII. In testing single layer thin films, the damage thresholds for films with low refractive indices were greater than those for films with high indices at the ruby laser wavelength. The role of absorption as a damage mechanism was analyzed. It was suggested that linear absorption could raise the film temperature either to the melting point or to a value high enough to produce harmful thermostrictive forces. Section VIII summarizes some important findings of this program and some suggestions for further work in this research area are made.

II. EXPERIMENTAL PROCEDURES

1. Experimental Setup

In order to accurately interpret the results of experiments involving laser-induced damage, the temporal and spatial-intensity profiles of the laser pulse must be smooth and preferably Gaussian. Accordingly, a high power, passively Q-switched ruby laser oscillator and amplifier system was constructed which operated in a single longitudinal and transverse TEM_{00} mode. The time contour of the pulse was nearly Gaussian with pulsewidths (FWHM) from 9 to 35 nsec, and peak powers up to 10 MW when using the amplifier. The output characteristics of this laser system are listed in Table 1. The values given for the oscillator were determined at 100 cm (1.1 Rayleigh distances) from the oscillator aperture. For such Gaussian pulses, the peak power P_o is related to the total energy E by $P_o = (0.941E)/T$, where T is the full width of the pulse at half maximum. Absolute energy calibration was performed using a ballistic thermopile (TRG 100), and agreed to within 5% of the calibration of another thermopile used by C.R. Guiliano at Hughes Research Laboratories. In the far field of the laser oscillator, the spatial intensity profile of the beam was close to a Gaussian distribution, as determined by a pinhole scan. At the distance of 100 cm (1.1 Rayleigh distance) from the oscillator, the intensity distribution at the temporal peak of the pulse is shown in Figure 1. The amplified profile also had a similar near-Gaussian shape as shown in Figure 2.

For measuring damage thresholds of dielectric thin film coatings, the laser was arranged as shown in Figure 3. Most of the tests were performed with the output of the oscillator alone, since its spatial profile in the far field was near ideal for analytical computations. For time resolved measurements, another laser having similar output characteristics but with only the oscillator was setup

6.

NORMALIZED OSCILLATOR INTENSITY
DISTRIBUTION

N = 0.4
1.12 mm DIA. APERTURE
PINHOLE (63μ) SCAN
AT 100cm (1.1 R) IN
VERTICAL PLANE

$\frac{I_0}{e} = 0.4\,mm$

RADIAL DISTANCE (mm)

1.0

0.8

0.6

0.4

0.2

1.00   .75   .50   .25   0   .25   .50   .75   1.00
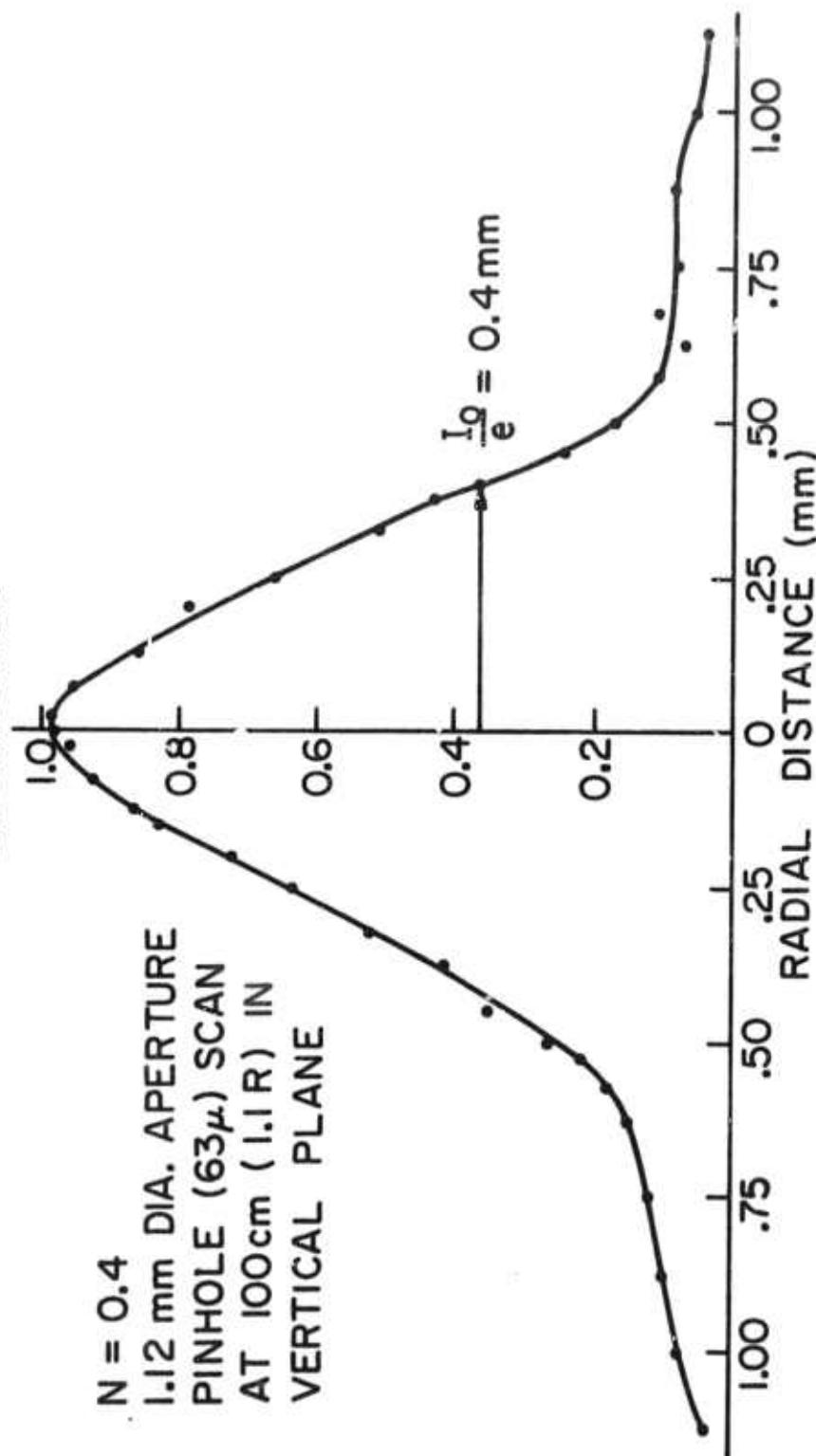
Figure 1. Normalized, transverse spatial-intensity distribution at 1.1 R (100 cm) from the aperture of the giant-pulse ruby laser oscillator with Fresnel number of 0.4.
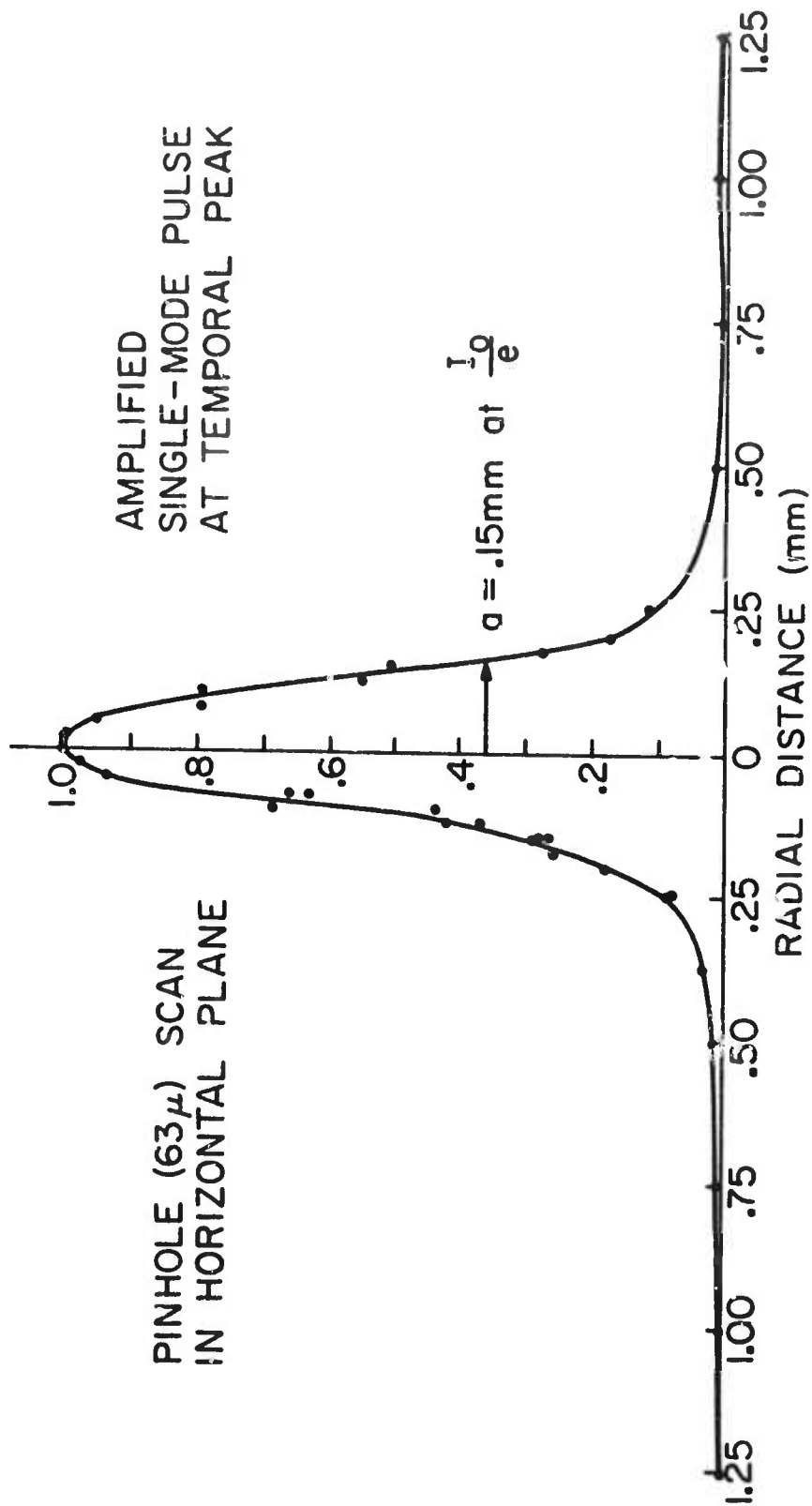
Fiture 2.   Normalized, transverse spatial-intensity distribution of the ruby amplifier.   The amplifier input face was at 2.2 R (200 cm) from the oscillator.
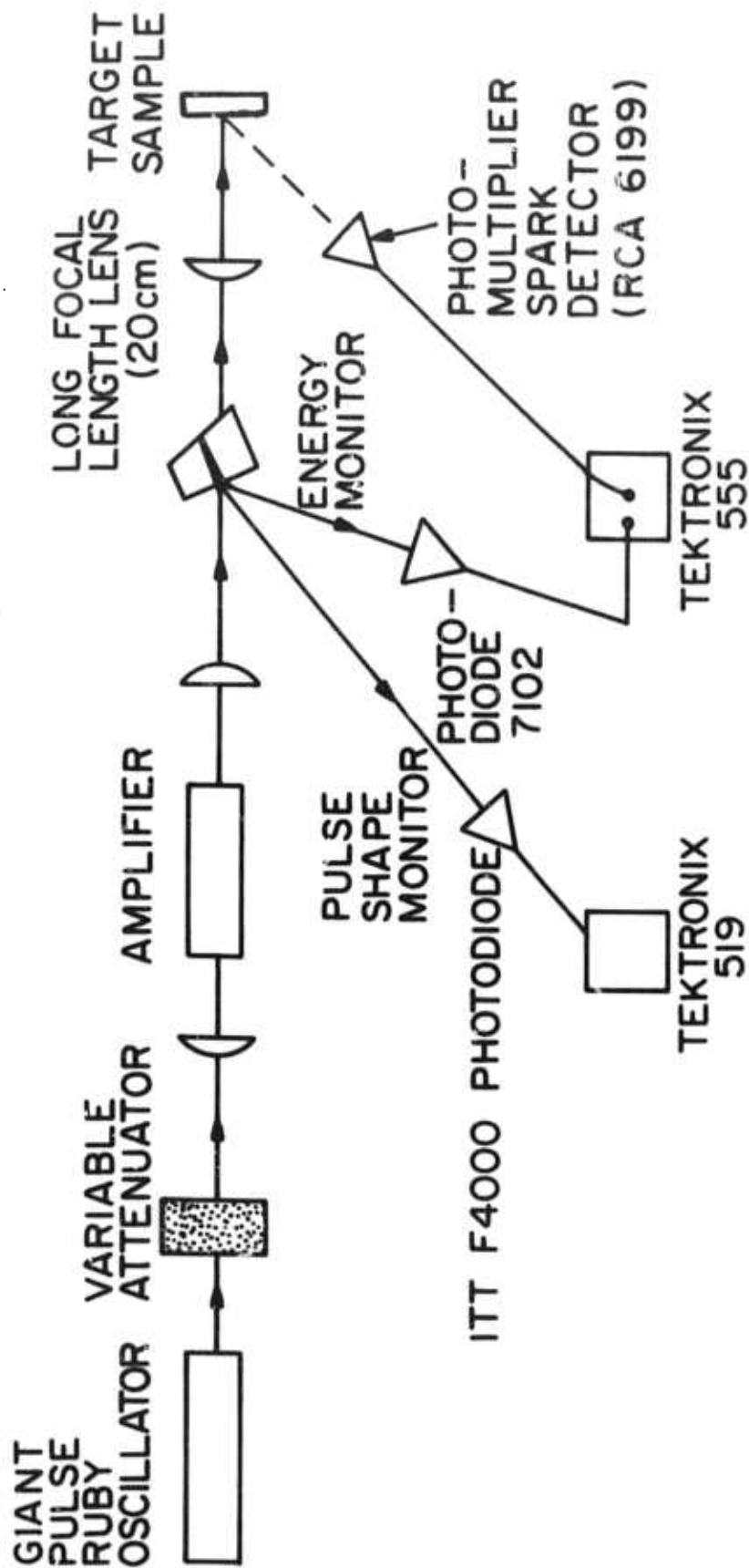
Figure 3. Schematic of the Q-switched ruby laser system and spark detection electronics for damage threshold measurements.

as shown in Figure 4. However, unless specified otherwise, our discussion will be mainly on the first experimental setup. The detailed operation of this apparatus was discussed at the Third ASTM-NBS Damage Symposium [1].

Table 1. Single-mode output of the ruby laser.

Parameter	Oscillator	Amplifier
Energy	5 - 7 mJ ($\pm$ 5%)	up to 120 mJ
Pulsewidth	~ 12 nsec	~ 12 nsec
Peak Power	0.4 - 0.6 MW	$\leq$ 10 MW
Divergence beam	1.1 mrad (full angle)	-----
Beam spot-size	0.62 $\pm$ 0.02 mm	-----
Peak energy density	0.8 - 1.2 J/cm^2	$\leq$ 100 J/cm^2
Peak power density	65 - 100 MW/cm^2	$\leq$ 10 GW/cm^2

2. Calibration and Truncated Gaussian Optics

The spatial intensity distribution of the laser beam cannot be exactly Gaussian since the single mode is coupled out of the laser oscillator through a circular aperture, resulting in the truncation of the aperture intensity illumination. This truncation produces rings in the far-field pattern and structure within the central disk in the near-field. Figure 5 shows the diffraction pattern of the laser oscillator in the far-field with three different exposures. The central disk is nearly Gaussian and in the over-
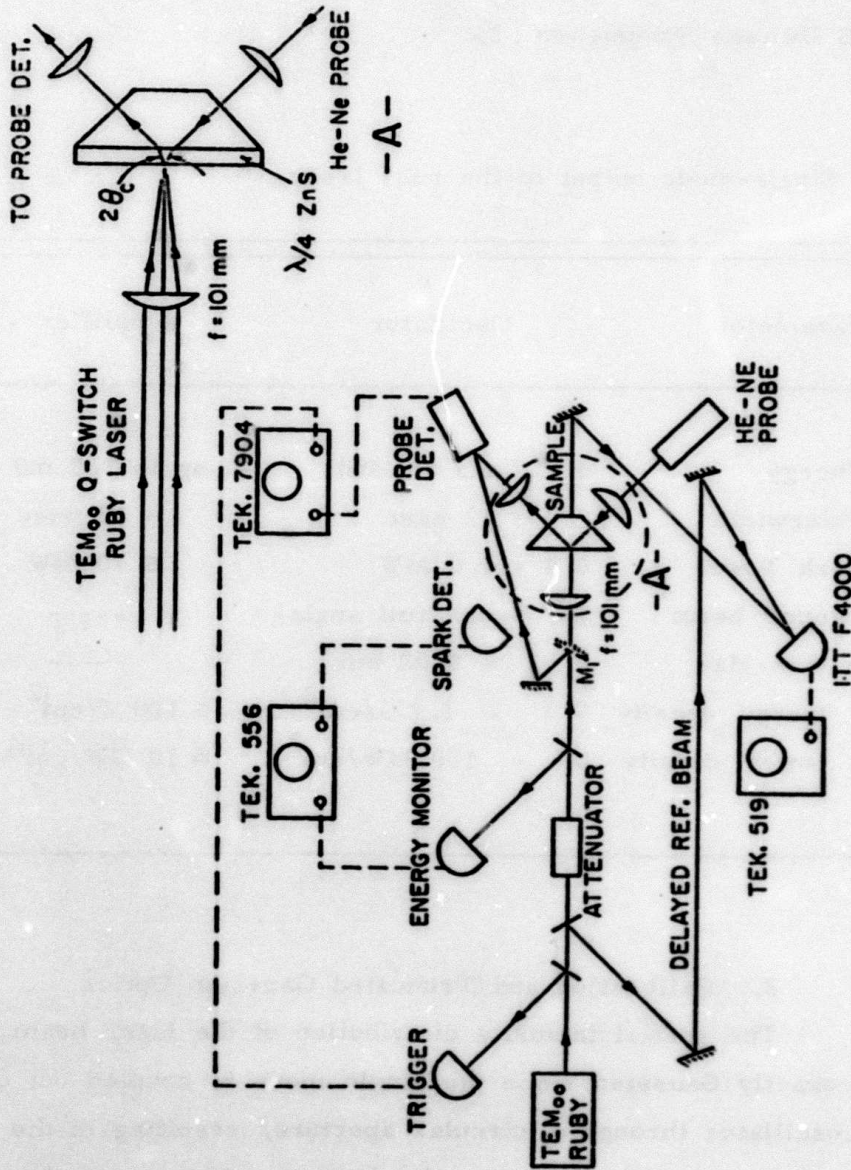
Figure 4. Schematic of the experimental setup for time resolution optical probe technique.
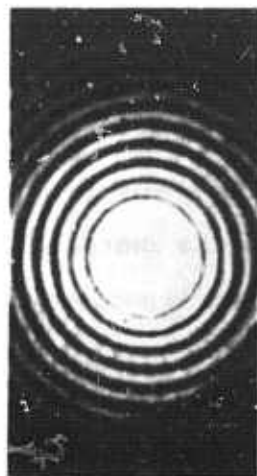
Figure 5. Photographs of the diffraction pattern of the giant-pulse ruby laser oscillator (N = 0.4) at 3.0 Rayleigh distances (far field) from the oscillator aperture. The three photographs were exposed under three different beam attenuations.

exposed pictures, the presence of the rings around the central disk
due to truncation is strikingly evident. Now, the importance of
recognizing the existence of truncation effects lies in the fact that,
if attention is not paid to these effects, calculations of the axial
intensity may be in error by as much as 100%. Such discrepancies
are particularly possible when truncated Gaussian beams are focused.

When a laser beam is focused by a lens the focused
intensities can be simply predicted only if the spatial profile of the
beam has the ideal Gaussian distribution [2]. Since an exactly
Gaussian beam remains Gaussian through out an optical system, only
the calculation of the spot-size of the Gaussian beam with respect to
the lens is required. The spot-size is the $1/e^2$ radius of the inten-
sity profile of a beam. The variation of the spot-size as the beam
propagates along the axis of the lens is controlled by the spot-size
w_o at the waist of the input beam and the distance d_1 of the input
waist from the lens as well as the geometric focal length F of the
lens. The geometry of the input beam to the lens is illustrated in
Figure 6, and the value of the spot-size w_2 at a distance d_2 from
the lens is determined from Eq. (1).

$$w_2 = w_o \frac{d_2}{d_1} \left(1 + \frac{b^2}{d_1^2}\right)^{-\frac{1}{2}} \sqrt{1 + \frac{d_1^4}{b^2} \left(1 + \frac{b^2}{d_1^2}\right)^2 \left(\frac{1}{d_2} - \frac{1}{F} + \frac{1}{d_1 [1 + (b^2/d_1^2)]}\right)^2} \qquad (1)$$

The parameter b is defined as $\pi w_o^2/\lambda$ where λ is the
laser wavelength. This Eq. (1) is the general expression giving
w_2 as a function of w_o, d_1 and F, and can be used to determine
the peak power and energy densities anywhere in a focused beam
provided the beam has an ideal Gaussian profile. Many experimenters
using single transverse-mode lasers generally assume that this
Gaussian description of focused beams applies to their laser setup.
Truncation of the Gaussian beam can severely alter this calculation,
though, and prevent a proper analysis of an experiment.
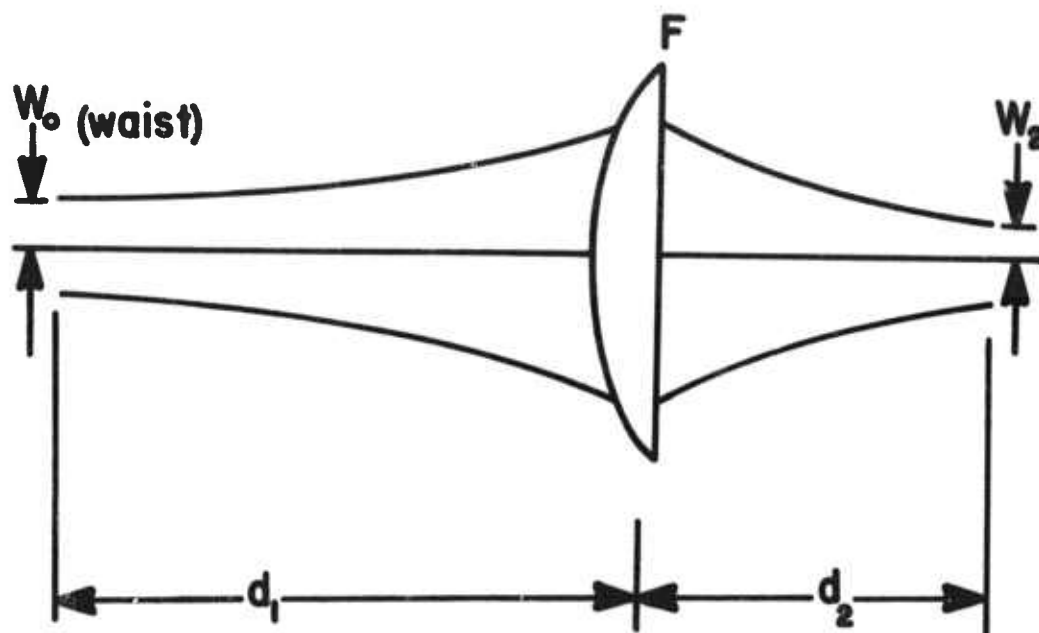
Figure 6. Focusing of a Gaussian beam.

Truncation of the Gaussian distribution, which is
infinite in extent, can never, of course, be avoided but is generally
unimportant in low-power lasers. In high-power Q-switched lasers
though, due to their resonator design requirements, the truncation
is usually not negligible. Figure 7 shows several possible intensity
distributions in the aperture plane of a laser oscillator having a
Fresnel number of 0. 4, the Fresnel number of our oscillator. The
profile for the fundamental stationary (Fox-Li) mode is a truncated
Gaussian having a truncation parameter of 0. 84. The truncation
parameter is the ratio of the radius of the truncating aperture a
to the spot-size w.   This Fox-Li profile is flattened by saturation
of the gain [3], which usually occurs in high-power pulsed lasers.
Three examples are shown for initial numerical gains of 20, 12. 2
and 7. 4, all calculated assuming a uniform initial gain distribution.
When the initial gain distribution is peaked symmetrically about the
resonator axis due to the design of a particular pumping scheme,
the Fox-Li profile is sharpened, increasing the truncation parameter.
A typical example of axisymmetric pumping is the elliptical focusing
of pump light into a cylindrical laser rod. For the laser oscillator
used in our investigations, the truncation parameter was near 0. 6.

Since Campbell and DeShazer [4] have shown that
diffraction effects due to truncation cannot be neglected when the
truncation parameter is less than 2. 0, the usual Gaussian description
of focused beams does not apply to our laser experiment. There-
fore, a calculation of focused truncated Gaussian beams is required
for the analysis. A formula has been published [5] for the intensity
variation along the optical axis for a special case of a truncated
Gaussian beam where the lens is also the aperturing element.
U. O. Farrukh [6] has calculated the diffraction effects of focused
truncated Gaussian beams for the more usual situation shown in
Figure 8. The source laser is represented by a collimated ideal
Gaussian beam of spot-size w, apertured by a diverging lens of
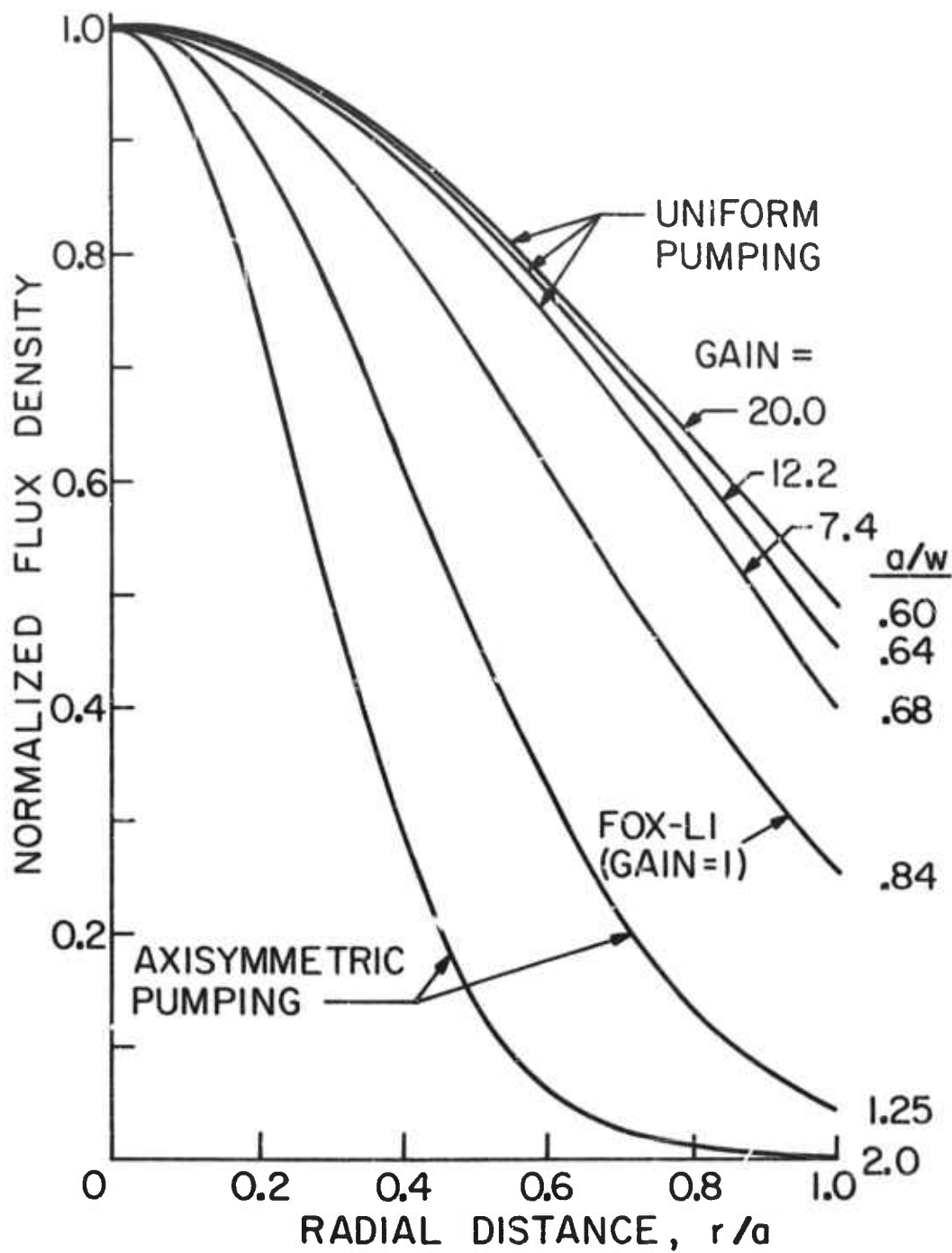
Figure 7. Aperture intensity profiles at the temporal peak
of a passively Q-switched ruby laser oscillator
with planar mirrors and Fresnel No. of 4.

16
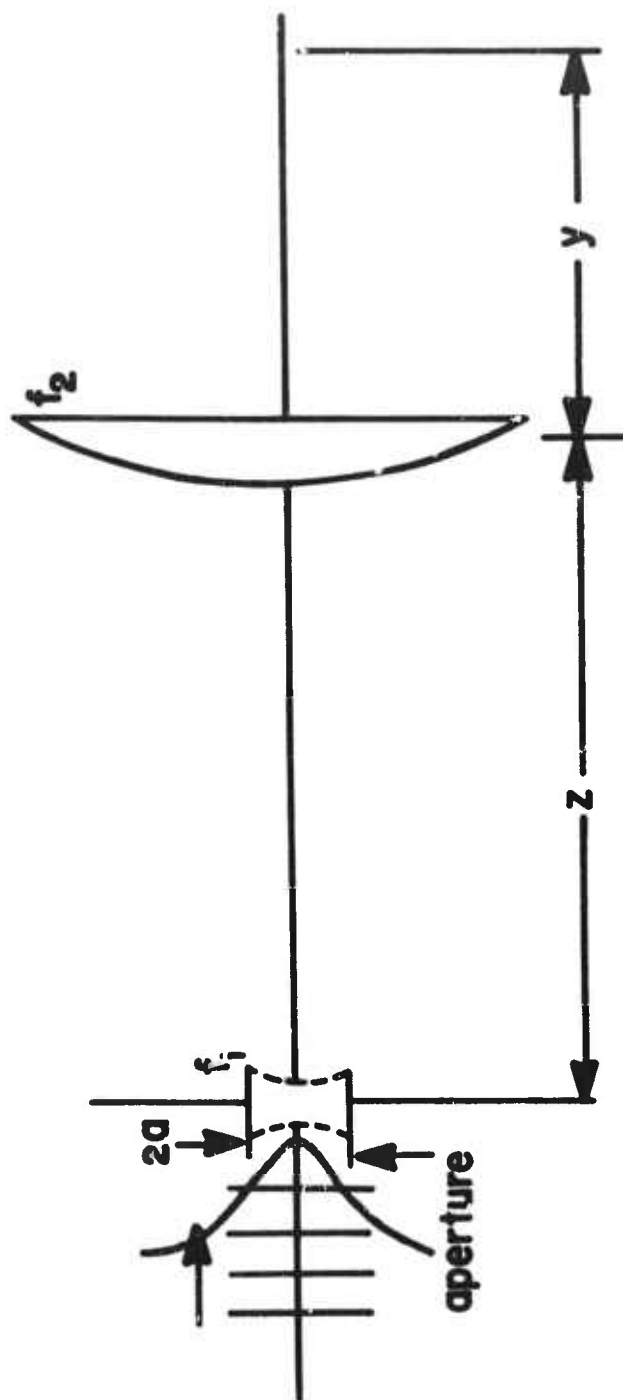
Figure 8.   Focusing of a truncated Gaussian beam, described by the truncation parameter a/w and the initial divergence represented by a lens in the aperture lens f_1.

geometric focal length f_1 and the radius a. A lens of geometric focal length f_2 is placed a distance z from the lens f_1, and the beam is viewed a distance y away from the lens. The axial intensity I at the distance y is determined from Eq. (2).

$$I = 2A^2 \left(\frac{y}{f_2} - 1\right)^{-2} \left[\frac{1}{f_1}\left(z - \frac{yf_2}{y-f_2}\right) - 1\right]^{-2} \frac{\left(\frac{ka^2}{2g}\right)^2 e^{-a^2/w^2}}{\left(\frac{a}{w}\right)^4 + \left(\frac{ka^2}{2g}\right)^2}\left[\cosh(a/w)^2 - \cos\Omega\right]$$

where $k = 2\pi/\lambda$

$$\frac{1}{g} = \frac{1}{f_1} - \frac{i}{z - yf_2/(y - f_2)}$$

(2)

$$\Omega = \frac{ka^2}{2}\left(\frac{1}{z} - \frac{1}{f_1}\right) - ky\left(1 - \frac{y}{h} - \sqrt{\frac{(h-y)^2}{h^2} - \frac{a^2}{z^2}}\right); \quad \frac{1}{h} = \frac{1}{f_2} - \frac{1}{z}.$$

Even though this is a rather complex expression, the axial intensities can be easily plotted by computer and the plots have predicted the experimental results.

In our experiment, a lens of 20.7 cm focal length was located 109.5 cm from the laser. The effective value of f_1 was calculated to be -154.5 cm from the theoretical radial phase distribution [3]. Since the equivalent Gaussian (corresponding to the measured laser divergence) and truncated Gaussian calculations of the axial intensity differ greatly near the focus, the axial intensity was directly measured and compared to the two calculations. The axial intensity of such small spots can be accurately determined by measurements of the energy required to damage Polaroid film. A microscope is required to examine the film. Fresh undeveloped Polaroid film (Type 410) was calibrated to have a damage threshold at 50 mJ/cm^2, which was independent of the laser beam spot-size. Figure 9 shows the measured axial intensity distribution after the lens and its comparison to both the equivalent Gaussian and truncated Gaussian laser beam calculations. The measured intensity value near the focus is about twice that predicted by the equivalent Gaussian calculation. The difference between the measured distribution and the truncated Gaussian calculation is not as large as indicated
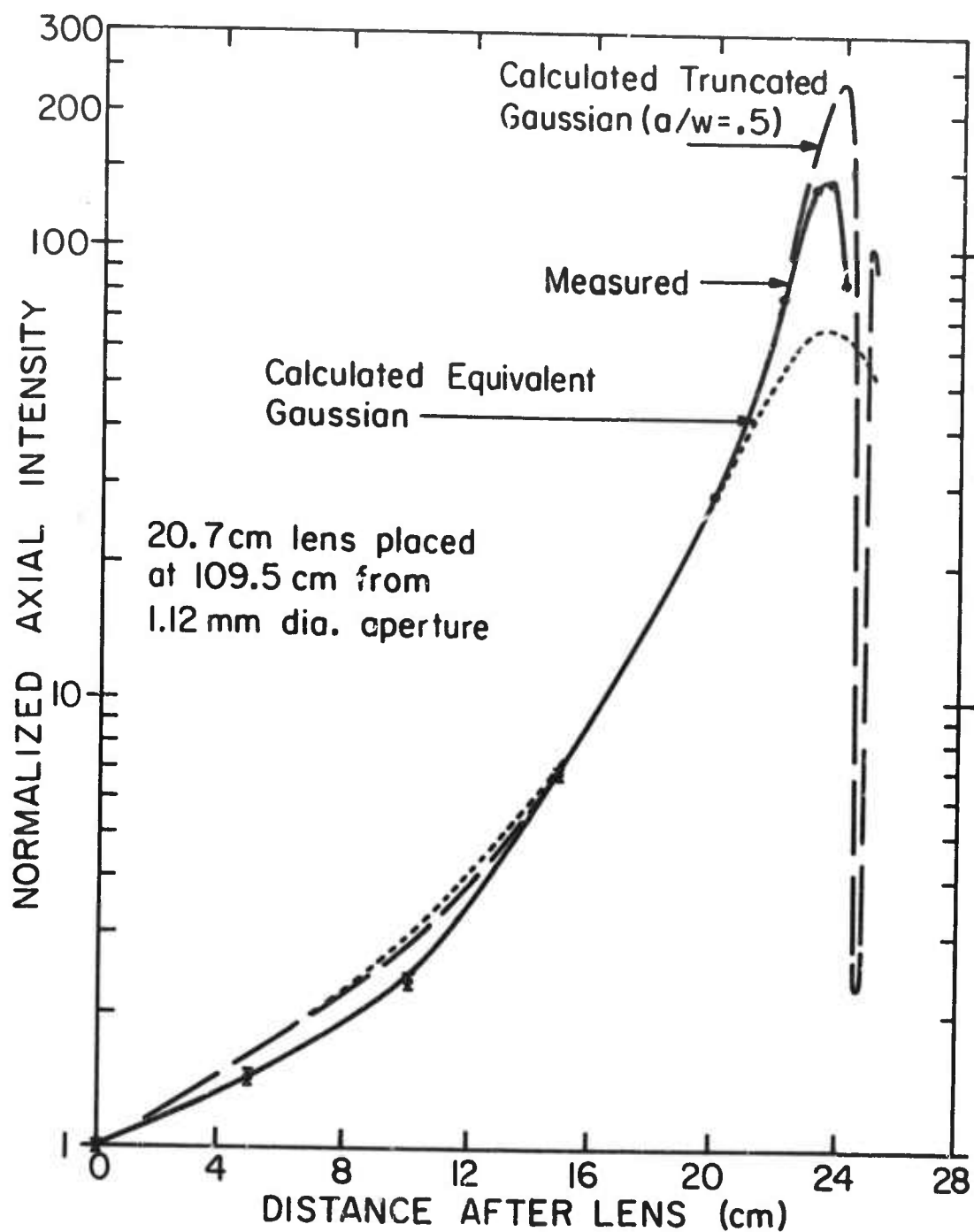
Figure 9. Axial intensities before the focus of a lens
(F = 20.7 cm) comparing the measured inten-
sities to the calculated equivalent and truncated
Gaussian distributions.

because the actual truncation parameter is near 0.6 and not the 0.5 as plotted.

Observation of the intensity profile of a truncated Gaussian beam after the focus reveals axial maxima and minima, unlike the smooth distribution before the focus. This is explained by recognizing that near-field axial extrema are present before the lens, which, when the lens is used in the far-field ($z > 2a^2/\lambda$), are transformed to locations after the focus. Figure 10 illustrated that the intensity distribution is not symmetrical about the focal plane for truncation parameters less than 2. Therefore, it is quite important to place the test samples before the focus in order to know the laser power densities incident to the samples.

In determining the damage thresholds, areas of a sample were irradiated by one shot only. Whether damage occurred or not, a new location was irradiated on each shot. The auxiliary He-Ne laser beam, which travelled collinearly with the pulsed laser beam, indicated the prospective irradiation sites.

The total energy and pulsewidth of each laser pulse were measured, and the presence of a spark at the sample surface was detected photoelectrically.

3. Thin Film Preparation

This study included mono-, bi-, and multi-layered vacuum deposited coatings of the materials MgF_2, SiO_2, ZrO_2, TiO_2, ZnS, ThF_4, and CeO_2 on substrates of glass, fused silica, rock salt, and spinel. These samples were prepared by an in-house facility as well as several commercial sources. Methods used in the preparation were the resistive-heating evaporation, electron-gun evaporation, as well as rf sputtering. The thin-film coatings available for our experiments are listed in Table 2.

Table 2. List of thin film coatings for laser damage study. All wavelengths refer to 6941Å.

Identification number	Supplier	Film Material	Substrate	Remarks
A. Single layer, quarter-wave				
U101, U102, U103, U104	USC	ZnS	cleaved NaCl	
U201, U202, U203, U204	USC	ZnS	BSC2 glass	
O121, O122	OCLI	TiO_2	BSC2 glass	
O125, O126	OCLI	SiO_2	BSC2 glass	
O129, O130	OCLI	ZrO_2	BSC2 glass	
O133, O134	OCLI	MgF_2	BSC2 glass	
V101, V102	Varian	ZnS	cleaved NaCl	
U5a	USC	ZnS	glass	
U101	USC	ZnS	spinel (Union Carbide substrate)	
B. Single layer, half-wave				
O123, O124	OCLI	TiO_2	BSC2 glass	
O127, O128	OCLI	SiO_2	BSC2 glass	
O131, O132	OCLI	ZrO_2	BSC2 glass	
O135, O136	OCLI	MgF_2	BSC2 glass	
C. Single layer, three-quarter wave				
O137, O138	OCLI	TiO_2	BSC2 glass	
D. Bilayer antireflection v-coatings				
H101, H102	Herron	ZrO_2-MgF_2	glass	
H103	Herron	ZrO_2-MgF_2	glass	baked
O141, O142	OCLI	TiO_2-SiO_2	glass	
O143, O144	OCLI	ZrO_2-SiO_2	glass	
O145, O146	OCLI	ZrO_2-MgF_2	glass	
O147, O148	OCLI	TiO_2-MgF_2	glass	
E. Multilayer reflection coatings				
S101	Sper-Phy	TiO_2-SiO_2	glass	special high-threshold
S102	Sper-Phy	TiO_2-SiO_2	glass	std. commercial
S103	Sper-Phy	ZrO_2-SiO_2	fused silica	
H104	Herron	TiO_2-SiO_2	glass	ir trans./visible refl.
H105	Herron	TiO_2-SiO_2	glass	ir trans./ visible refl., baked
H106	Herron	TiO_2-SiO_2	glass	ir trans./visible refl., but 90% trans, .8μ
O101, O102	OCLI	TiO_2-SiO_2	glass	plasma resistant
O103, O104	OCLI	TiO_2-SiO_2	glass	22 layers (λ/4 per layer)
O105, O106	OCLI	ZrO_2-SiO_2	glass	29 layers
O107, O108	OCLI	ZrO_2-MgF_2	glass	25 layers
O109, O110	OCLI	TiO_2-SiO_2	BSC2 glass	12 layers
O111, O112	OCLI	TiO_2-SiO_2	glass	22 layers
SS101, SS102, SS103	Spec. Syst.	Unknown	fused silica	probably ZrO_2-SiO_2
U111	USC	ZnS-ThF_4	BK7 glass	17 layers, resistance heating deposition
O165, O166	OCLI	Enhanced Ag	BSC2 glass	98% reflectance
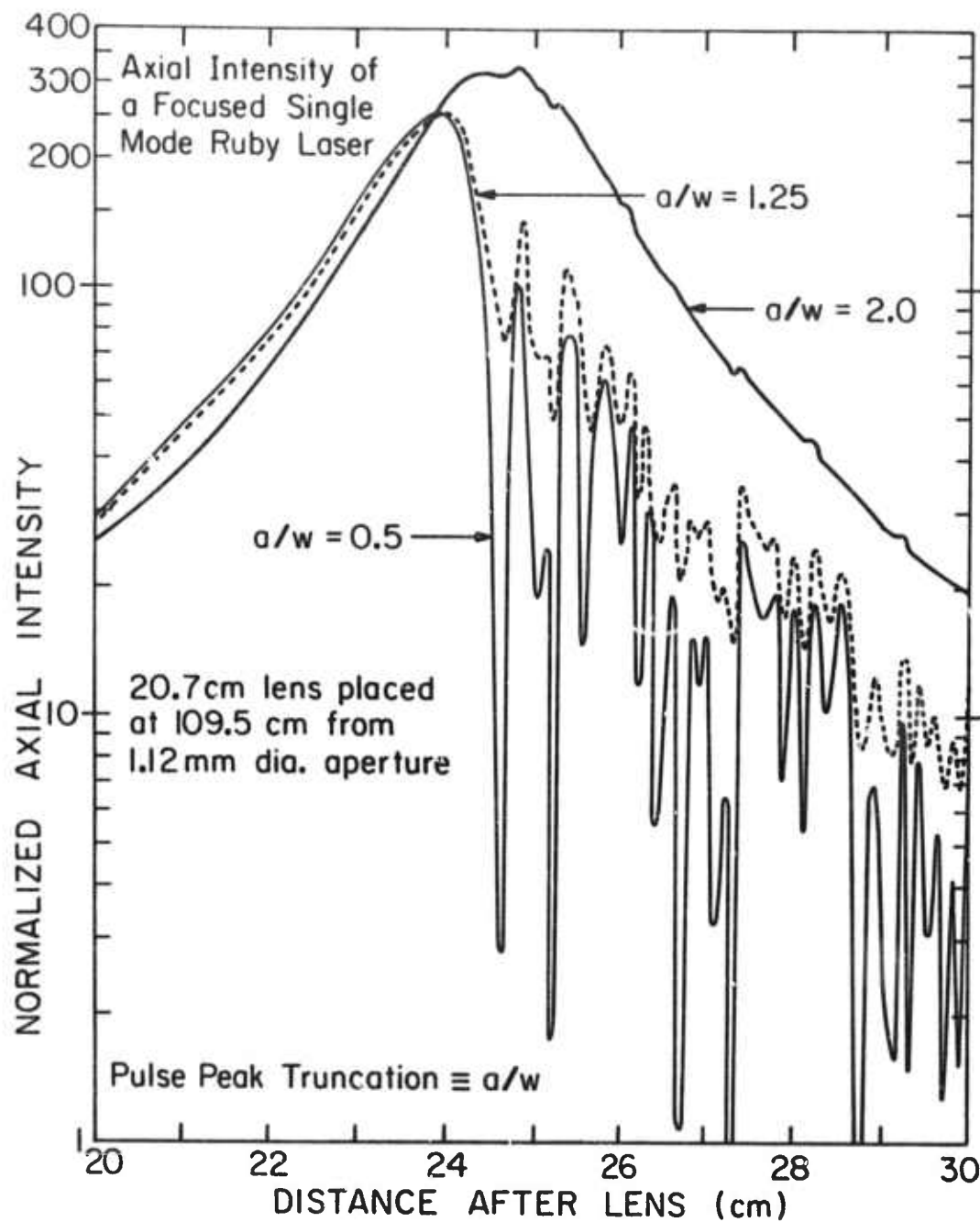
Figure 10.   Axial intensity after the focus of a lens
(F = 20.7 cm) for truncated Gaussian beams
with truncated parameters 0.5, 1.25 and 2.0.

III.   DETECTION METHODS

An important aspect of this program has been the determination of a sensitive and reliable criterion for the onset of damage.   Many investigators of laser-induced surface damage to transparent dielectrics have observed a luminous surface spark whenever physical damage occurred.   For example, see Figure 11. Some have proposed that the spark is responsible for the observed damage.   Although it has become a convenient practice to identify the spark threshold as the damage threshold, other researchers also detected damage without seeing any sparks.   Four different kinds of detection methods were studied in this program: 1) photo-electric detection of the spark, namely, spark detection system, 2) visual observation of laser-induced increases in the weak-signal film scatter, namely, laser-induced scatter (LIS), 3) microscopic observation of film breakup and damage morphology including optical and scanning-electron microscopy, 4) time evolution of laser induced damage, namely, time resolution optical probe technique.   In the following, these methods will be described and then evaluated accordingly.

1.   Spark Detection System

The spark emission was detected with a photomultiplier tube (RCA 6199) at 4340Å using a narrow-band interference filter (FWHM = 40Å).   Detection of only the blue emission decreased the interference from the flash-lamp light.   The photoelectric signal caused by the spark emission was measured with a Tektronix Model 555 oscilloscope and was effectively isolated from the blue emission of the lamp by means of a passive high pass filter.   The electronic circuitry of the detection system is shown in Figure 12.

Examples of oscillograms corresponding to laser-induced sparks are illustrated in Figure 13.   Signals for the incident laser energies causing the sparks are also shown.   The

23.
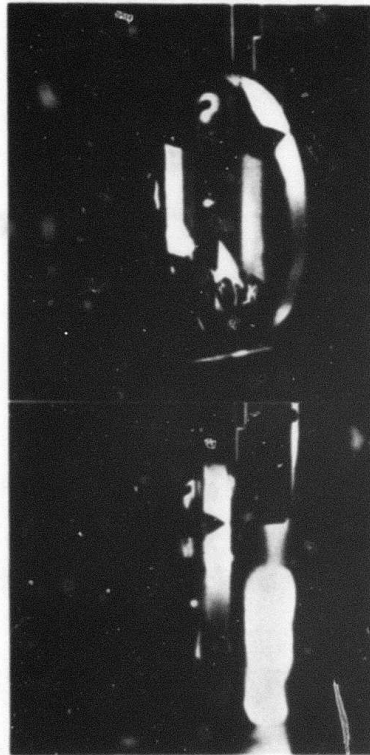
Figure 11. Laser-induced sparks above the damage threshold
of a multilayer reflector. The two smaller images
shown in the front view (a) are a tiny spark (above)
due to energy inter-reflected in the focusing lens
and focused flashlamp illumination (behind; flat
image) reflected to the camera.
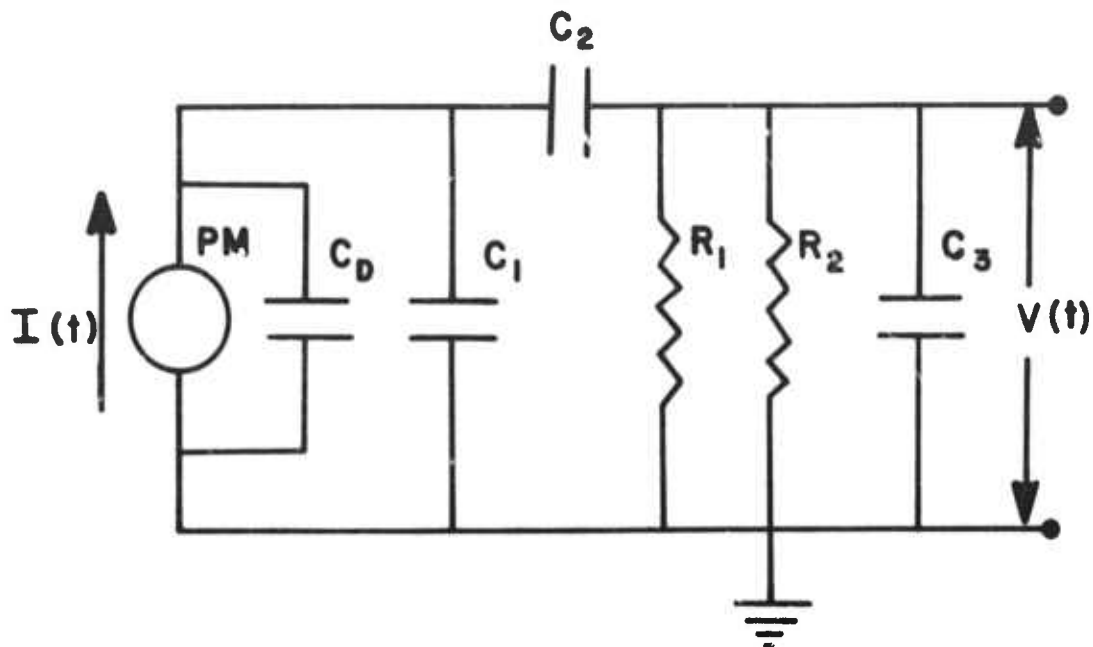
Detector: RCA 6199 Photomultiplier

$C_D = 67$ pfd., Risetime $= 2.5$ nsec.

Connecting Cable: RG 58/U, $C_1 = 150$ pfd.

Low Frequency Filter: $R_1 = 150$ KΩ

$C_2 = 100$ pfd.

Oscilloscope: Type 1A1 Tektronix Plug- In

Type 555 Dual Beam Unit

$R_2 = 1$ MΩ, $C_3 \cong 15$ pfd.

Figure 12.   Electronic circuit for photoelectronic detection
of laser-induced spark emission.

a

b
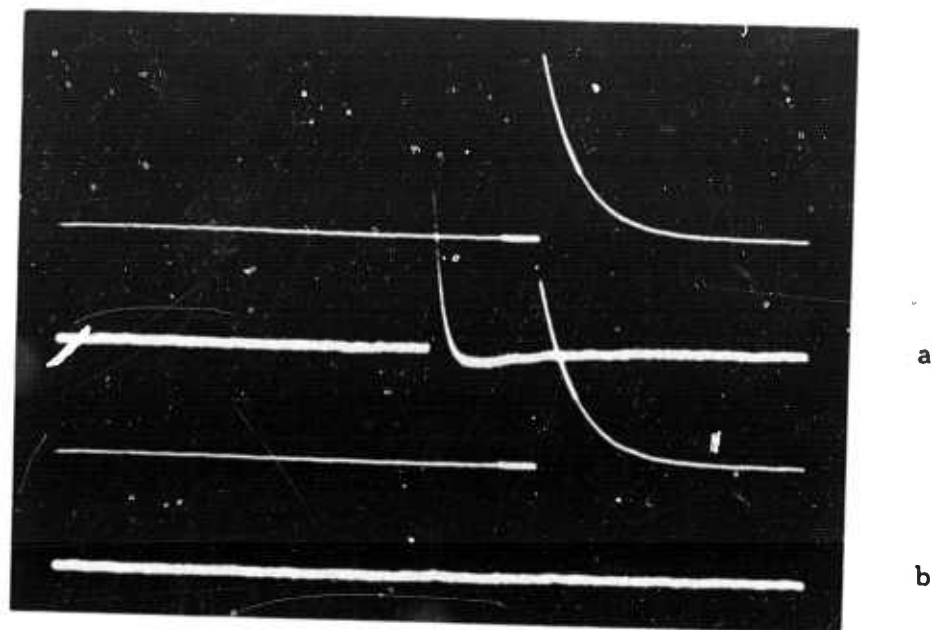
Figure 13.   Measurement of laser-induced spark emission
(a) above and (b) near the spark threshold.
Also measured is the incident laser energy
(upper traces).   Dual-beam oscillograms
with 10 mv/cm vertical scale and time scales
of 200μ sec /cm (energy) and 50 μsec/cm
delayed by 1 msec (spark) are shown.

height of the signal deflection was a measure of the total energy contained in the spark or laser beam. The sensitivity of the detection system is evaluated in detail in Technical Report No. 5 of this program. For a typical damage spot of $10\mu m$-radius area, it is estimated a spark emission per unit area and wavelength of 1.6 watts/$cm^2\mu m$ can be detected. The temperature corresponding to this value is $2300^\circ K$, which is $200^\circ K$ higher than the melting point of TiO_2.

2. Laser-Induced Scatter (LIS)

Evidence of laser-induced disruption of the surface of a coating was manifested by increased scattering of He-Ne laser, travelling collinearly with the pulsed laser beam, illuminated the test area. By visually comparing the level of scattering in a darkened room before and after pulsed irradiation, changes in the coating structure could be detected. These changes were considered as damage. For single-and bi-layer coatings, which had very little incipient scattering, this method provided an especially sensitive measure of the damage threshold.

Another approach of the weak-signal scatter was measured by the intensity of light scattered at about 135° from the direction of the incident beam using a severely attenuated output from the TEM_{00} Q-switched ruby laser instead of a He-Ne gas laser. This beam had a power density of 40 MW/cm^2 and did not produce any changes in the films.

3. Microscopy

The coatings were visually examined after most shots with low-power microscopes (7X or 40X). Since this method was much less sensitive than the first two methods, information obtained was limited to the shape and extent of the damaged areas. More detailed information on the structure of damage near threshold was

provided by photographs of damaged areas under high magnification (100X to 800X) with a Bausch and Lomb Metallograph, and even higher magnification (up to 20,000) with a scanning electron microscope (SEM).

4. Time Resolution Technique

The time evolution of laser-induced damage to thin-films was measured by using an optical probe technique, as well as observing the transmitted pulse. This technique consists of illuminating the surface site to be damaged with a He-Ne laser, and then detecting the reflected beam with a fast electro-optical system. Any change at the surface of the sample is recorded as a change in the intensity of the reflected probe beam, and the temporal behavior of the reflected probe beam is directly related to the temporal change at the sample surface. The damage is caused by a TEM_{00} Q-switched ruby pulse of pulsewidth 10-20 nsec. The temporal shape of the ruby pulse (optically delayed) and the transmitted portion of the pulse after passing through the sample are recorded as input and output pulses respectively. Each damage site is indexed to allow comparison of the SEM photograph and the corresponding time resolved damage trace. Detailed description of the method can be found in Quarterly Technical Reports No. 4 and No. 7 as well as reference [7].

5. Evaluation

a. LIS-Spark Ratio

It was found that for a single or bilayer film the laser-induced increase in the film scattering (LIS) was the most sensitive method for detecting damage. (See Table 3). For multilayer reflecting films, for which the initial He-Ne scatter level was quite high, spark detection was not sensitive. An interesting result was that, for single or bilayer films, an increase in the He-Ne light scatter was observed prior to or at the detectable spark threshold, depending on the film material. If the initial He-Ne scatter levels

Table 4. Comparison of weak-signal scatter and spark threshold for
multilayer reflectors.

Sample	Reflector	Normalized scatter intensities at 6943Å	Peak energy density (spark)
			J/cm^2
O104	TiO_2/SiO_2	1.0	107-127
O102	"	2.3	98-110
[a]U111	ZnS/ThF_4	2.8	25-26
O101	TiO_2/SiO_2	3.5	83-103
O103	"	3.7	121-126
S101	"	6.5	44-56
O105	ZrO_2/SiO_2	9.3	18-20
SS103	CeO_2/SiO_2	14.3	17-19
O106	ZrO_2/SiO_2	16.7	18.5
SS101	CeO_2/SiO_2	24.5	11.5
[a]O108	ZrO_2/MgF_2	24.5	90
[a]O107	"	27.0	81-113
SS102	CeO_2/SiO_2	37.5	14.5-17
S103	ZrO_2/SiO_2	41.5	7.5

[a]Notable exceptions to the correlation.

c. Damage Morphology

The visual examination of irradiated samples using low-power microscopes (7x and 40x) was not as sensitive as the other methods. However, certain structures in the damage morphology can be observed by a high-power optical microscope (100x to 1000x) or electron microscope (up to 100Kx). In general, the damaged areas below spark threshold were typically circular, nearly following the intensity profile of the incident beam. Figure 14 to 19 illustrates that damage with a spark shows a very round hole of rather large size, while Figure 20 and 21 show that damage occurs without always producing a spark.

d. Optical Probe Technique

Results presented here are representative of entrance surface damage to $\lambda/4$ ZnS films on BSC2 glass. Damage was time resolved with a resolution of 2 nsec. The damage evolution falls into two classes: a fast damage initiation process starting near the peak of the ruby pulse and having a rise time of ~4 nsec, and a slow process initiating at the trailing edge or after the ruby pulse and having a rise time 10-20 nsec. When the probe intensity recovers under conditions described in above, the recovery time is 25-50 nsec. Thin film damage areas on the order of $4\mu m$ in diameter have been observed without spark emission, and without distortion occurring in the transmitted ruby pulse. A typical result is displayed in Figure 22. The probe response indicates a fast damage initiation process starting near the peak of the ruby pulse resulting in a fast decrease of the probe intensity to a minimum value typically in less than 4 nsec.
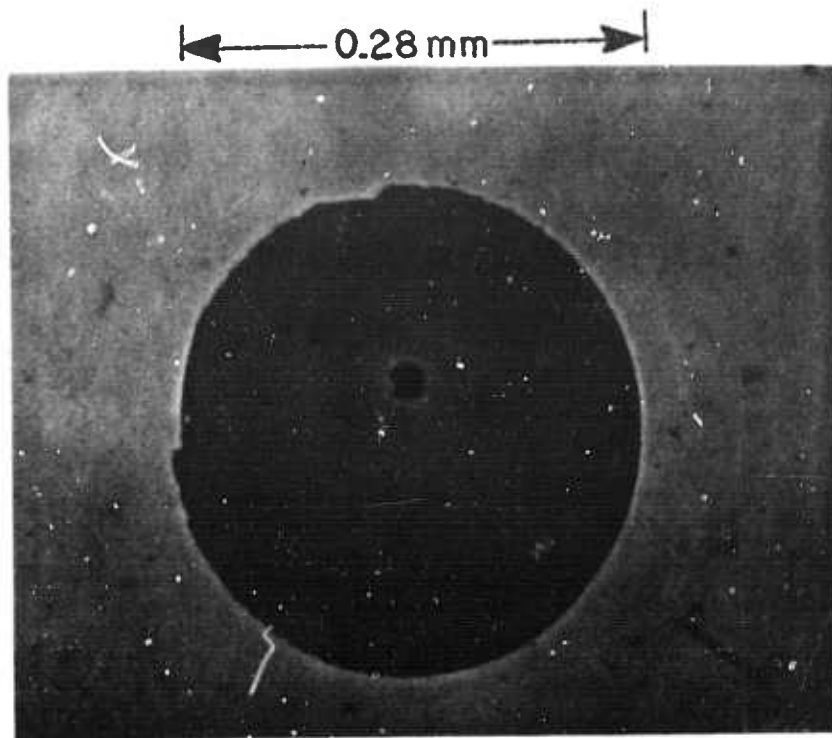
Figure 14.   Laser-induced damage above the spark threshold
for a 22 layer TiO_2/SiO_2 reflector of configuration
$G(HL)^{10}HL^2A$. (by Bausch & Lomb Metallograph)
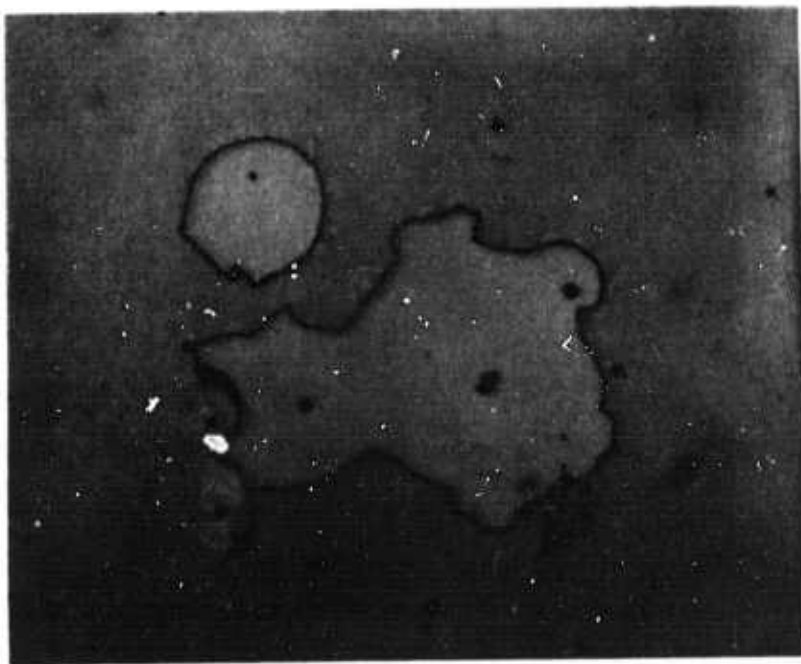
Figure 15.   Laser-induced damage far above the spark threshold
for the same reflector as in Fig. 14.
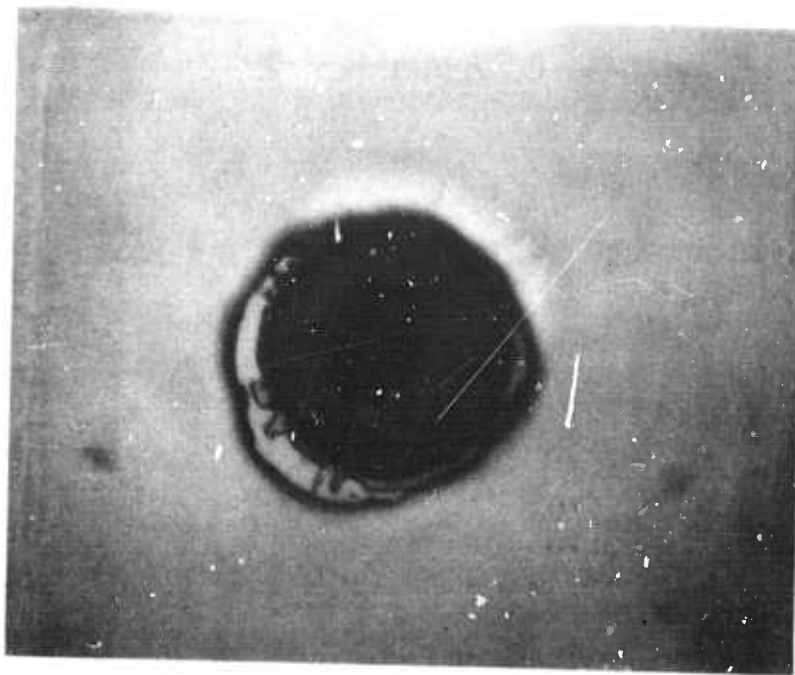
Figure 16.   Severe laser-induced damage on the same reflector
shown in Fig. 14.   The glass substrate is seen on
the site. (magnification: 1100x)

Figure 17.   Laser-induced damage far above the spark threshold
on a TiO_2/SiO_2 multilayer reflector (Sample S101).
Random penetrations to deeper layers is apparent.
(magnification: 120x)

33.
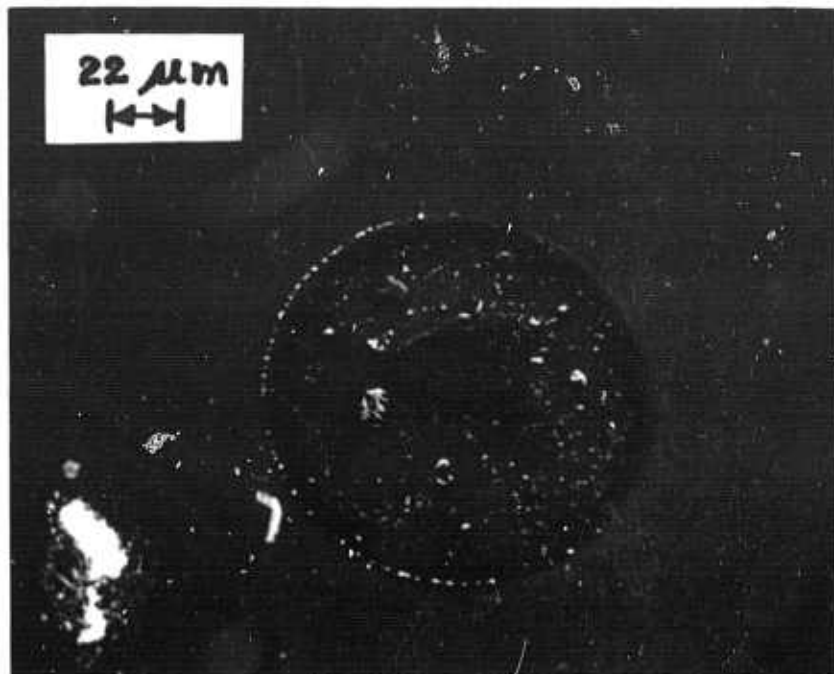
Figure 18.   Scanning Electron Microscope (SEM) photograph of a
damage site on a single quarter-wave thick film of
TiO_2 (Sample O121) where a spark was detected.

Figure 19.   SEM photograph of a damage site on MgF_2, $\lambda/4$ film
(Sample O133).   The site dimension is 100 microns
from left to right (80° sideview of the site).
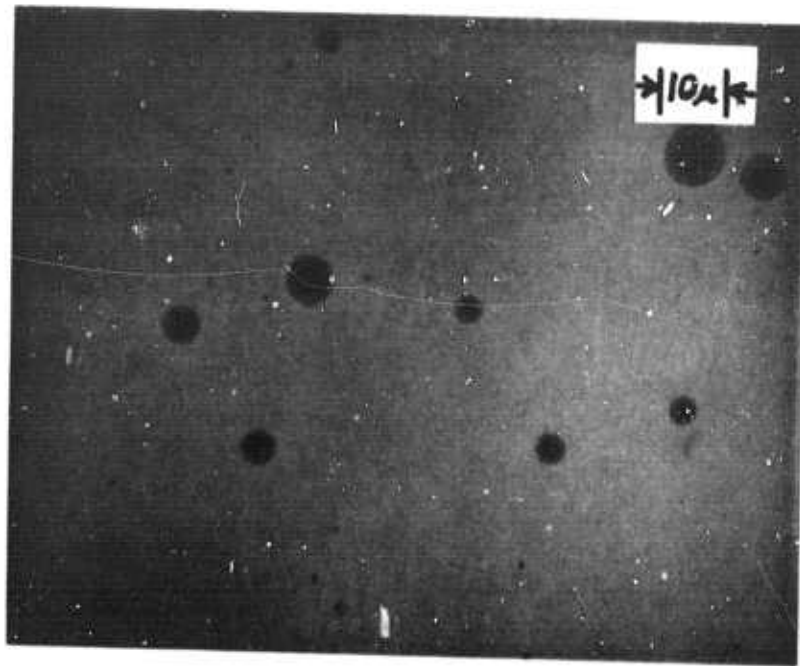
Figure 20.   Laser-induced damage occurring before a detectable
spark in a single quarter-wave film of TiO_2.
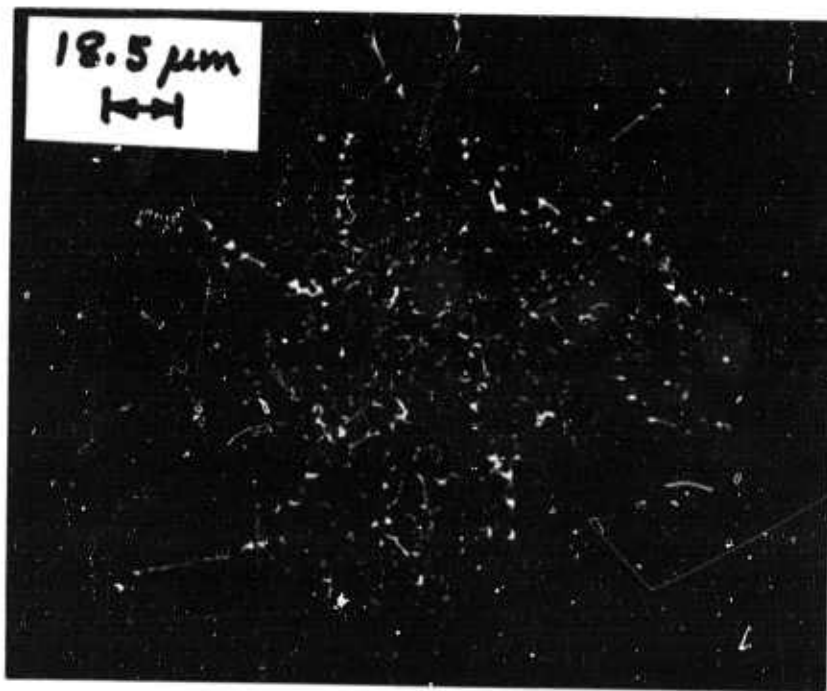
Figure 21.   SEM photograph of a damage site on a single quarter-
wave film of ZnS (U5a) using LIS diagnosis.
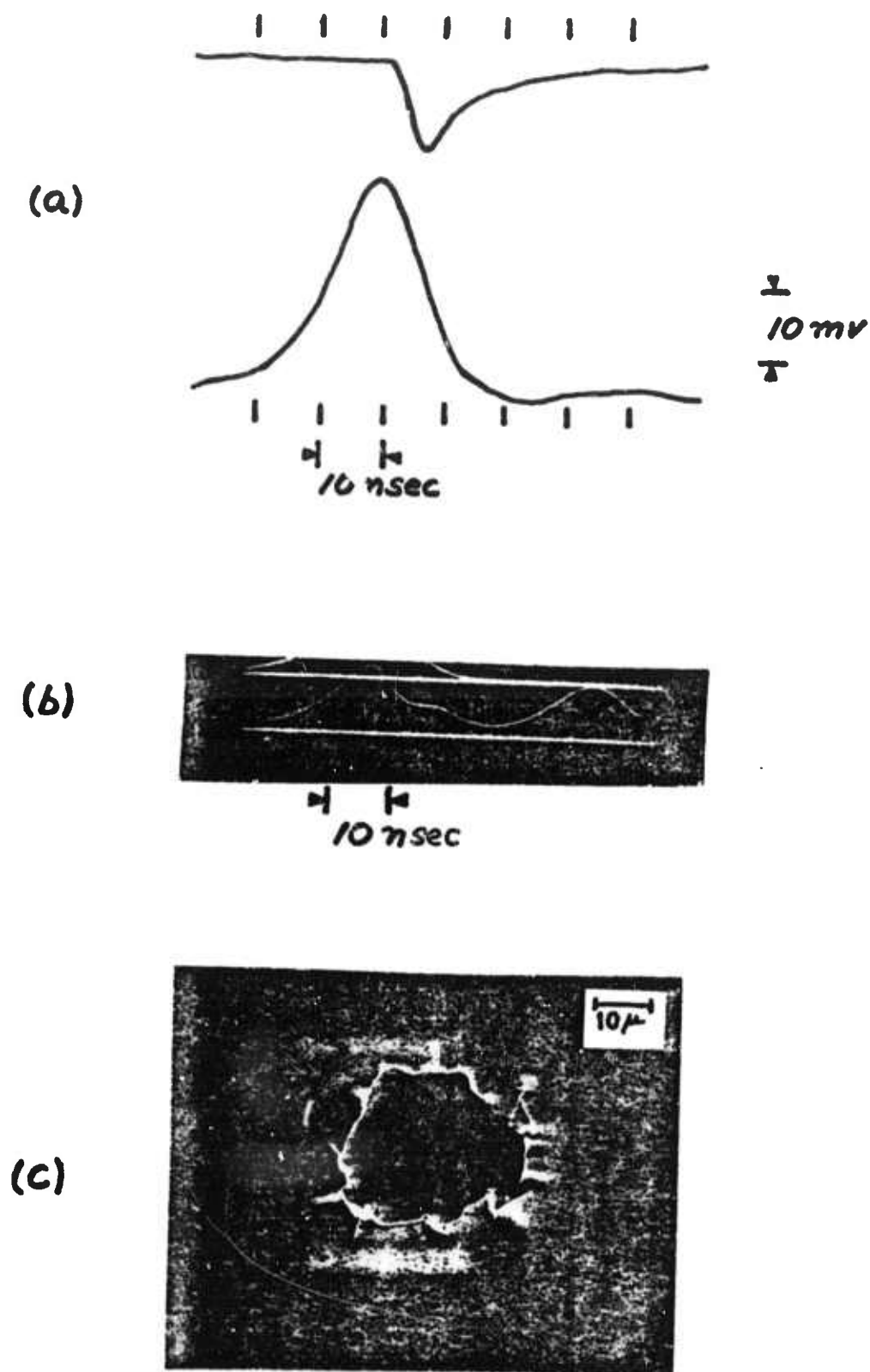
Figure 22. Entrance surface damage to λ/4 ZnS. (a) Probe trace (upper trace) and the damaging ruby pulse (lower trace). The maximum decrease in the probe intensity is 35% of peak intensity (peak intensity is 38 mV). (b) The output damaging pulse is shown followed by the input delayed reference pulse. (c) SEM photograph taken at 10° tilt.

IV. ELECTRIC FIELDS IN THIN FILM COATINGS

1. Introduction

In the analysis of laser-induced damage processes, the role of absorption cannot be neglected. A more detailed discussion of absorption will be presented in Section VII. In this section, we will discuss the role of electric fields which is indirectly related to the absorption in the laser-induced damage.

The power P absorbed per unit volume from an electromagnetic wave of intensity I traveling in a medium having a complex refractive index N is $P = -dI/dz = \beta I$. β is the absorption coefficient which is related to the imaginary part of $N = n - ik$ by the relation $\beta = 4\pi k/\lambda$. For a plane wave $I = \overline{E}^2/\eta$ where $\overline{E}^2$ is the mean square of the electric field averaged over several cycles $(\frac{1}{2}|E|^2)$ and $\eta = (\mu/\epsilon)^{1/2}$ is the wave impedance. In terms of the incident intensity I_o ($= |E_o^+|^2/2\eta_o$), the power absorbed (watts/cm^3) at a distance z in a weakly absorbing medium is

$$P(z) = \beta n \left|\frac{E(z)}{E_o^+}\right|^2 I_o = \frac{4\pi n k}{\lambda} \left|\frac{E(z)}{E_o^+}\right|^2 I_o \quad (3)$$

Similar expression can be obtained for the energy absorbed per unit volume (joules/cm^3) from a light pulse with incident energy density. Since the energy absorbed per unit volume is proportional to the square of the electric field, the standing-wave patterns due to the reflections at the film interfaces must be taken into account.

2. Calculation of Electric Fields in Thin Film Coatings

The electric field intensities were calculated assuming plane waves and planar boundaries. In addition, all films and substrates were assumed to have negligible absorption. The matrix

37.

method [8] involving Fresnel coefficients was used for the calculations. In matrix form, the fields at the boundary of the (m-1)th and mth media are given by

$$
\begin{pmatrix} E_{m-1}^+ \\ E_{m-1}^- \end{pmatrix} = \frac{1}{t_m} \begin{pmatrix} e^{i\delta_{m-1}} & r_m e^{i\delta_{m-1}} \\ r_m e^{-i\delta_{m-1}} & e^{-i\delta_{m-1}} \end{pmatrix} \begin{pmatrix} E_m^+ \\ E_m^- \end{pmatrix}
\tag{4}
$$

where the superscripts + and - designate waves traveling in the forward and backward z directions. r_m and t_m are the Fresnel coefficients and δ_m is the optical phase, given by $\delta_m = 2\pi n_m d_m / \lambda_o$ where d_m is the layer thickness. This matrix equation is a recursion relation between the electric fields in successive layers and allows convenient computation of E(z) in terms of the incident field E_o^+.

The indices of refraction for the film and substrate materials at the ruby laser wavelength that were used in our calculations are listed in Table 5.

Solutions were obtained for normal incidence on single-layer films, bilayer V-type antireflection coatings and multilayer reflection coatings. Solutions for non-normal incidence on single-layer coatings for polarizations perpendicular (S) and parallel (P) to the plane of incidence were also obtained. A brief summary on general expressions of $|E_i / E_o^+|^2$ for different cases as well as the corresponding computer programs can be found in Appendix A. Some of the results from the calculations will be used to analyze our experimental data in the subsequent sections.

Table 5. Refractive indices of film and substrate materials at
6943Å .

Material	Index of refraction	Reference
MgF_2	1.38	[9]
SiO_2	1.456	[9]
ThF_4	1.52	[10]
ZrO_2	1.975	[9]
CeO_2	2.2	[11]
TiO_2	2.28	[9]
ZnS	2.32	[10]
Fused silica	1.456	[12]
BSC2 glass	1.513	[13]
NaCl	1.54	[14]
Spinel	1.73	[15]
YAG	1.83	[15]

a. Single-layer Films

In the case of normal incidence, Figure 23 shows the
distributions of the electric-field intensity for quarter-wave films of
MgF_2, SiO_2, ZrO_2 and TiO_2 on a glass substrate. Note that the
intensity scale is broken at 1.6, and the peak of some distributions
in air has been displaced downward and plotted on the scale in
parenthesis. Figure 24 shows the intensity distributions for half-
wave films of the same materials. Since SiO_2 films have an index
of refraction near to the index of the glass substrate, there is not
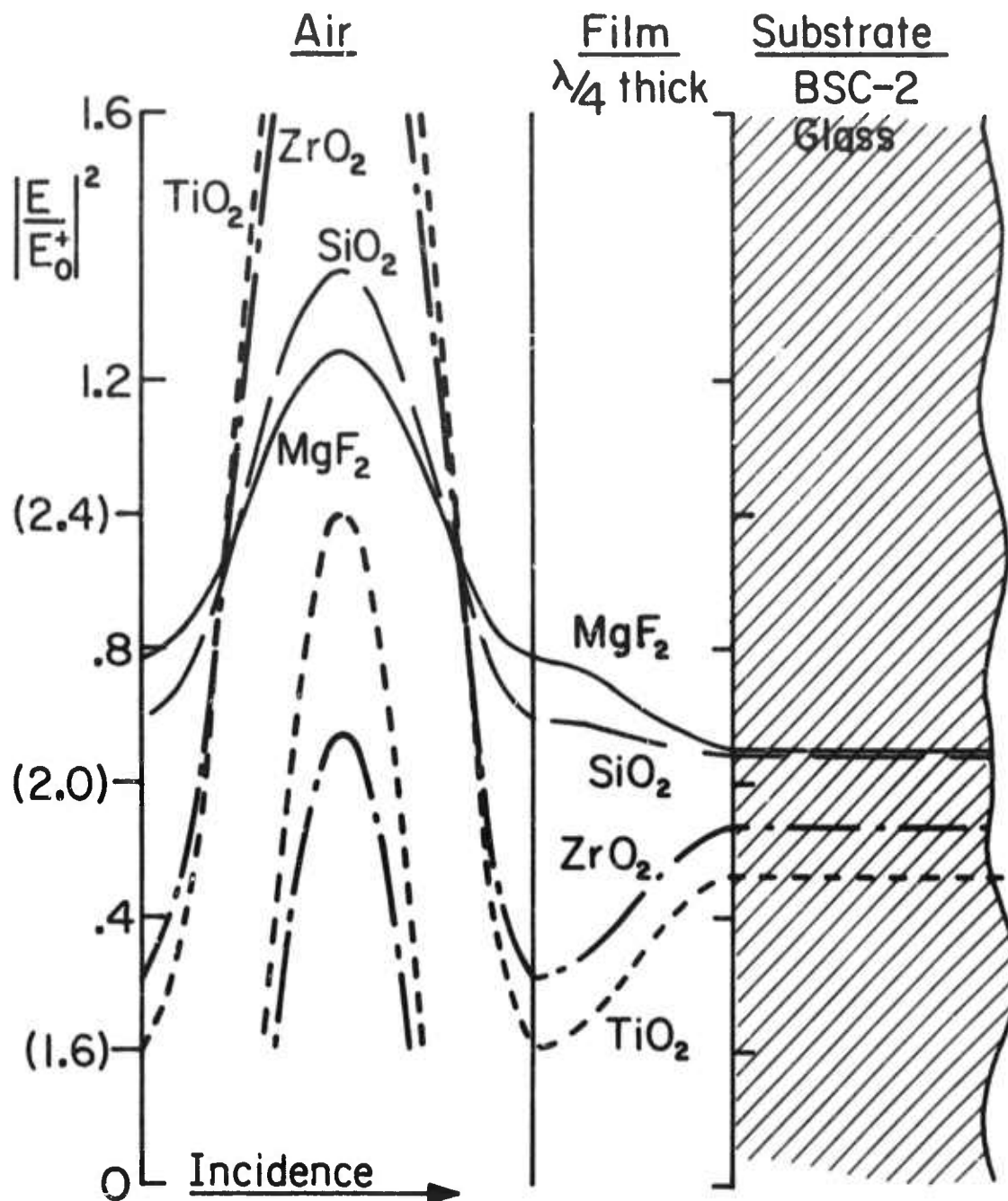
Figure 23.   Relative electric-field intensity distributions for
quarter-wave films on BSC-2 glass substrates.
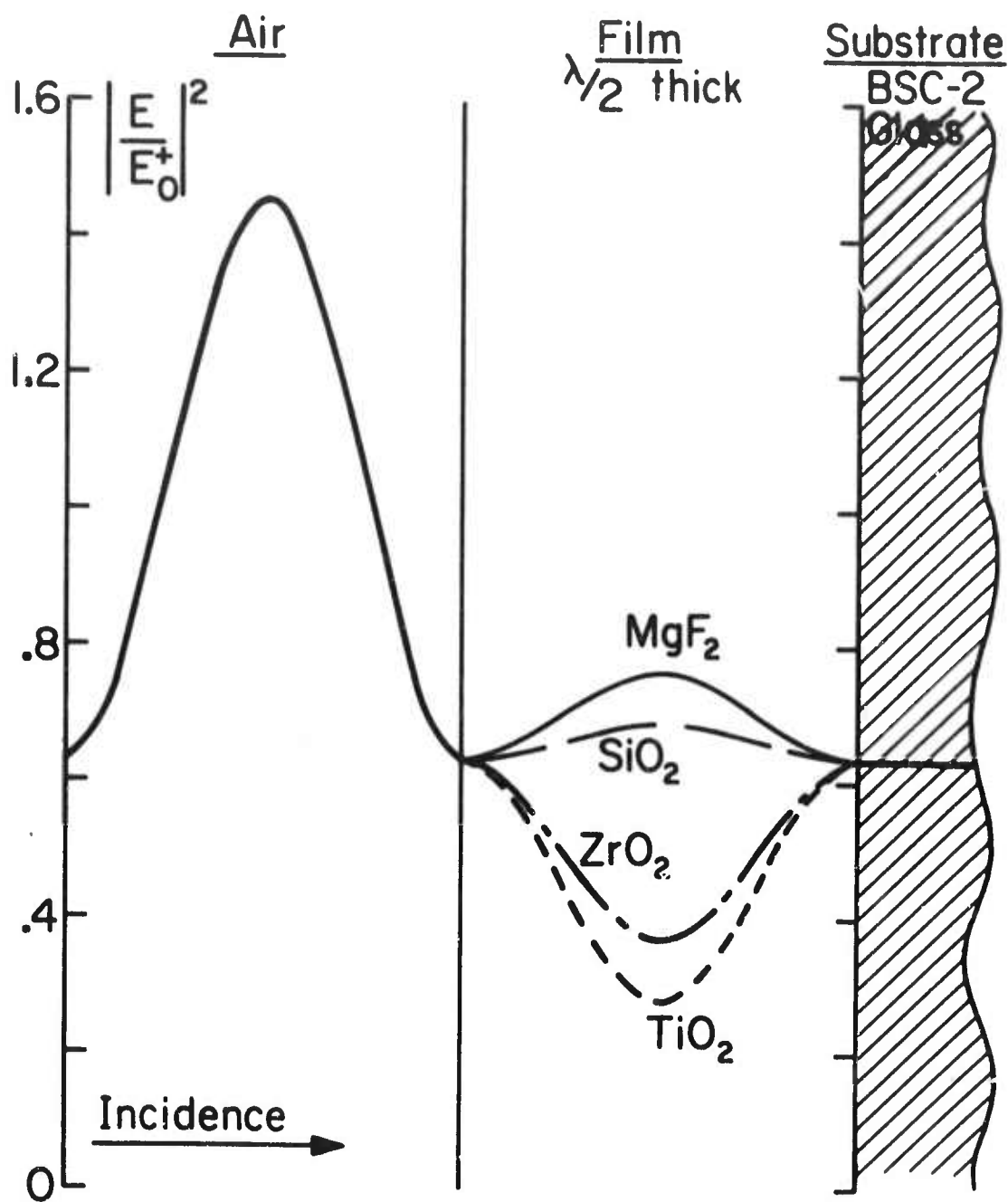
Figure 24.   Relative electric-field intensity distributions
            for half-wave films on BSC-2 glass substrates.

much difference between the intensity distributions for the quarter and half-wave films. The main differences for the other film materials occur at the air-film interface.

In the case of non-normal incidence, Figures 25 and 26 show the relative power-density distributions for both S and P polarizations for quarter and half-wave thick films of MgF_2. The thresholds for P polarization should be significantly lower than those for S polarization.

b. Bilayer Antireflection Coatings (V-type)

The electric fields in bilayer antireflection coatings of a V-design were calculated for normal incidence in two steps. First, the thicknesses of the two layers were calculated, and then the fields were computed. The thicknesses were calculated directly using the relations of Hass [16] and Catalan [17]. These relations yield the thicknesses required to obtain 0% reflectance at a given wavelength for normal incidence. The actual coatings were designed for pairs of films with high and low refractive indices on BSC-2 glass substrates. The higher-index layer was adjacent to the substrate and was less than $\lambda/4$ thick. The calculated optical phases and thicknesses and the physical thicknesses are listed in Table 6. The substrate was BSC-2 glass. The thicknesses of the high-index layers ranged from 1/5 to 1/2 of a quarter-wave, and the thicknesses of the low index layers were all about 1.3 quarter-waves.

The electric-field distributions shown in Figure 27 are about the same for each V-coat. The only differences occur in the power density distributions which is obtained by multiplying the relative electric-field intensity by the index of refraction.
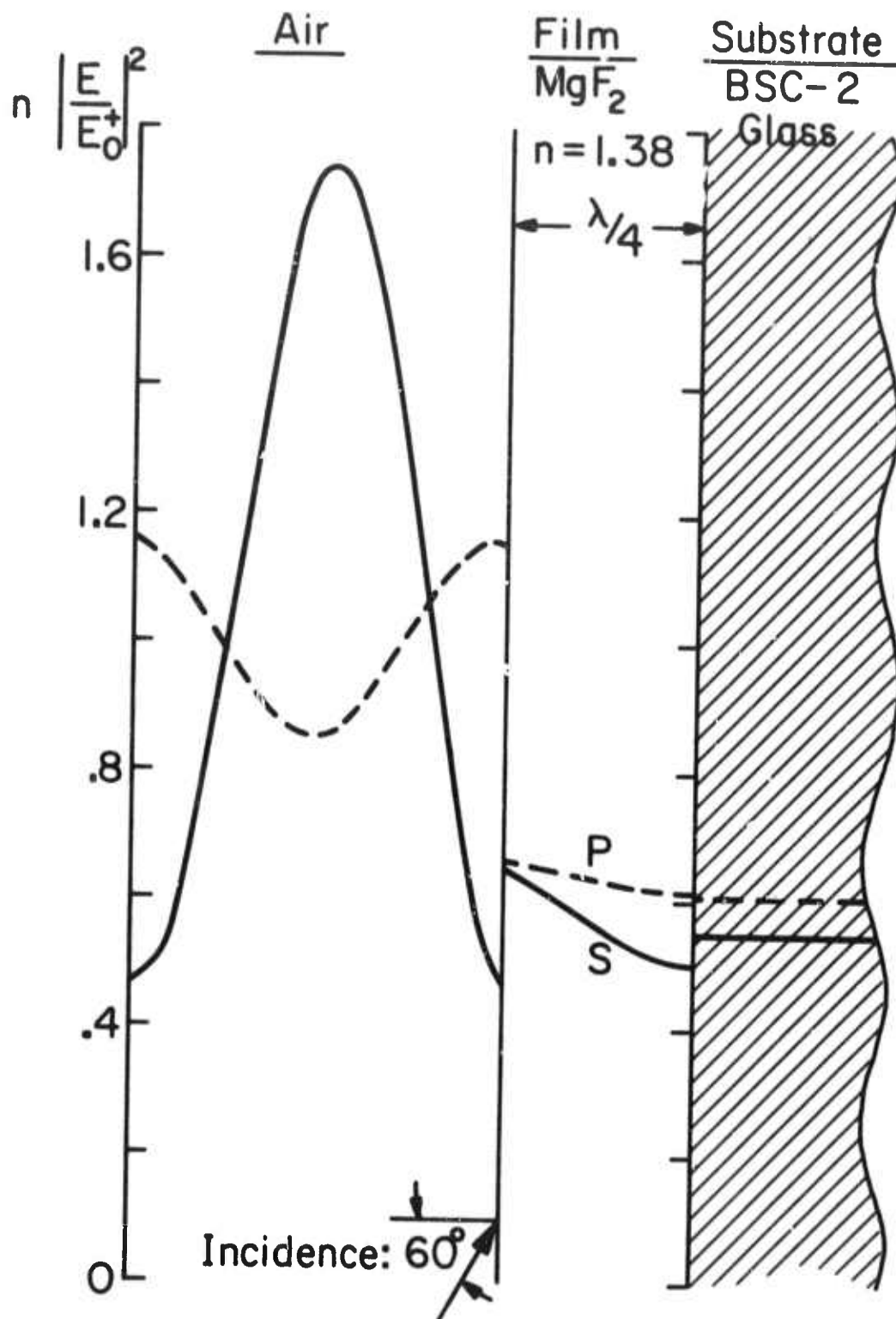
Figure 25. Relative power-density distributions for a quarter-
wave film of MgF$_2$ on a BSC-2 glass substrate for
60° incidence as a function of incident polarization.
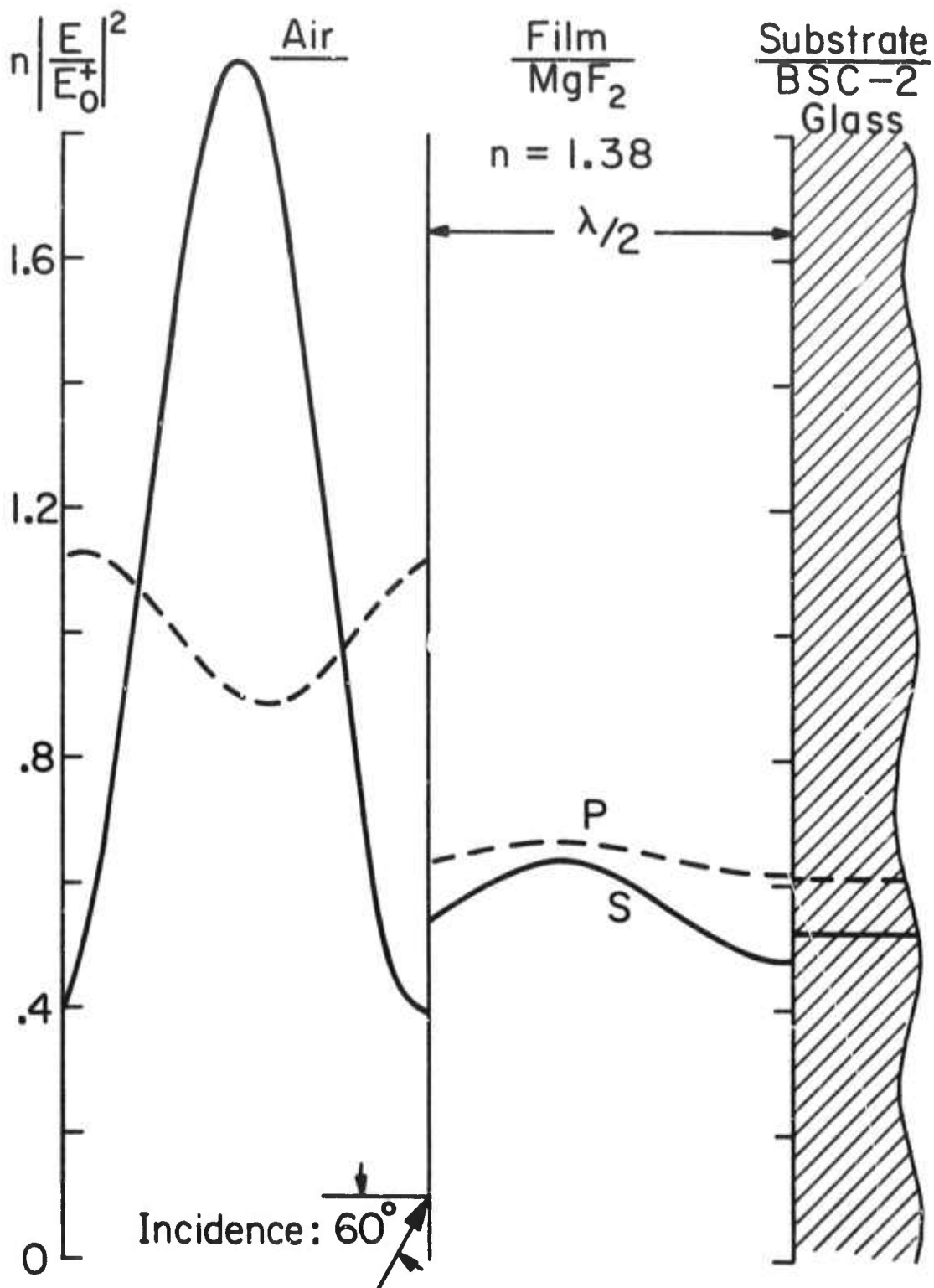
Figure 26. Relative power-density distributions for a half-wave film of MgF_2 on a BSC-2 glass substrate for $60°$ incidence as a function of incident polarization.
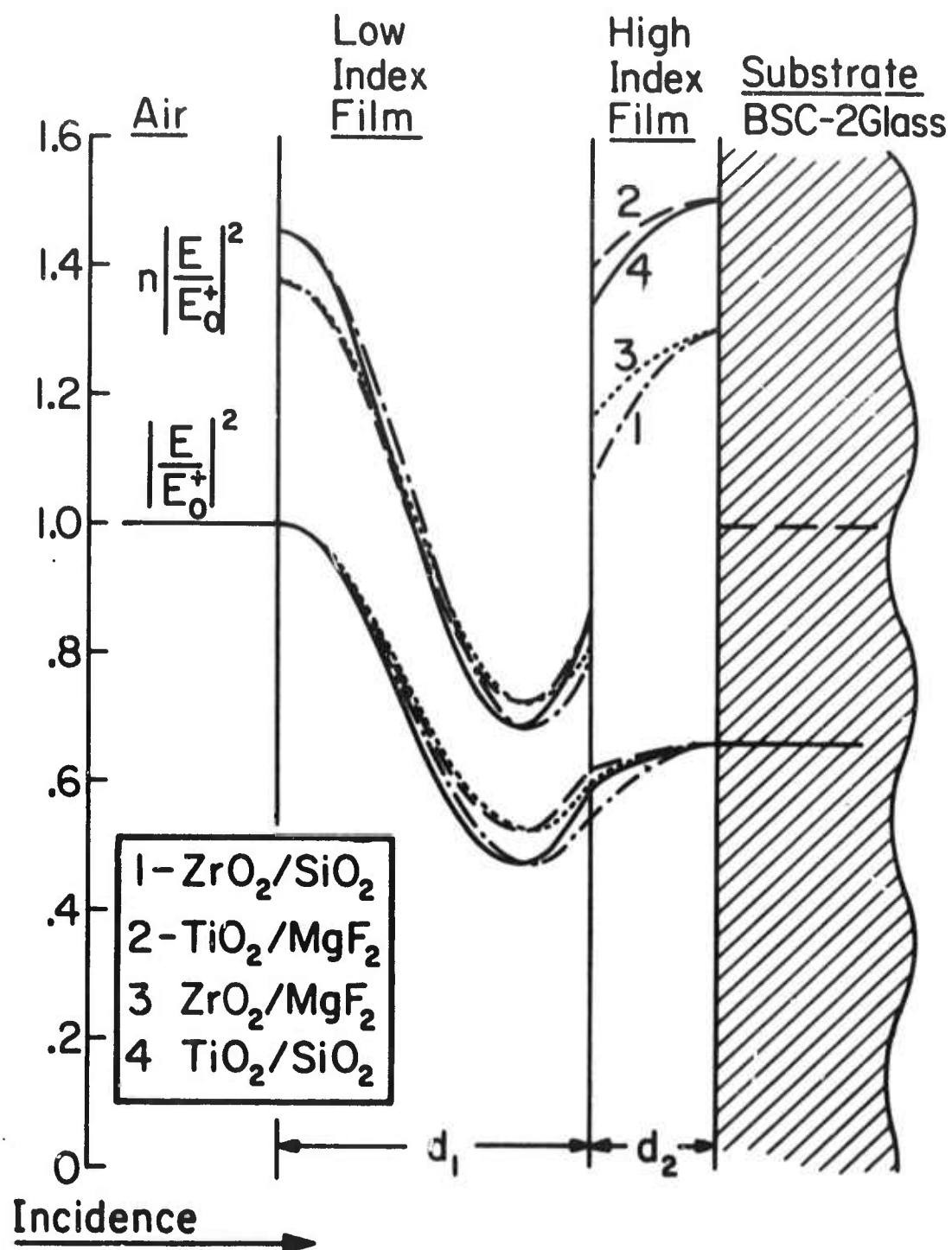
Figure 27. Relative electric-field intensity and power-density
distributions for bilayer antireflection coatings on
BSC-2 glass substrates.

Table 6. Thicknesses of bilayer antireflection coatings.

Sample No.	O143	O145	O147	O142
Materials	ZrO_2/SiO_2	ZrO_2/MgF_2	TiO_2/MgF_2	TiO_2/SiO_2
δ_1 (degrees)	111.9	112.5	116.65	118.8
δ_2 (degrees)	40.6	29.55	19.2	25.2
$n_1 d_1 (\lambda/4)$	1.244	1.250	1.296	1.320
$n_2 d_2 (\lambda/4)$	0.451	0.328	0.214	0.280
d_1 (nm)	148.2	157.2	163.0	157.3
d_2 (nm)	39.65	28.86	16.27	21.29

c. Multilayer reflectors

The electric field distributions for normal incidence in two multilayer reflection coatings are shown in Figures 28 and 29, and the fields at the film interfaces of these and other reflectors are listed in Table 7. Note that the most damage-resistant reflectors of the TiO_2/SiO_2 configuration have lower electric fields at the H-L interfaces than the other designs. Furthermore, for all reflectors the fields decrease rapidly from the top layer inward, and at the substrate they are negligible. This explains why only the top layers are damaged at threshold.

As illustrated in Figures 28 and 29 the electric field intensities peak at the H-L interfaces. Therefore, for laser irradiation above threshold, damage involves removal of layers in pairs since the high-index films are less damage resistant than the low-index films. For example, at the first peak in the electric-field-squared inside the TiO_2/SiO_2 reflector, the energy density in the high index layer was 65% higher than in the low-index layer.

Figure 28. Relative electric-field intensity distributions for a 29-layer ZrO_2/SiO_2 reflector with $G(HL)^{14}HA$ configuration.

Figure 29. Relative electric-field intensity distributions for a 22-layer TiO_2/SiO_2 reflector with $G(HL)^{10}HL^2A$ configuration.

Table 7. Normalized electric field intensities in multilayer reflectors

Sample	Film Materials	Design reflectance	Number of layers	Film order	$\|E/E_0'\|$ in top low index layer	$\|E/E_0'\|^2$ at first H-L interface	$\|E/E_0'\|^2$ at second H-L interface
		%					
O102,103	TiO_2/SiO_2	99.9+	20	$G(HL)^9 HL^2 A$	1.887	0.724	0.278
O105,106	ZrO_2/SiO_2	99.9+	29	$G(HL)^{14} HA$	--	1.025	0.557
O107,108	ZrO_2/MgF_2	99.9+	25	$G(HL)^{12} HA$	--	1.025	0.501
SS101,102,103	CeO_2/SiO_2	95.3	13	$G(HL)^6 HA$	--	1.027	0.573
O103,104	TiO_2/SiO_2	99.9	22	$G(HL)^{10} HL^2 A$	1.887	0.769	0.314
O109,110	"	98.7+	12	$G(HL)^5 HL^2 A$	1.875	0.764	0.312
None		98.7	11	$G(HL)^5 HA$	--	0.764	0.312
None	"	97.3	12	$G(HL)^6 A$	3.945	1.609	0.656
Incidence from substrate side:							
O103,104	TiO_2/SiO_2	As above		--	--	1.116	0.455
O105,106	ZrO_2/SiO_2	As above		--	--	1.487	0.808
O107,108	ZrO_2/MgF_2	As above		--	--	1.485	0.725

3. Damage thresholds for entrance and exit face coatings.

The damage thresholds of entrance and exit-face coatings were measured.   These tests were conducted to find out if there is a direct relationship between the thresholds and the electric field standing-wave distributions in the films.   Listed in Table 8 are the peak energy density thresholds as measured by LIS for the single-layer films and by spark detection for the multi-layer reflectors. In every case, except for the ZrO_2/MgF_2 reflector (sample O108), the entrance-face thresholds were equal to or greater than the exit-face thresholds.

Table 8. Damage thresholds for entrance and exit face coatings

Sample	Coating description	Spot-size	Peak energy density[a]		Ratio (entr./exit)
			entrance	exit	
Single layers		mm	J/cm^2	J/cm^2	
O125	$SiO_2, \lambda/4$	0.055	117	110-~114	1.0
O133	$MgF_2, \lambda/4$	0.055	111-131	>124	1.0
O135	$MgF_2, \lambda/2$	0.07	65-102	44	1.9
O121	$TiO_2, \lambda/4$	0.072(entr.) 0.09 (exit)	36-42	20-21	1.9
O131	$ZrO_2, \lambda/2$	0.072(entr.) 0.063(exit)	12-13	9.5-10	1.3
O132	$ZrO_2, \lambda/2$	0.15	8.5-9	8	1.1
Multilayer reflectors					
O103	TiO_2/SiO_2	0.056(entr.) 0.07 (exit)	121-126	95-116	1.2
O104	TiO_2/SiO_2	0.056	117-127	98-108	1.2
O106	ZrO_2/SiO_2	0.13	18.5	14.5	1.3
O108	ZrO_2/MgF_2	0.062(entr.) 0.055(exit)	90	128-131	0.7

[a]Single layer thresholds were determined by laser-induced scattering (LIS). Reflector thresholds were determined by spark formation.

For these tests, each coating was alternately faced toward and away from the incident laser beam.   This result is similar to that generally observed for glass and crystal surfaces [18], but there has been considerable discussion about which surface, front or back, at which a laser-induced optical discharge first occurs. Fersman and Khazov [19] and Dupont et al.[20] in measuring surface damage of glass, observed a spark first at the front surface, although damage effects at the rear surface were more severe.   In further investigations Giuliano [21] detected microscopic damage at the exit surface of sapphire prior to the development of a visible spark. This latter result is in agreement with the present observations for thin film coatings in which damage detectable by laser-induced scattering (LIS) occurred before or at the spark threshold.   Now since

the single-layer thresholds were determined by LIS, any possible confusion in damage detection by sparks is avoided. However, there might be a difficulty in the comparison of multilayer thresholds since their thresholds were determined by spark formation.

The electric-field distributions for exit-face single-layer films of quarter and half-wave thicknesses are shown in Figures 30 and 31. These distributions can be compared to those for entrance-face coatings presented in Figures 23 and 24. The obvious difference is that maxima invariably occur at the air-film interface for each exit-surface coating. When the quarter-wave coating is moved from the entrance to the exit face, the intensity increases at the air-film interface and decreases at the film-glass interface with the total intensity within the film slightly increasing. For TiO_2, the intensity increases by 3.55 at the air-film interface and decreases by 0.30 at the film-glass interface. The measured ratio of entrance to exit-face damage thresholds was 1.9 for TiO_2; this value corresponds well to the calculated ratio of 1.56 for the peak intensities (at the film-glass interface in the entrance orientation, and at the air-glass interface in the exit orientation). For MgF_2 and SiO_2, the measured ratio of entrance-to-exit thresholds was unity, corresponding to the calculated ratio of the total intensities within the film (1.09 and 1.04, resp.).

When the half-wave films are considered, there is a simplification in that the film material does not affect the entrance-to-exit intensity ratios. When moved from entrance-to-exit face, the intensity at the air-film interface increases by 1.58 regardless of film material. The intensity at the film-glass interface is the same as the air-film interface, while the intensity extremum within the film decreases by 0.69. For MgF_2 and ZrO_2 half-wave films, the measured ratios of entrance-to-exit thresholds were 1.9 and 1.3. The average of these measured ratios is 1.6, quite close to the value for the air-film interface.
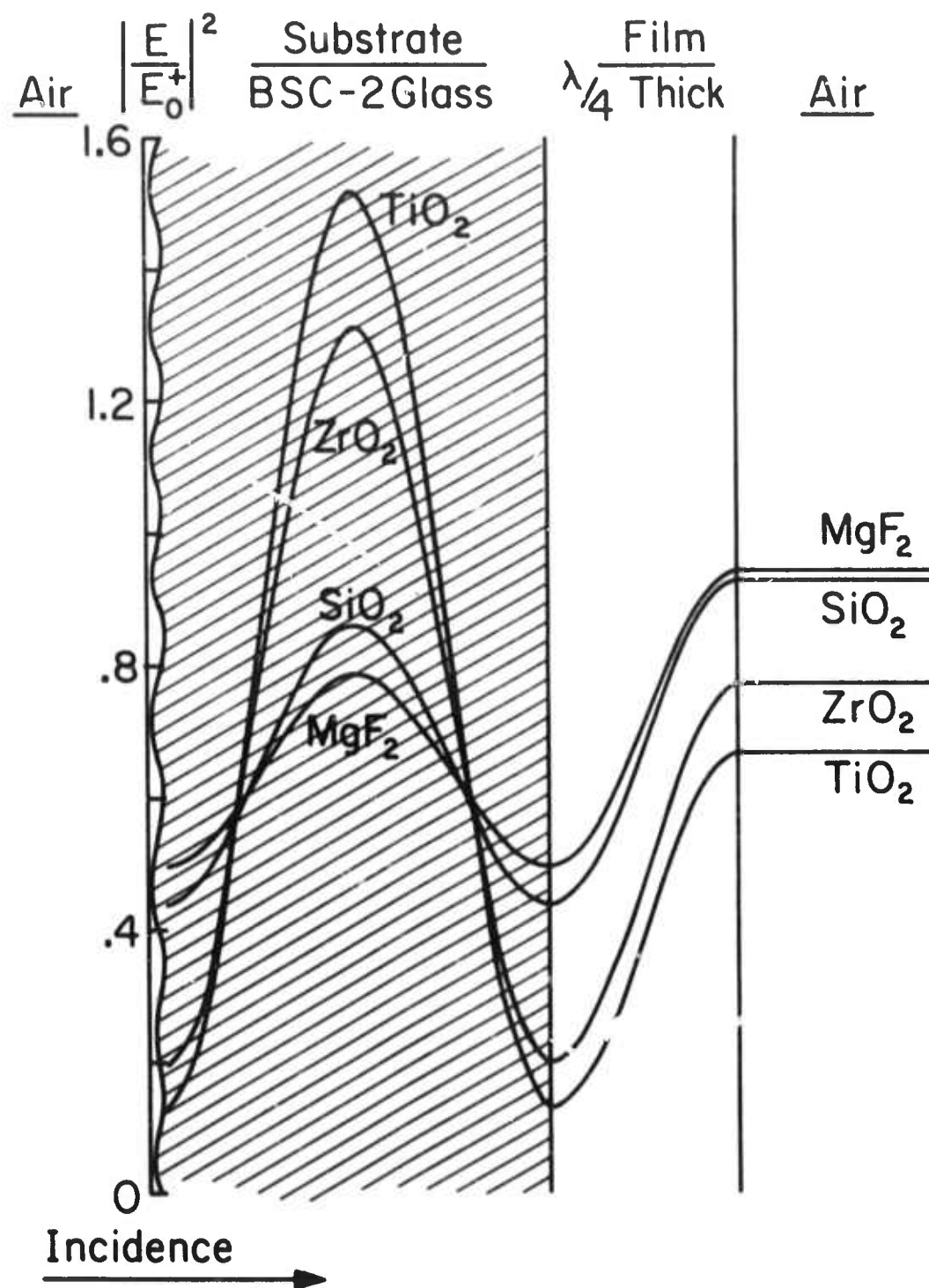
Figure 30. Relative electric-field intensity distributions
for quarter-wave films coated on the exit
face of BSC-2 glass substrates.
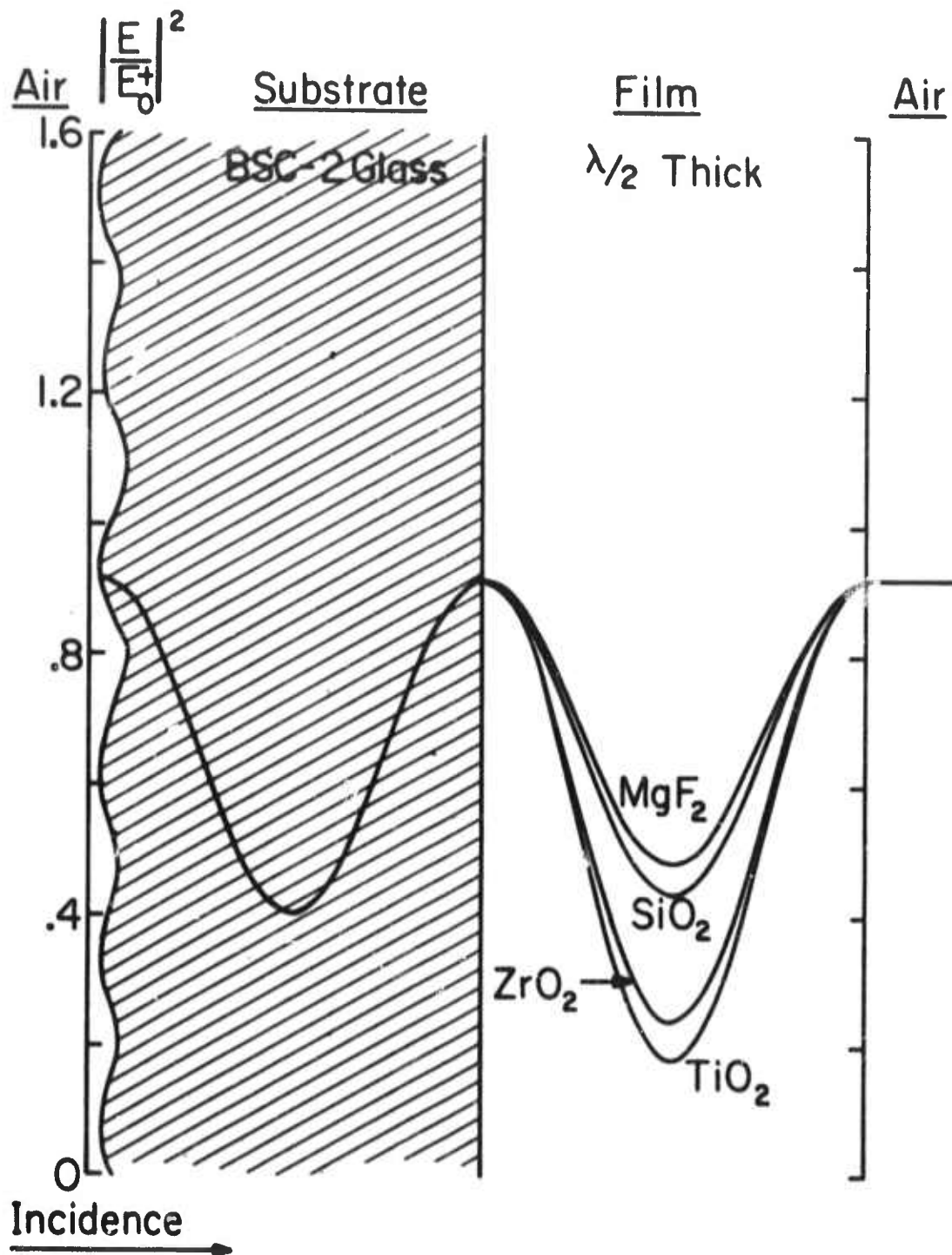
Figure 31.   Relative electric-field intensity distributions for
half-wave films coated on the exit face of BSC-2
glass substrates.

The electric-field intensity distribution in an exit-surface TiO_2/SiO_2 reflector is shown in Figure 32 and may be compared to the distribution in Figure 29 for the same reflector in the usual front-surface orientation. The maxima and minima occur at the layer interfaces for both orientations, but higher peaks are present in the reversed reflector. Another difference is that the extremely high peaks of the standing waves which occur in front of the reflector in Figure 29 are relocated in the glass substrate in Figure 32.

The peak values of the intensity are 45% higher for the reverse orientation and therefore by electric field considerations alone, the damage thresholds would be expected to be 45% less. However, the spark thresholds of reversed TiO_2/SiO_2 and ZrO_2/SiO_2 reflectors were only 20% and 30% lower and the ZrO_2/MgF_2 reflector was about 45% higher! Apparently the substrate caused no degradation of the threshold. Quite to the contrary, the substrate probably provided structural support to the adjacent layers which experienced the highest electric fields. Furthermore, the residual stresses in the layers near the substrate theoretically have less residual tensile stress than the layers near the air-film interface. It is then reasonable that the layers near the substrate are more damage resistant for a given energy density.

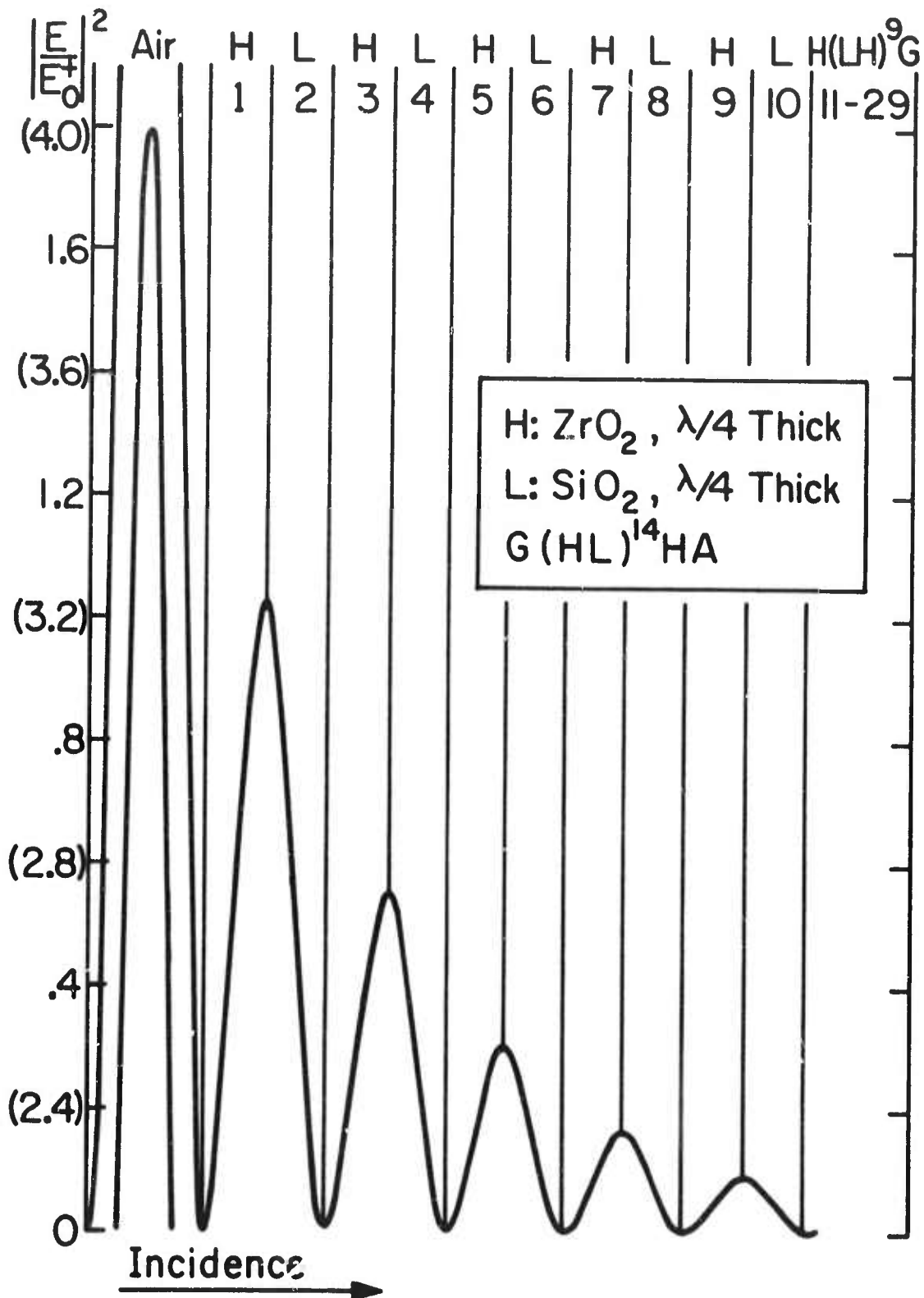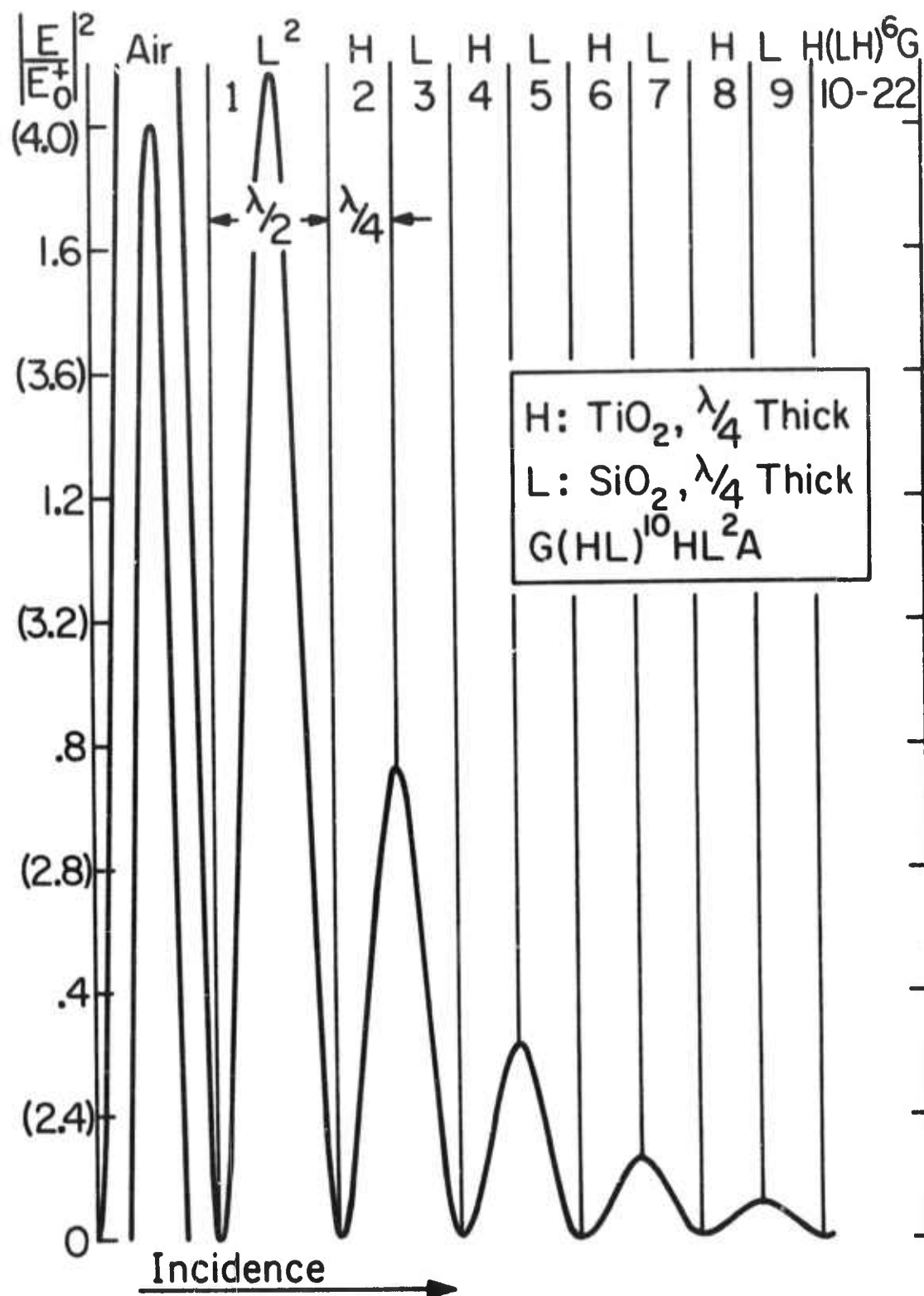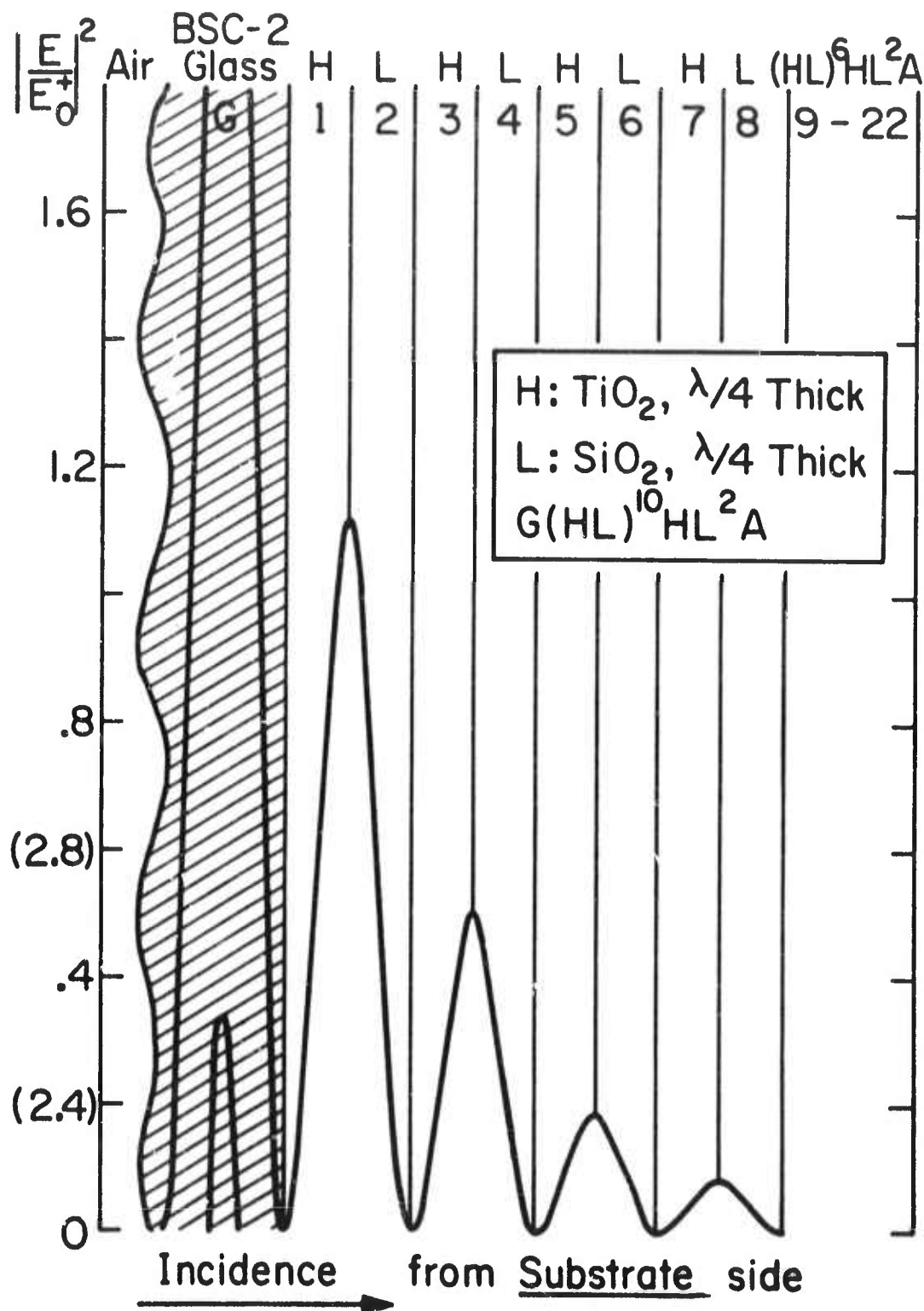Figure 32. Relative electric-field intensity distributions for a 22-layer TiO_2/SiO_2 reflector with $G(HL)^{10}HL^2A$ configuration coated on the exit face of a BSC-2 glass substrates.

V. ROLE OF COATING DEFECTS IN LASER-INDUCED DAMAGE TO THIN FILMS

1. Introduction

It is noted that in the literature the spot-size of the laser beam was seldom reported along with its corresponding laser-induced damage thresholds of laser materials. One of the most important experimental results in correlating laser parameters in this study is that the damage threshold of the thin film increases as the spot-size of the laser beam decreases. An 80% variation of damage threshold for the same film could be observed by just varying the spot-size.

In this report we develop a simple model correlating the nature and distribution of coating defects to this spot-size dependence. The model assumes that damage due to local defects or impurities in the film is different from the intrinsic damage of the material and that the defect sites are randomly distributed on the coating surface. The probability of the laser beam striking a defect site with a certain intensity can be calculated when the intensity distribution of the laser beam is known.

2. The Defect Model

For a random distribution of points on a plane, the probability that a randomly chosen area (e.g., a circle of radius r) will contain exactly n points can be described by the Poisson function

$$P(n) = \{ (\rho \pi r^2)^n / n! \} \exp (-\rho \pi r^2) \tag{5}$$

where ρ is the mean surface density of the defects. The probability that no points will be contained in this area is

$$P(0) = \exp (-\rho \pi r^2) \tag{6}$$

which is the probability that the area will contain no point within a distance r. Hence, the proportion of distances of nearest neighbors less than or equal to the distance r is

$$P(r) = 1 - \exp(-\rho\pi r^2) . \qquad (7)$$

Now, if r is allowed to vary, the probability distribution of r is then expressed as

$$dP(r) = 2\rho\pi r \exp(-\rho\pi r^2) dr . \qquad (8)$$

Thus, if we consider the case of a square pulse with width w less than or equal to r, the probability of such a pulse hitting one or more defects will be easily derived as

$$P(w) = 1 - \exp\left[-\frac{\pi}{4}(w/d_o)^2\right] \qquad (9)$$

where d_o is the expectation value of r, or the mean distance of two defects, and is related to the mean density ρ. In the actual case, a TEM_{00} ruby laser pulse was used so that the square pulse should be modified to the form of a Gaussian beam with spot-size w_o. Then, Eq. (9) becomes

$$P(w_o) = 1 - \exp\left[-\frac{\pi \ln 2}{8}(w_o/d_o)^2\right] \qquad (10)$$

Now, by assuming that the coating defects on a dielectric film surface have a damage threshold I_d (in joules/cm^2), much less than the intrinsic damage threshold I_i of the film, the total damage threshold I can be expressed in terms of the probability given in Eq. (10).

$$I = I_d P(w_o) + I_i \{1 - P(w_o)\}$$

To analyze our experimental data, it is convenient to normalize the total damage threshold I with respect to the defect damage threshold such that

$$\mathcal{J} = 1 + (\eta - 1) \exp\left[-\frac{\pi \ln 2}{8} (w_o/d_o)^2\right] \tag{11}$$

where we have defined the ratios $\mathcal{J} \equiv I/I_d$ and $\eta \equiv I_i/I_d$. If the distribution of defects on the coating is random, only one parameter, namely d_o, is needed to completely describe the distribution. I_d and η will be parameters which can be related to the type of defect, whether defect damage is associated to absorption or electron avalanche.

In a digression, let us take a closer look at the parameter η, which can be viewed as a function of the defect damage mechanism. A recent calculation by Bloembergen [22] concerning the role of pores in laser-induced damage to surfaces can be extended to structural defects in films. If a defect was a cylindrical groove on the surface, then

$$\eta = 4n^4/(n^2 + 1)^2 \tag{12}$$

which has a maximum value of 4 when the refractive index is infinite. If a defect was a needle cavity or the so-called 'crack' defect, which is an oblate ellipsoidal void in the surface, the enhancement factor η will have a much larger value of

$$\eta \sim n^4. \tag{13}$$

Other types of defects will have different values of the enhancement factor. Hence, the parameter η is very sensitive to the type of defect on the coatings or the surface of the bulk materials. Table 9 gives some estimates of the enhancement factor η for five different films.

To illustrate the results of such a probability model, Figure 33 displays a theoretical plot of the total damage threshold I
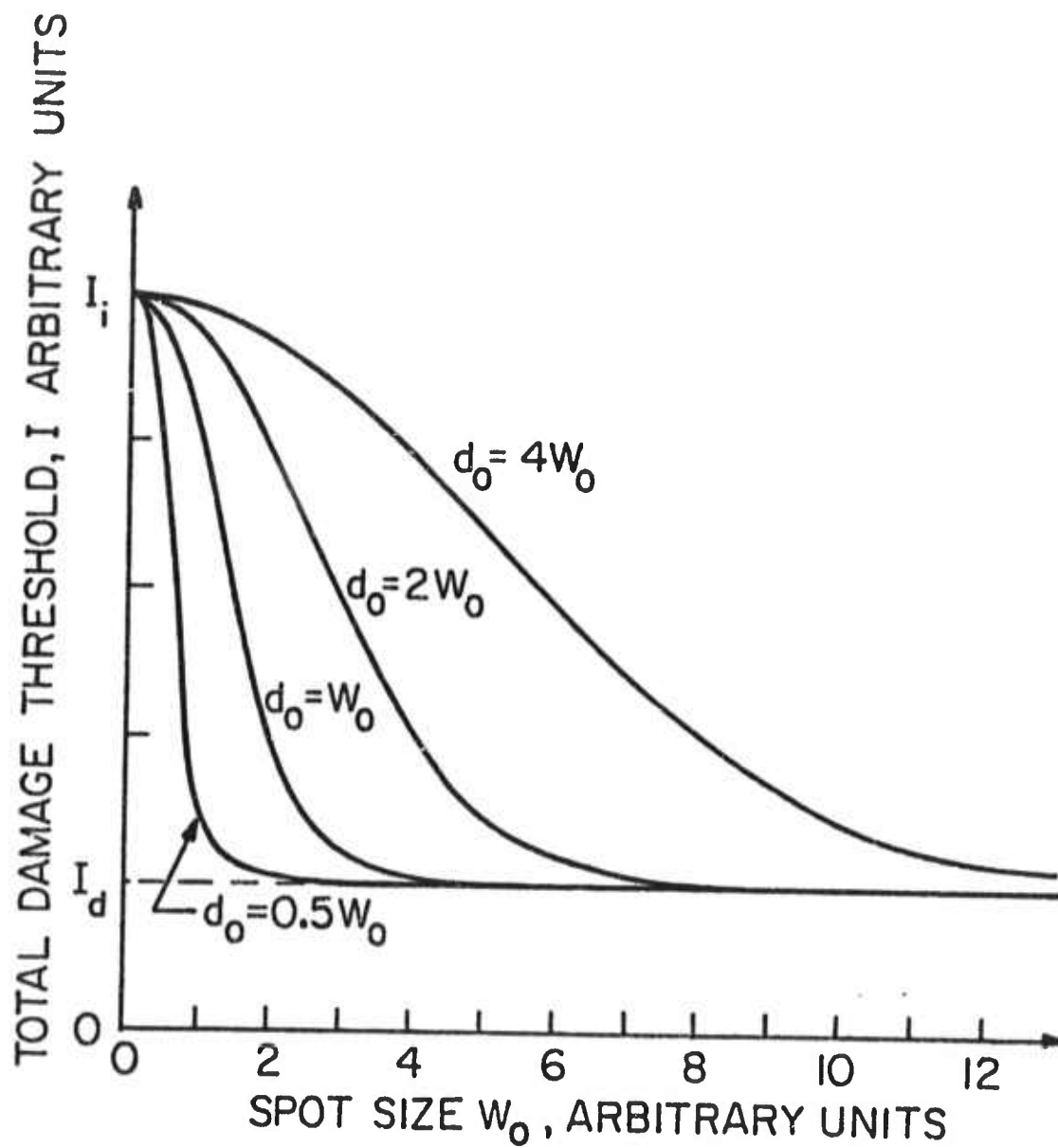
Figure 33. Theoretical plot of the total damage threshold versus spot-size.

versus spot-sizes w_o. For very large spot-sizes, the measured threshold will be the defect damage threshold I_d. For decreasing spot-sizes, the damage threshold will follow a variety of curves depending on the distribution of defects, e.g., the mean distance d_o. In the case of thin-film coatings, the damage thresholds are very low because d_o is a small fraction of the spot-sizes used in the usual laser damage tests. Hence, the curve is similar to the one for $d_o = 0.5\,w_o$, and the threshold value is close to the defect damage I_d and not to the intrinsic damage, I_i. However in the case of single crystal damage studies, e.g., for NaCl [23] the spot-size is very small with respect to the defect distance d_o. Then the curve is similar to the one for $d_o = 4\,w_o$, and in fact, the measured threshold would be very close to the intrinsic damage I_i. Therefore, using this model both thin film and surface damage can be related for a single material.

Table 9. Some estimates of enhancement factor η due to structural defects

Sample	n	Groove $\eta = 4n^4/(n^2+1)^2$	Crack $\eta \sim n^4$
ZnS	2.32	2.84	29
TiO$_2$	2.28	2.81	27
ZrO$_2$	1.98	2.54	15
SiO$_2$	1.46	1.84	4.5
MgF$_2$	1.38	1.71	3.6

3.   Experimental Results

The descriptions of the experimental setup (see Fig. 3) and procedure used in this experiment can be found in Section II and III.   Three methods were used to monitor the onset of the damage: spark detection, optical microscopy and laser-induced scatter (LIS). However here we emphasize that the LIS technique was our primary tool for diagnosis.   Spot-sizes ranging from $52\mu m$ to $280\mu m$ were used and areas of a test sample were irradiated by one shot only. The mean distance d_o between defects of each sample was determined by measuring the density of coating defects for ten randomly chosen areas on the sample, which was examined under a scanning electron microscope with magnification of 1000.

A half-wave film of ZrO_2 and a quarter-wave film of ZnS with glass substrate were used in studying the spot-size dependence on damage thresholds.   By varying the spot-size of the laser beam, damage thresholds were determined by the onset of LIS.   The laser pulsewidth was 8 nsec.   Figures 34 and 35 display the experimental data as well as the theoretical curves using the forementioned defect model.   For ZrO_2 film, the defect damage threshold I_d was found to be 9.2 joules/cm^2 and the data was fitted to a curve with η of 3 and d_o of 20.4 microns.   Figure 36 compares damage data for three other coatings to the curves derived from the defect model. For the plotting of this data, d_o was measured by SEM photographs and was not fitted.   The sketchy nature of the data for these three coatings prevented an accurate determination of the enhancement factor η, but it is to be noted that the data was consistent with the model.
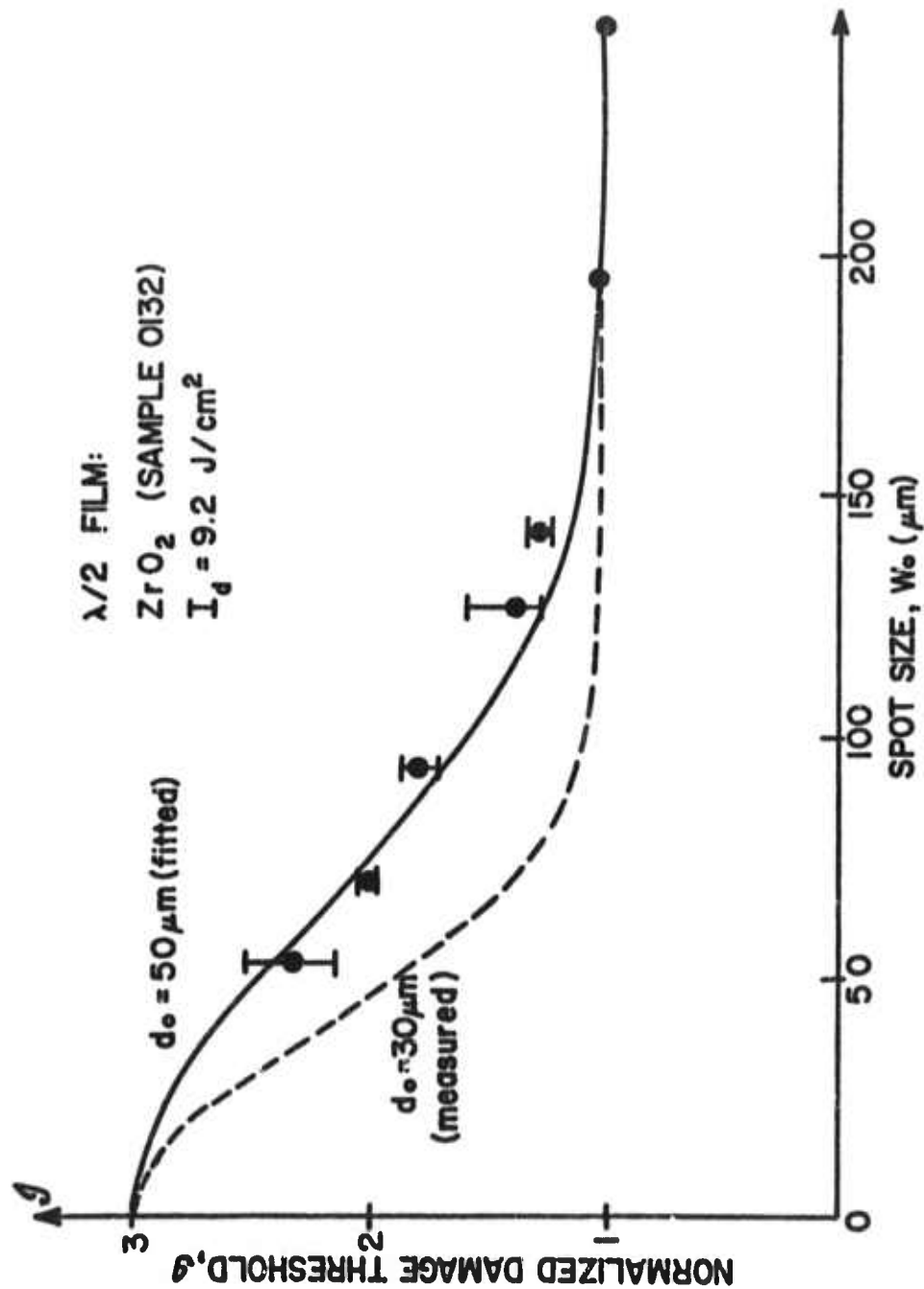
Figure 34. Spot-size dependence for single half-wave thick film of ZrO_2 on BSC-2 glass substrate. $\mathcal{J} = I/I_d$ and $\eta = I_i / I_d$.
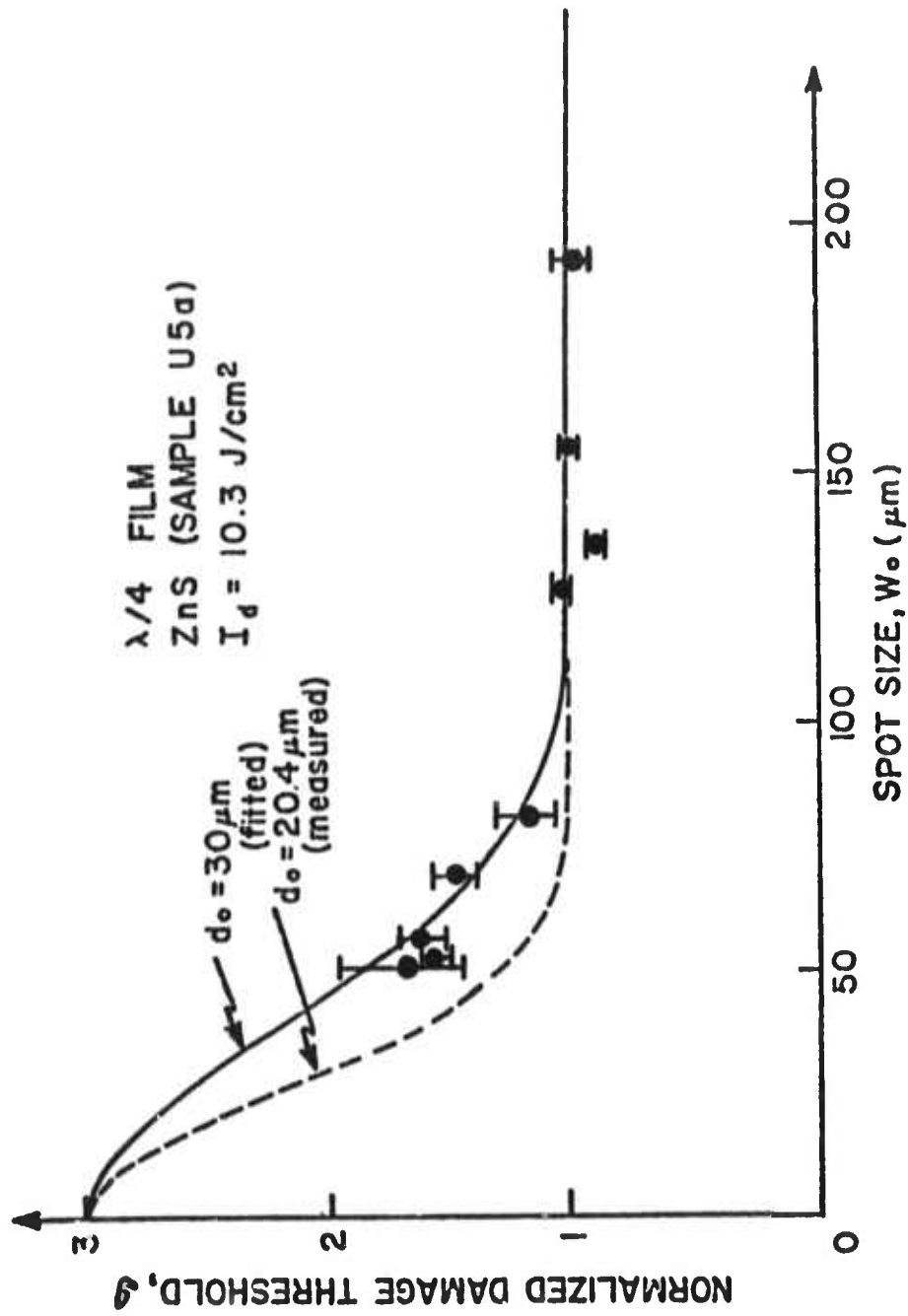
Figure 35.   Spot-size dependence for single quarter-wave thick film of
ZnS on glass substrate.

63.
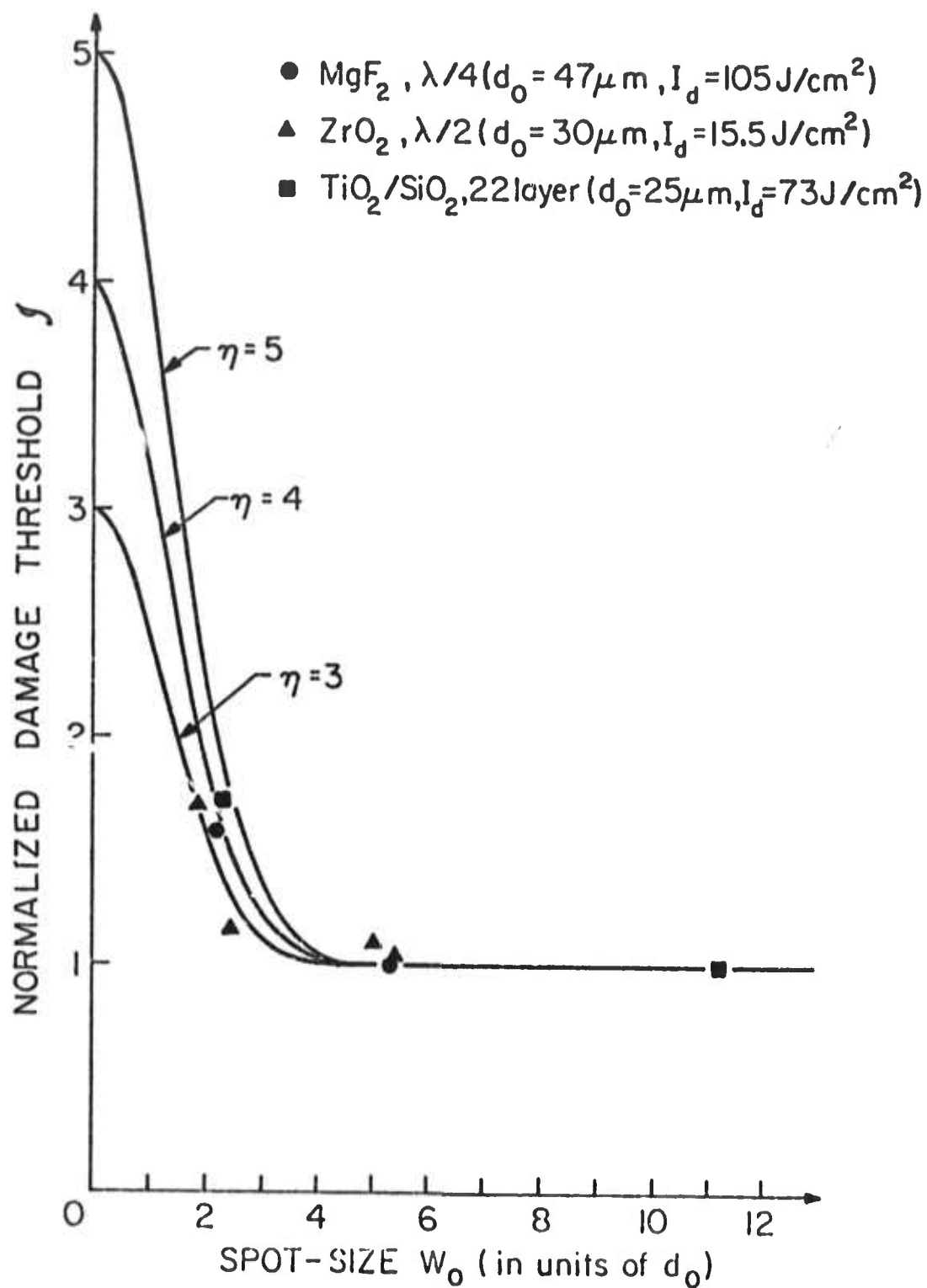
Figure 36. Normalized damage threshold as a function of
laser beam spot-size including the role of
local defects. The range of spot-size is 55
to 200 microns.

4. The Role of Coating Defects

A closer look at the morphology of the coating defects
or impurities on the films using the electron microscope has indicated
that defects are irregular both in sizes and shapes and the density
may strongly depend on several film parameters and preparation
methods. In general, six types of defects were observed. Figures
37 to 43 show that such local defects can be found in different films.
For the ZnS film used in the experiment, five types of defects were
found (see Fig. 44). It is recalled that the measured d_o was 20.4
microns and the fitted d_o was 30 microns, which indicates that the
damage may be primarily caused by those defects having irregular
forms (or "mountain chains") and "shadows with strips". One can
also easily observe in this case that a small mean distance between
defects occurs for the most prevalent defect, "shadows with a dot".

By examining coating procedures, one may be able to
change the mean distance between coating defects. At USC, we have
attempted to vary the coating defects on one type of film by varying
the deposition rate in the preparation of the coatings. It was found
that by doing so, d_o decreases as the deposition rate increases.
Figure 45 simply illustrates this result for MgF_2 films. The idea
was then to damage all three of these films of the same material
and find out how it relates to the parameter d_o.
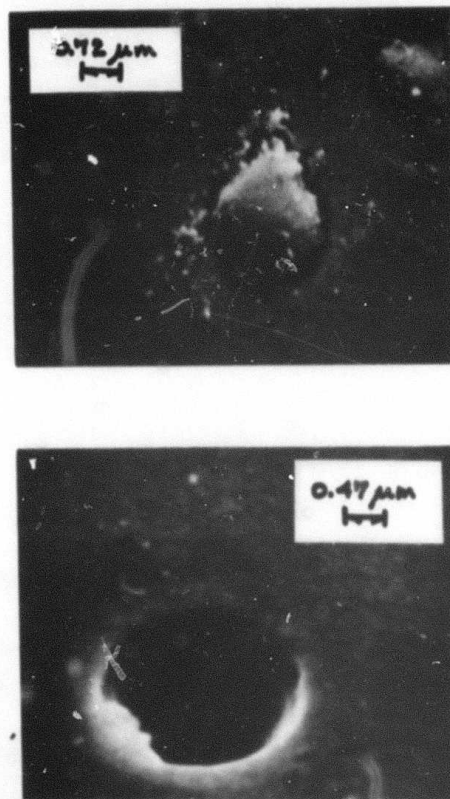
Figure 37. Scanning Electron Microscope (SEM) photograph of
defects of the two extreme forms, a hill (upper) and
a hole (lower), on an eleven layer CeO_2/SiO_2 reflector.
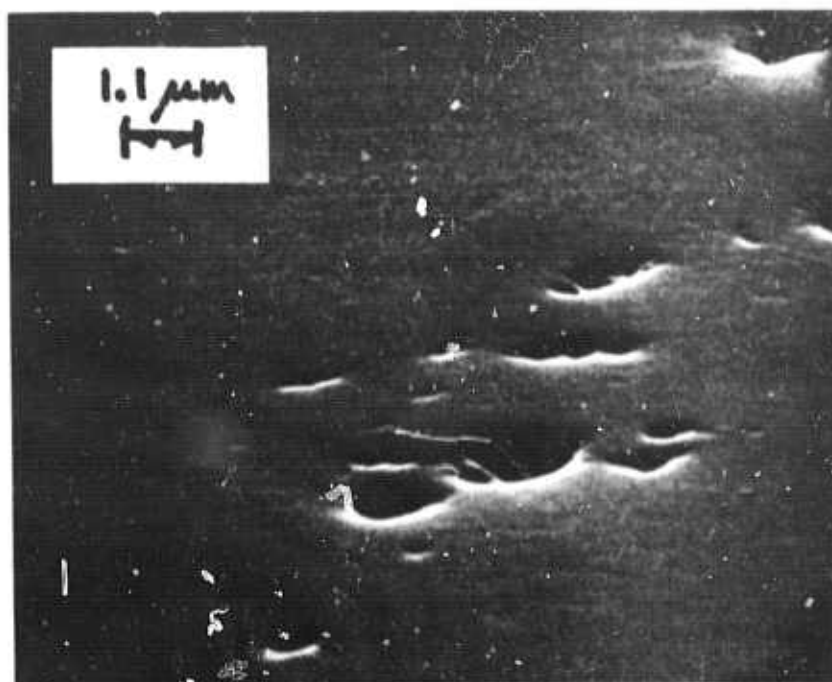
Figure 38. SEM photograph of defects of a group of holes on a single quarter-wave MgF_2 film.
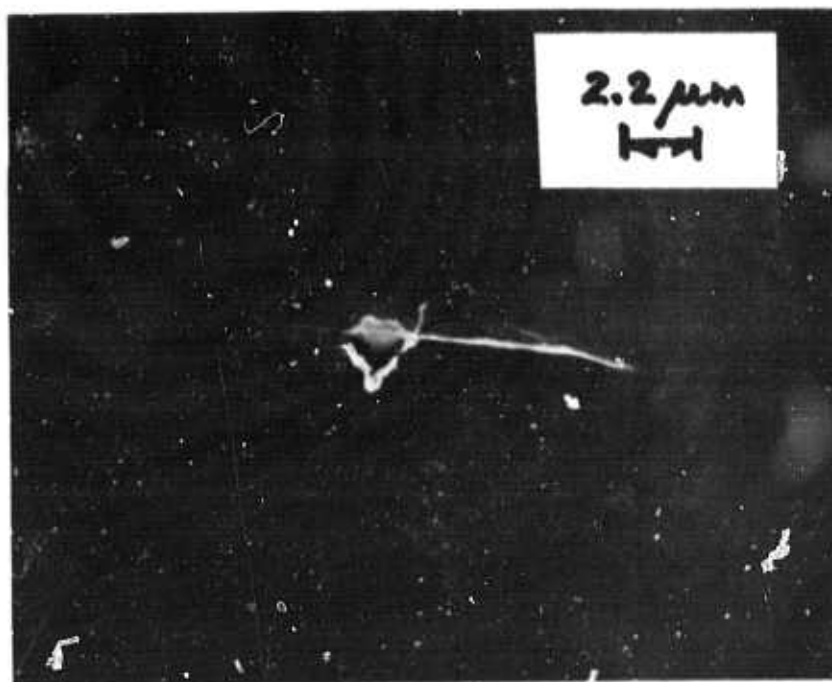
Figure 39. SEM photograph of defects in the form of a crack on a single quarter-wave MgF_2 film.

67.
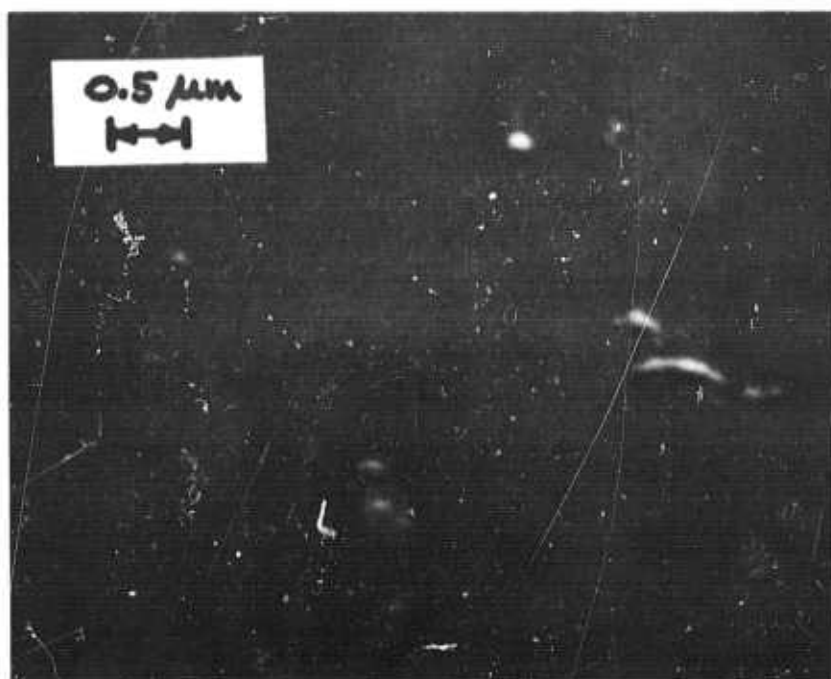
Figure 40.   SEM photograph of defects in the form of irregular
shaped hills, or "mountain chain," on a single
quarter-wave MgF$_2$ film.
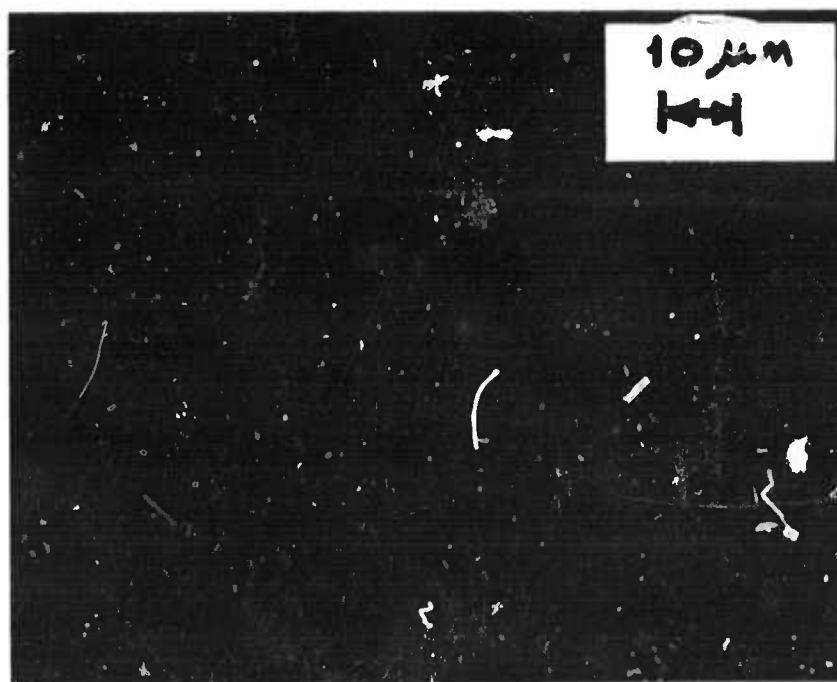
Figure 41.   SEM photograph of defects in the forms of shadow
with dot, crack and hill on a single quarter-wave
ZnS film.
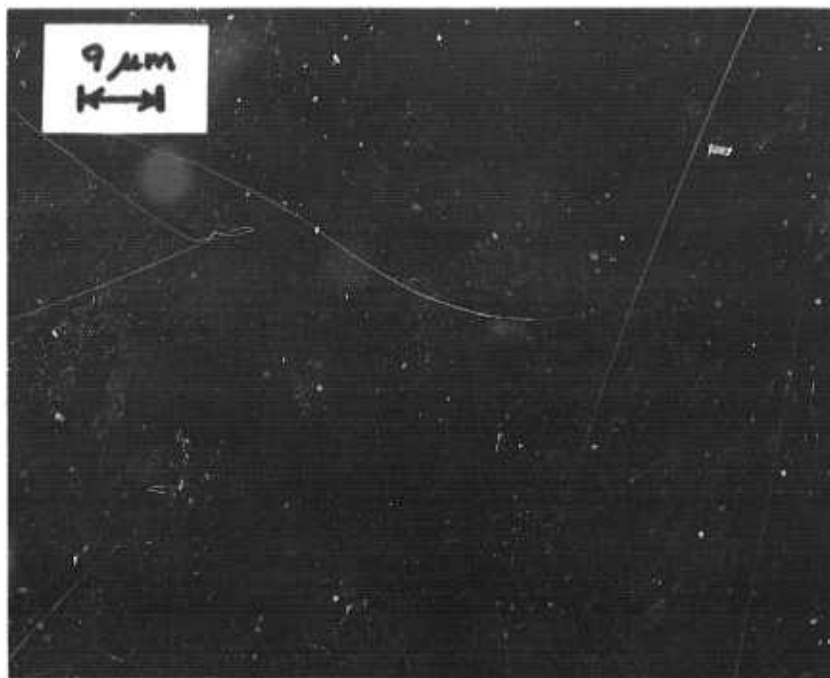
Figure 42.   SEM photograph of defects in the form of "shadow with strips" on a single quarter-wave ZnS film.
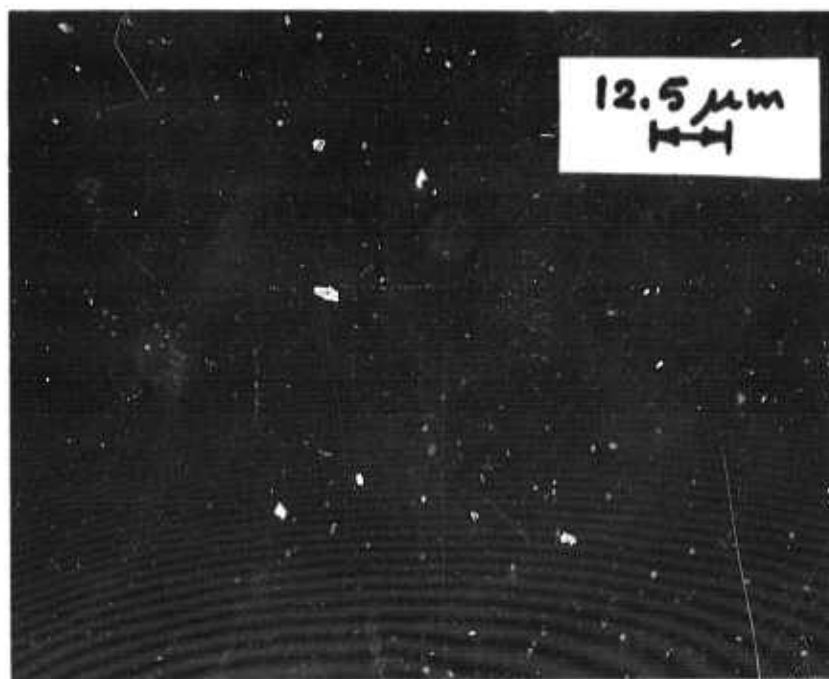
Figure 43.   SEM photograph of clean area (no defect observed) on a single quarter-wave MgF_2 film.
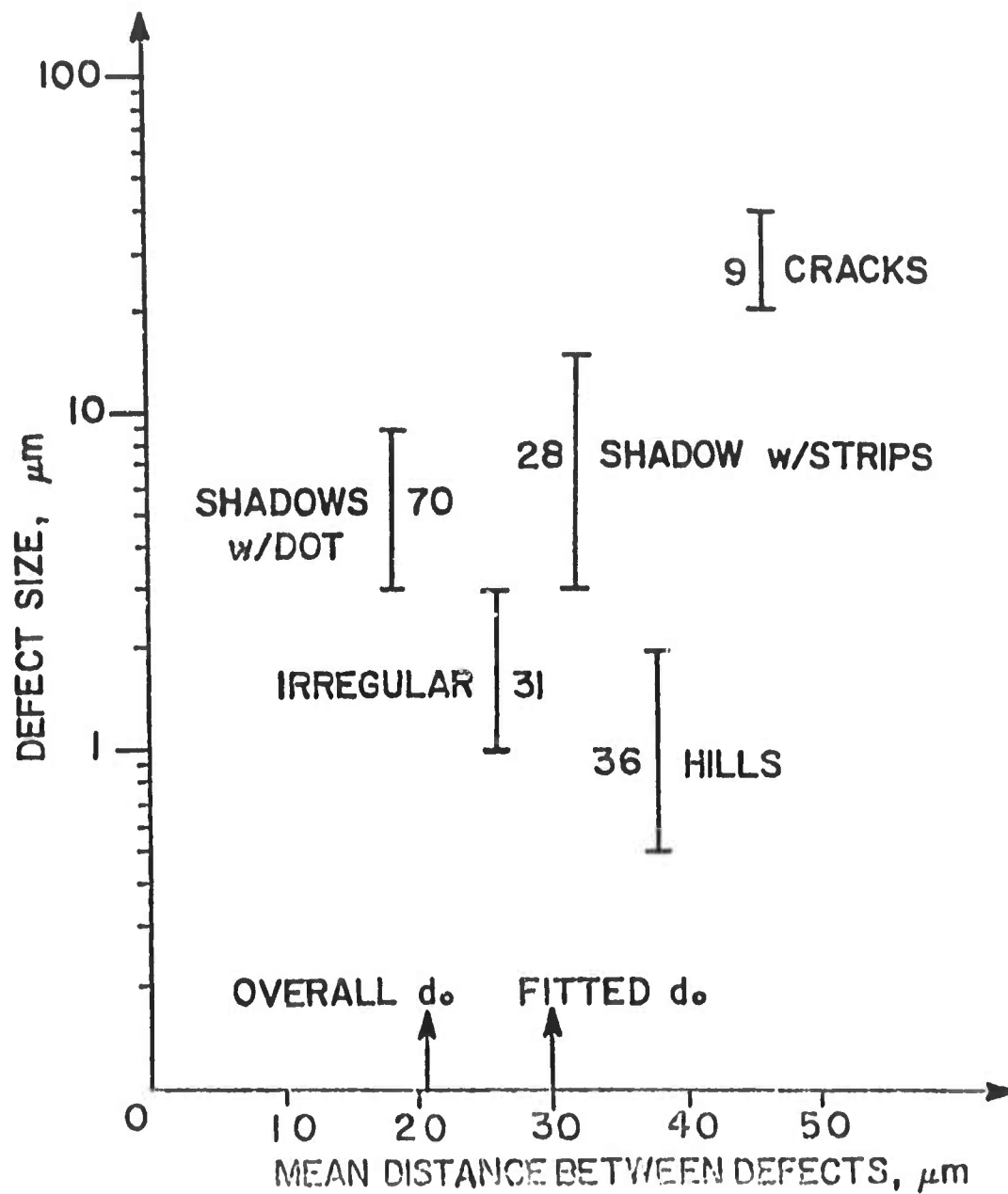
Figure 44. A schematic plot of size versus distribution and nature of coating defects, for a single quarter-wave film of ZnS (sample number U5a).
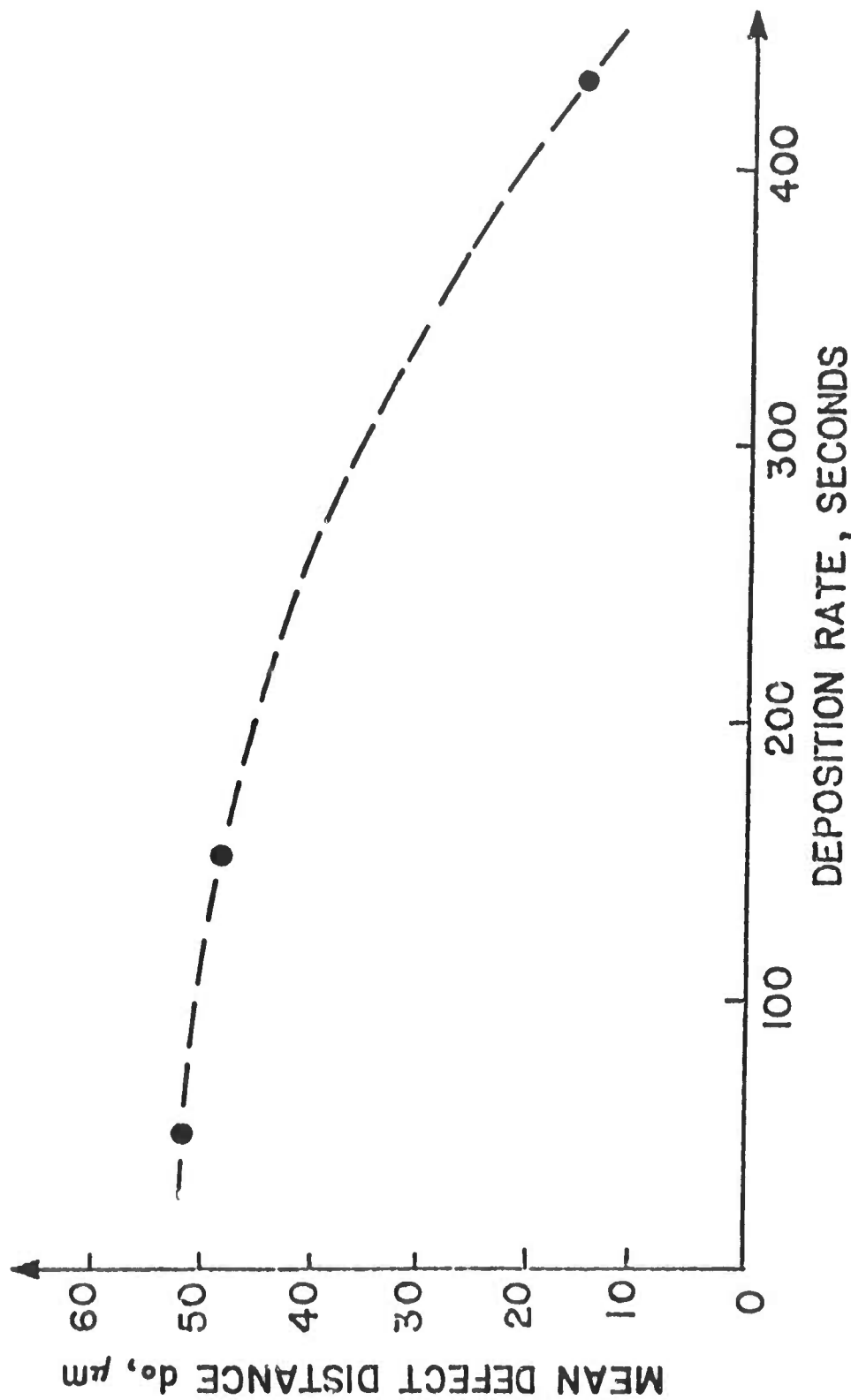
Figure 45. Mean defect distance d_o versus deposition rate for single quarter-wave films of MgF_2.

VI.   OTHER LASER PARAMETERS

As described in Section II, knowledge of the spatial and
temporal behavior of the laser beam, and hence the mode properties
of the laser, is required for an accurate prediction of damage.
Furthermore, if we want to know whether or not time-dependent
damage mechanisms are involved, correlation of the damage threshold
to the laser pulsewidth should be studied.   In this program, two experi-
ments were performed to investigate thin-film damage as a function
of these two laser parameters, namely, the transverse mode struc-
ture and the pulsewidth of the laser.

1.   Damage by Multimode Lasers

For the multimode damage study, the ruby laser
oscillator was adjusted to have a Fresnel number of 8.0 instead of
0.4, which allowed the oscillator to operate in many transverse
modes.   For our laser, the cavity Fresnel number of 8.0 corresponded
to an aperture having a diameter of 4.47 mm.   The test samples were
placed at approximately 20 cm after a 31-cm focal length lens located
at 116 cm from the aperture.   In single-mode operation, the lens
would see a far-field diffraction pattern at this distance (1.3R) [24]
but it was in the near-field distances of the samples from the aperture
were computed to be approximately 0.125R by using the geometrical
lens transformation.

The damage thresholds (spatial averages) of these
dielectric reflectors (samples S101, 102 and 103) are listed in Table
10 for near-field, non-single transverse-mode laser irradiation.
Shown for comparison are the average, single-mode thresholds com-
puted from the data given in Table 4 of Quarterly Technical Report
No. 4.   An "average" energy-density threshold for a Gaussian trans-
verse intensity is defined by $E = E_T / \pi w^2$.   This average is equal to

71.

one-half the axial energy density prescribed. Because multimode
emission is temporally unstable, theoretical computations by
McAllister [25] of the time-dependent intensity distributions plus
geometrical lens optics were used to estimate the spot-size at the
sample locations. Since these measurements were performed prior
to incorporating the spark detection system, the thresholds of the
reflectors were established using low-power (7 X and 40 X) microscopes.
Taking into account the differing sensitivity of the detection methods,
the multimode thresholds were still considerably less than those for
single-mode pulses. A typical comparison of damage morphology
due to these two different pulses can be found in Figure 46.

Table 10. Damage thresholds for non-single transverse-mode laser
irradiation (nominal pulsewidth is 16-18 nsec)

Sample	Description	Spot-size, Average	Average energy density	Peak power Density, avg.
		mm	J/cm^2	GW/cm^2
S101	TiO_2/SiO_2	0.65	10 (22-28)	0.6(1.5-2.0)[a]
S102	TiO_2/SiO_2	0.8	7 (25)	0.4(1.8)
S103	ZrO_2/SiO_2	1.2	3 (4)	0.14(0.26)

[a]For comparison, damage thresholds for single-mode laser irradiation
are given in parentheses.

The damage thresholds of thin film coatings for multi-trans-
verse-mode (MM) laser radiation were much lower than for single-trans-
verse-mode (SM) radiation. For the three multilayer samples listed in
Table 10, the energy density thresholds for MM radiation were 40%,
30% and 75% of the respective SM thresholds. Apparently, the more
damage resistant the coating, the greater the difference between MM
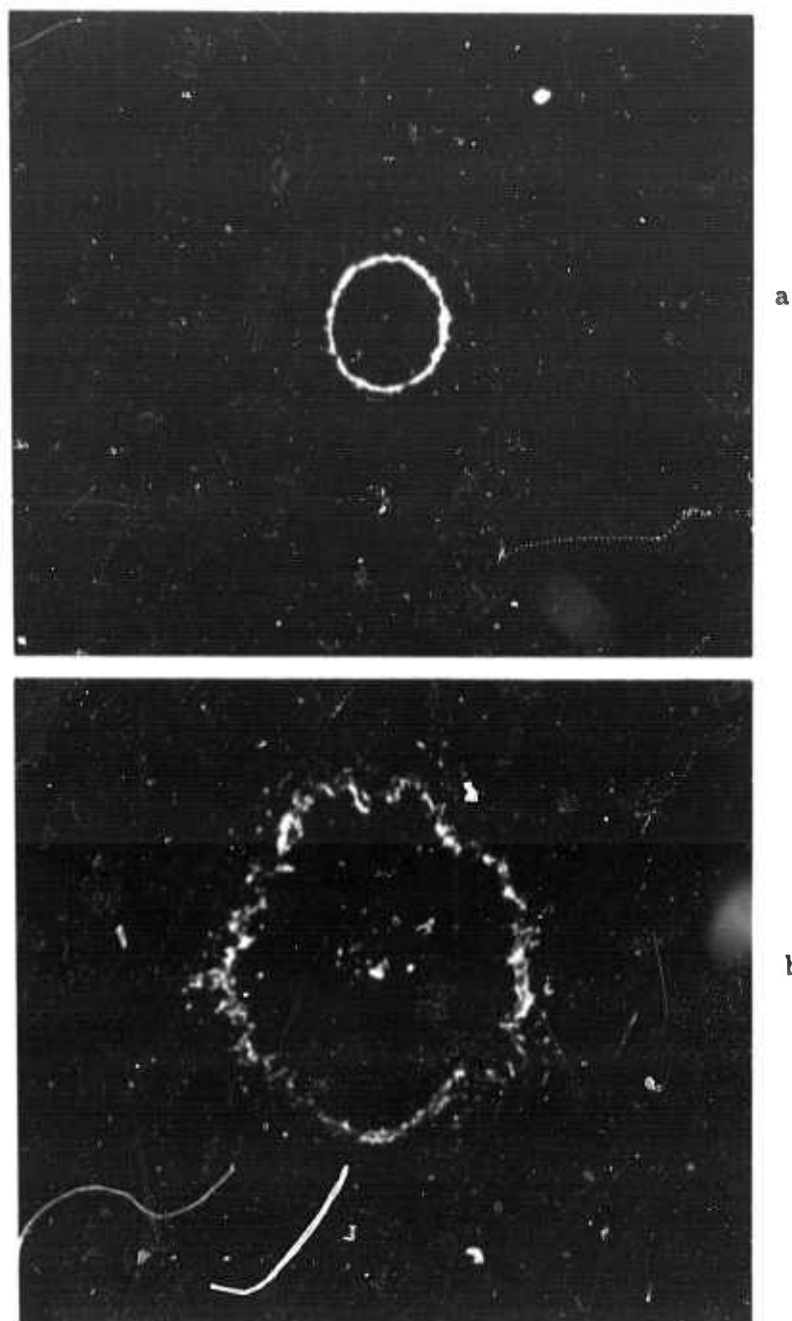
Figure 46.   Laser-induced damage far above threshold on a
TiO_2/SiO_2 multilayer reflector (Sample S102)
caused by the output of (a) a single-mode oscillator
and (b) a multi-transverse-mode oscillator.   Damage
at film defects is apparent.   Photographed with dark-
field illumination.   Magnification: 120 X .

and SM thresholds.   It is only apparent that the ratios for MM to SM power density thresholds are even lower than those for energy density. When the longer pulsewidths used in the MM tests are taken into account, the ratios are about the same for both.   Theoretical calculations of the MM output have shown that spatial nonuniformities in the power-density distribution at a given instant in time can be considerably more severe than for the energy-density distribution which is an integration over the pulse duration.   A larger difference for power-density thresholds would have indicated that the damage mechanisms are strongly time dependent in this pulsewidth range.   Thus the experimental thresholds indicate the contrary.

The calculation of the MM thresholds was very approximate because the spatial distribution of the output at the sample plane was both radially nonuniform and time dependent.   Numerical calculations of the theoretical intensity distributions at three different times during a single pulse were supplied by McAllister [25] and are shown in Figure 47.   Each curve is normalized to its peak radial value, and radial distances are normalized to the aperture radius a. The curves represent the output in the plane of the irradiated samples which was 0.125R from the laser.   This distance is in the near diffraction field at which the oscillator aperture subtended four Fresnel zones as viewed by the samples.

The temporal and spatial structure of this MM output was semi-controlled by use of an aperture which set the oscillator Fresnel number N equal to 8.0.   Without the aperture, N would have equaled 16 as established by the diameter of the ruby rod, and an even more erratic temporal and spatial output would have resulted.   Additional computer analysis of the laser output at several distances in the near and far fields revealed that the spatial nonuniformities at a given instant decrease with increasing distance, but temporal variations persist.   For example, at one Rayleigh distance (7.2 meters from the 4.47 mm aperture) the radial distribution is Gaussian-like during the
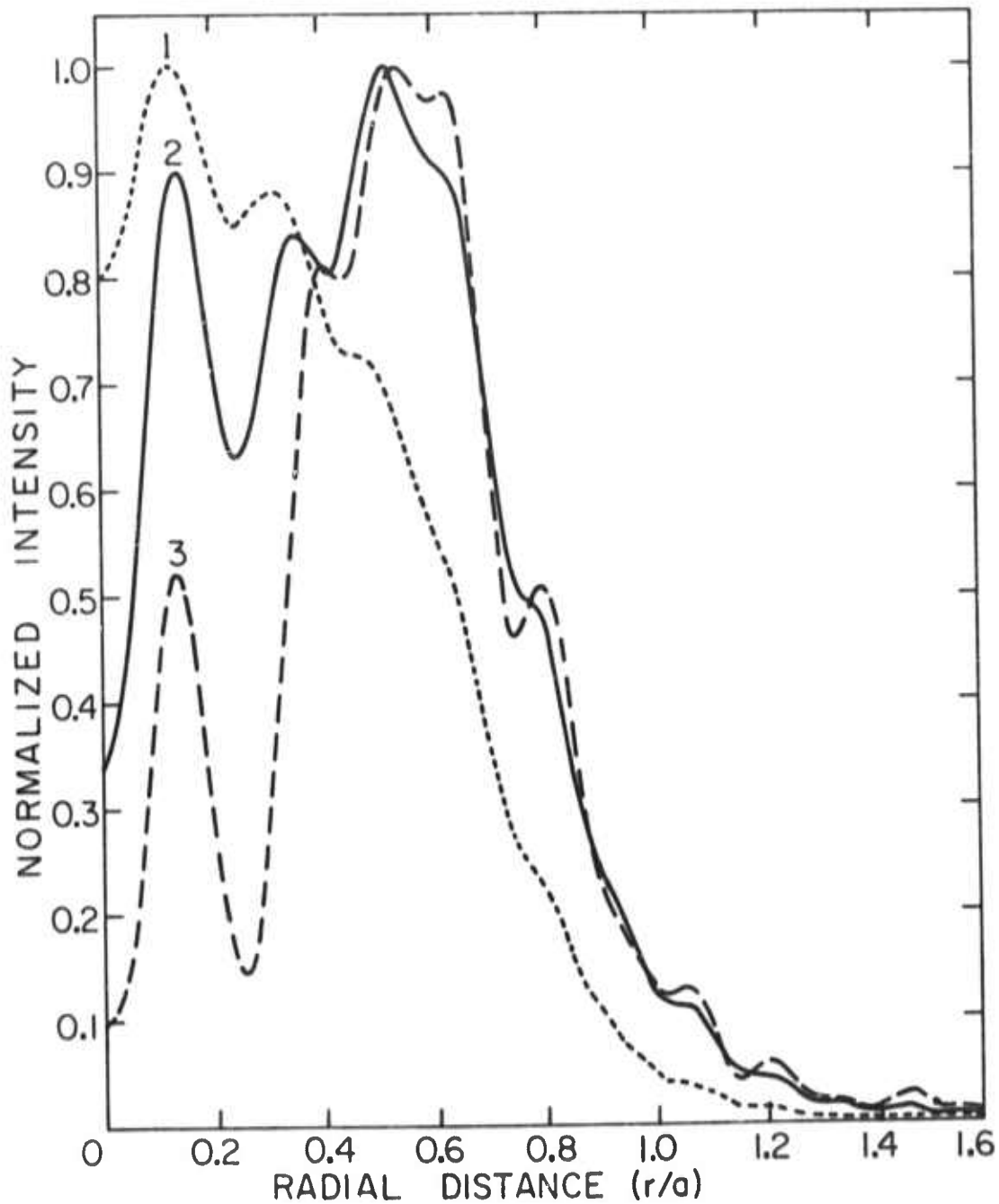
Figure 47. Theoretical transverse intensity distributions for the output of a multi-transverse-mode ruby laser (N=8.0) at 0.125 R from the oscillator aperture. Curve 1 (3) occurs during the rise (fall) of the temporal pulse when the total power equals 0.51 (0.55) the peak power. Curve 2 occurs at the pulse peak.

entire pulse, but the spot-size severely decreases in time after the pulse peak.

The damage thresholds of thin film coatings irradiated by MM laser pulses were considerably _lower_ than with SM pulses. This is in agreement with the results of two other investigators for other dielectric surfaces. Izamitani, Hosaki and Yamanaka [26] measured the single-shot MM surface damage threshold of Hoya glass to be about one-half the value of the SM threshold which was 28 J/cm^2. Similarly, Bass [27] determined that the surface damage threshold of $LiNbO_3$ caused by a single pulse from a multimode Nd:YAG laser was 0.8 GW/cm^2 (average) in contrast to that caused by a SM pulse of average power density equal to 1.6 GW/cm^2. The lower damage resistance to MM pulses is in agreement with the general results of our thin film experiments. Relative "hot spots" in the MM transverse beam profile or excitation of additional damage mechanisms by en-hanced temporal and spatial gradients may cause early damage. It is not clear that these are the only possible explanations. The difficulty in performing accurate calculations of the MM power may well be responsible for some of the apparent difference [28].

2. Damage by Different Pulsewidth of the Laser Beam

Single, half-wave layer ZrO_2 films were irradiated by the ruby laser using 11 to 35 nsec pulsewidths. The damage thresholds, shown in Figure 48, exhibited an interesting dependence on pulse duration. The threshold detected by LIS increased by 36%, from 12.5 to 17 J/cm^2 over the pulsewidth range of 13 to 32 nsec. Over the same temporal range, the spark threshold rose from 17.5 to 30 J/cm^2, an increase of 67%. The slopes of the straight lines drawn between the data points lie between the hypothetical, constant energy-density curves (horizontal lines) and the constant power-density curves (drawn through the shorter pulsewidth data points). Apparently, the energy requirements for spark formation were more time dependent than

those required to increase the surface scatter. Conduction of thermal energy from the irradiated sites during the duration of the pulse can be ignored since $(D\tau)^{1/2} \ll w_o$ (e.g., the diffusivity D of ZrO_2 is 0.81×10^{-2} cm^2/sec, pulsewidth is 32 nsec and the spot-size is 72 μm).

Now, Bliss and Milam [29] recently measured the damage thresholds of a TiO_2/SiO_2 multilayer reflector with a single-mode ruby laser to be about 2 and 50-60 J/cm^2 for pulsewidths of 20 psec and 20 nsec, respectively. It is reasonable to assume that the minimum threshold of a single layer of ZrO_2 for very short pulses is also near 2 J/cm^2. Extrapolating the straight lines in Figure 48 to shorter pulses, the threshold of 2 J/cm^2 is reached at 5 nsec for spark detection and at 1.5 nsec for LIS detection. These pulsewidths are much larger than the 20 psec used by Bliss and Milam; so it is plausible that the energy-density threshold could well be a constant value over the range of 20 psec to 2 nsec.

This temporal dependence of the damage threshold of ZrO_2 is similar to that described by Bliss [30] for damage caused by an electron avalanche breakdown. According to his analysis, the dependence of the threshold energy density on pulse duration changes from linear with τ for long pulses to independent of τ for short pulses. This result assumes that the lifetime τ of electrons in the conduction band is long compared to the time t' required to accelerate an electron to the energy of the conduction band.
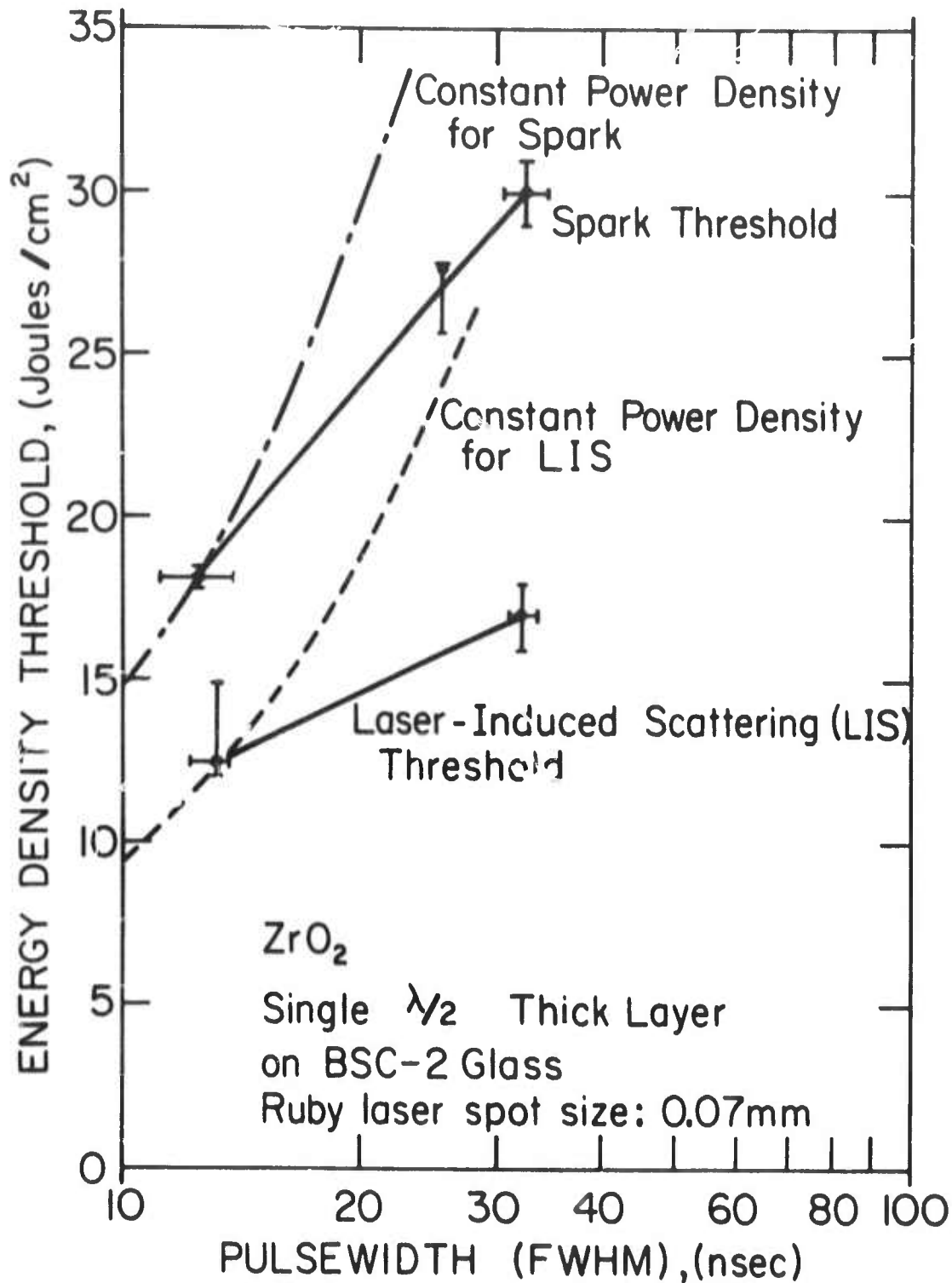
Figure 48. Laser pulsewidth dependence of the damage thresholds
for a single half-wave thick film of ZrO_2 on BSC-2
glass. Damage was detected by both laser-induced
scattering and spark formation. Deviation from con-
stant power density thresholds is indicated by dashed
curves.

VII.   COATING PARAMETERS

1.   Introduction

Unlike the bulk and surface damage studies in trans-
parent dielectrics, the understanding of damage in dielectric thin-film
coatings is exceedingly difficult due to the variability of certain film
properties due to coating procedures.   Our approach to this multi-
variable problem was not to attempt either to establish any one coating
procedure or to control any particular coating property, but to use
"state-of-the-art" coatings obtained from commercial sources.   In
particular, the coating configurations studied were: (1) single-layer
dielectric coatings of different materials and thickness, (2) bi-layer
antireflection coatings of different materials, (3) multi-layer reflectors
of different materials and varied number of layers, and (4) substrate of
different materials.   In addition, absorption by thin-film systems was
analyzed and other possible damage mechanisms were examined.

2.   Single-layer Coatings

a.   Film Materials

The damage thresholds for single, quarter-wave thick
films of MgF_2, SiO_2, ZrO_2, TiO_2, and ZnS on polished BSC-2 glass
substrates are listed in Table 11 in the order of increasing refractive
index at 6943Å.   The thresholds are seen to monotonically decrease
with increasing film index (see Fig. 49).   It can also be seen that the
LIS technique was the most sensitive in these threshold measurements
for single-layer coatings.   The correlation with index is expected,
since by the classical theory of H. Lorentz a low index is associated
with a large energy gap between the valence and conduction bands.
This decreases the likelihood of absorption.   A more detailed dis-
cussion on the role of absorption as a damage mechanism can be
found in Section VII.6.

Table 11. Damage thresholds for quarter-wave single coatings (nominal pulsewidth, 11-13 nsec).

Sample	Material[a]	Refractive Index (6943 Å)	Spot size	Peak energy density		Peak power density		Ratio of spark to LIS
				by spark	by LIS	by spark	by LIS	
			mm	J/cm^2		GW/cm^2		
O133	MgF_2	1.38	0.055	111-131	111-131	8.2-9.3	8.2-9.3	1.0
O125	SiO_2	1.456	0.055	>125	117	>10.5	10.5	>1.1
O129	ZrO_2	1.975	0.072	61-68	35-44	4.3-4.9	2.4-3.2	1.6
O121	TiO_2	2.28	0.072	57-71	35-42	4.2-5.7	3.0-3.9	1.7
U203	ZnS	2.35	0.072	63	5.5-12.5	4.7	0.4-0.85	>5

[a] All substrates are BSC2 glass.

Table 12. Damage thresholds for various film thicknesses[a]

Sample	Film	Spot size	Peak energy density	Peak power density
		mm	J/cm^2	GW/cm^2
O133	MgF_2, $\lambda/4$	0.055	111-131	8.2-9.3
O135	MgF_2, $\lambda/2$	0.065	65-102	5.3-8.1
O125	SiO_2, $\lambda/4$	0.055	117	9.8
O127	SiO_2, $\lambda/2$	0.055	>111	<9.9
O129	ZrO_2, $\lambda/4$	0.072	36-44	2.4-3.2
O131	ZrO_2, $\lambda/2$	0.072	12-13	0.85-0.90
O121	TiO_2, $\lambda/4$	0.072	36-42	3.0-3.9
O124	TiO_2, $\lambda/2$	0.097	7-8	0.55-0.65
O137	TiO_2, $3\lambda/4$	0.072	17.5-25	1.4-2.2
		0.122		
O138	TiO_2, $3\lambda/4$	0.072	20-23	1.4-1.5

[a] Damage detected by laser-induced scatter.
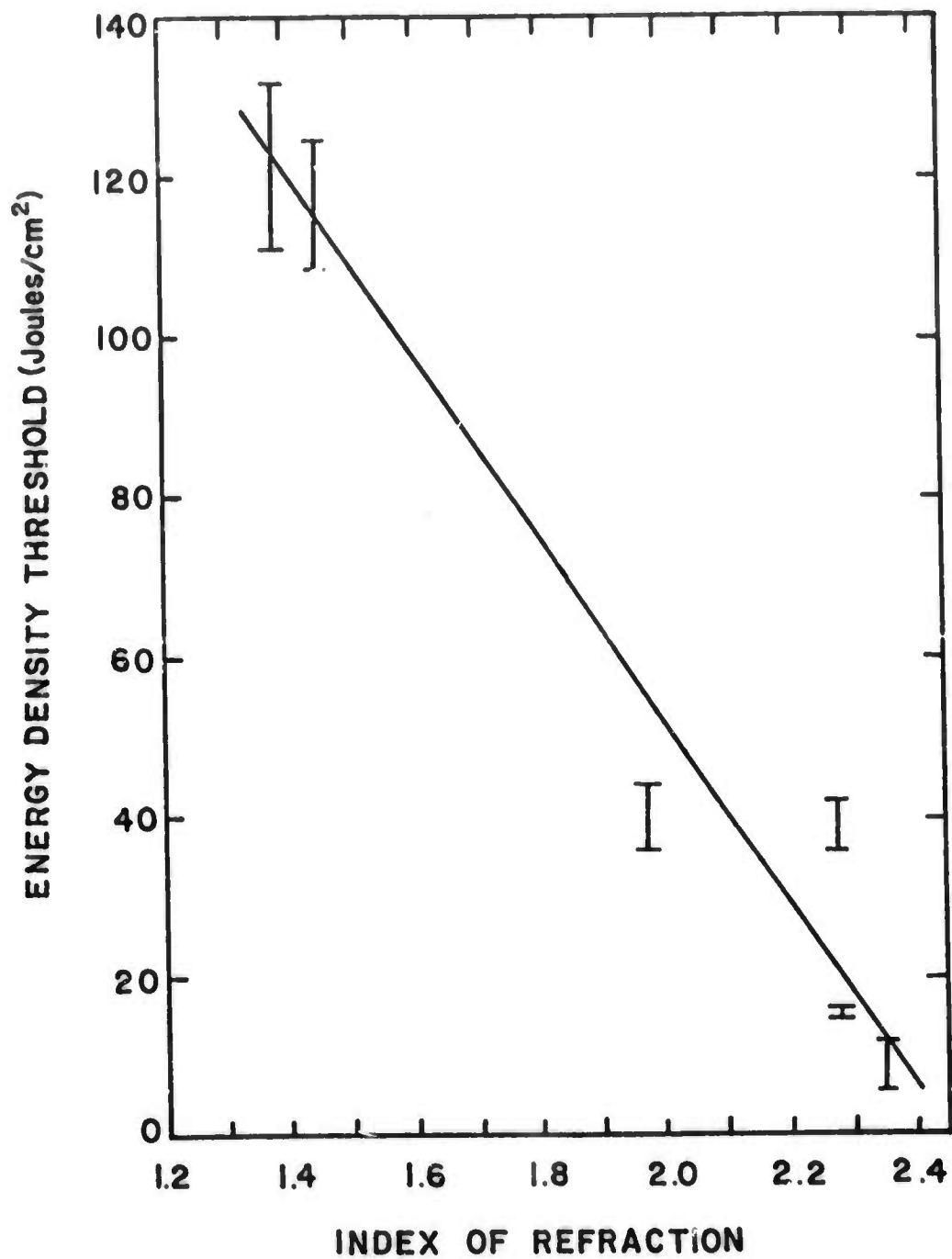
Figure 49.   Correlation of energy density damage threshold
with refractive index of film material.

b. Film Thickness

Table 12 gives the damage thresholds for various film
thicknesses. In particular, note the variation of the thresholds for
the three TiO_2 films. The damage threshold of the half-wave film
was about one-third that of the quarter and three-quarter-wave films.
Figure 50 calculated relative intensity distribution for these three film
thicknesses of TiO_2. For a high index film material, such as TiO_2,
between two lower index materials of air and glass, the net electric
field has an antinode at the rear or glass-film interface. This rear
reflected wave has an antinode(node) at the front or air-film interface
in the case of a half- (quarter) wave film. The higher net electric-
field at the front surface of the half-wave film may be the origin of
the lower damage threshold of the half-wave film. It is interesting
to note that the ratio of the intensities for the half and quarter-wave
films at the air-film interface is about three.

Further understanding of the thickness dependence may
be obtained by comparing the energy densities inside the films when
the incident laser energy was sufficient to cause threshold damage.
If differences in the electric fields in films of varied thicknesses were
sufficient to explain the damage threshold variations, then the internal
energy densities at the film depth most susceptible to damage should
be equal. For MgF_2 and SiO_2 the energy densities for quarter and half-
wave thicknesses are most closely matched at the maximum values.
For ZrO_2 and TiO_2 the values at the air-film interfaces are most
nearly equal. Still, except for SiO_2, half-wave energy densities at
the damage thresholds are lower than those of the quarter-wave.
Therefore, even when electric-field standing-wave intensities are taken
into account, thick films are still more susceptible to damage than
thin films.
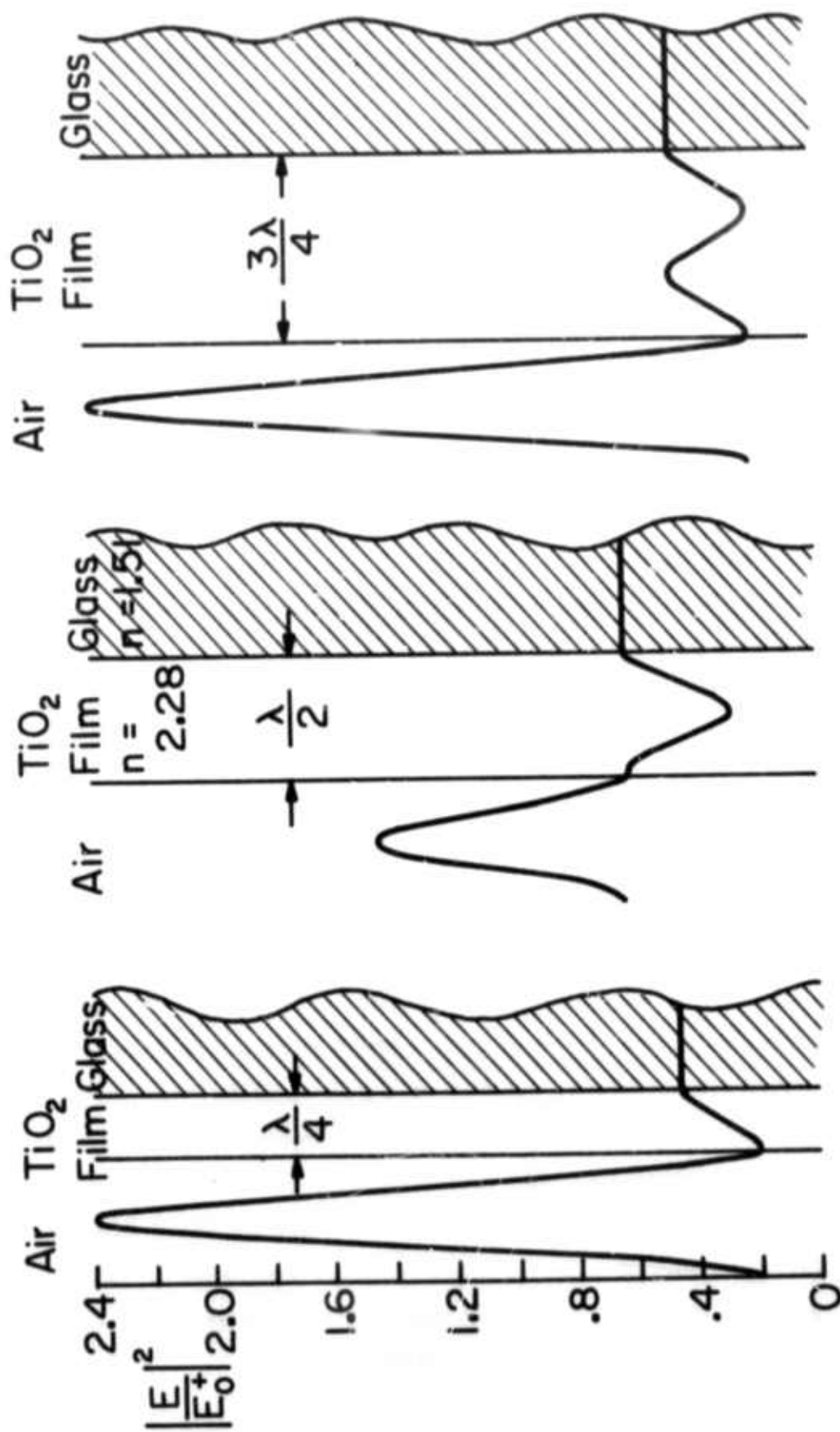
Figure 50. Relative intensity distributions for quarter-, half-, and three-quarter-wave TiO_2 films.

3. Bilayer Antireflection Coatings (V-coats)

The damage thresholds for bilayer antireflection coatings composed of each possible combination of the high-index materials, TiO_2 and ZrO_2, with the low-index materials, SiO_2 and MgF_2, are presented in Table 13. Like single-layer films, LIS was the most sensitive method of detecting damage. The laser parameters were essentially identical in each test, and the ZrO_2/SiO_2 coating was easily the most damage resistant. The damage thresholds of these coatings were generally midway between the threshold values of their component films. This observation was also made by Turner [4] for coatings composed of two quarter-wave films. It is known that the fracture strength of thin film is greater than that of thick films and the bulk material [13] For the bilayer coatings, the thicknesses of the high-index layers ranged from only 1/5 to 1/2 of a quarter-wave, and those of the low index layers were all about 1.3 quarter waves (see Table 6). This suggested an explanation to the fact why the V-coatings have much higher thresholds.

4. Multilayer Reflection Coatings

a. Film Materials

The damage thresholds of dielectric reflectors composed of multiple, quarter-wave films are listed in Table 14. Only the photoelectrically-detected, laser-induced spark thresholds were measured, because the initial weak-signal scatter of these coatings was suffi- ciently high to preclude sensitive LIS detection near the damage thres- holds. (Refer to Section III.5 for discussion on weak-signal scatter of multi-layer coatings). The reflectors are listed by their film mater- ial combinations beginning with the most damage-resistant types. Reflectors with the TiO_2/SiO_2 configuration had the highest thresholds, closely followed by the ZrO_2/MgF_2 combination.

Table 13. Damage thresholds for bilayer antireflection coatings[a, b]

Sample	Description	Peak energy density		Peak power density		Ratio of spark to LIS
		by spark	by LIS	by spark	by LIS	
		J/cm^2	J/cm^2	GW/cm^2	GW/cm^2	
O143	ZrO_2/SiO_2	118-147	97-118	8.6-11.7	7.6-9.5	1.2
O147	TiO_2/MgF_2	84-85	60-65	5.8-6.1	4.0-4.3	1.4
O145	ZrO_2/MgF_2	64-92	54-57	5.1-6.8	3.5-4.0	1.5
O142	TiO_2/SiO_2	74-98	35-42	6.5-6.8	2.4-3.1	2.3

[a] Sample configuration is GHLA, where G is BSC2 glass (0.5 mm thick), H is high index film (< $\lambda/4$ thick), L is low index film (> $\lambda/4$ thick), and A is air.

[b] Laser spot-size is 0.062 mm, and nominal pulsewidth is 11-14 nsec.

Table 14. Thresholds for multilayer reflectors (nominal pulsewidth: 12-15 nsec)

Sample	Description	Spot-size	Peak energy density	Peak power density
		mm	J/cm^2	GW/cm^2
O103	TiO_2/SiO_2	0.056	121-126	9.1-9.3
O104	"	0.056	107-127	6.1-8.9
[a]O104	"	0.056	97-118	7.6-8.7
O101	"	0.062	83-103	5.5-8.4
O102	"	0.060	98-110	6.8-7.2
S101	"	0.062	43-56	3.0-4.6
S102	"	0.062	50	3.7
O107	ZrO_2/MgF_2	0.058	81-113	4.7-7.8
O108	"	0.062	90	6.1
O105	ZrO_2/SiO_2	0.13	18-20	1.2-1.6
O106	"	0.13	18.5	1.3
S103	"	0.12	7.5	0.52
SS103	CeO_2/SiO_2	0.14	17-19	1.4
SS102	"	0.14	14.5-17	1.1-1.2
SS101	"	0.14	11.5	1.1
SS101	"	0.072	14.5-19	1.0-1.4
U111	ZnS/ThF_4	0.084	25-26	2.0-2.1

[a] Second test after $2\frac{1}{2}$ months.

As illustrated in Figures 28 and 29 in Section IV, the electric field intensities peak at the H-U interfaces. Therefore, for laser irradiation above threshold, damage involves removal of layers in pairs since the high-index films are less damage-resistant than the low-index films. This was previously pointed out by Turner [4]. For example, at the first peak in the electric field squared inside the best TiO_2/SiO_2 reflector, the energy density (J/cm^2) in the high index layer was 65% higher than in the low-index layer. Taken together with the higher absorption coefficient of the high-index film, sufficient thermal expansion could have occurred to have overcome the adhesive bond with resultant film rupture. Reflectors with TiO_2/SiO_2 configuration had the highest thresholds. Therefore, it was of interest to compare the damage resistance of reflectors of the same materials but with different numbers of layers. In Table 15, the spark thresholds of TiO_2/SiO_2 reflectors with 12 layers are compared with a 22-layer design. Also included for reference are the thresholds of single-layer and bilayer films of these materials. The reflectance of the 12-layer reflectors, 98.7%, was not much less than 99.9+% reflectance of the 22-layer design. The coating procedure, sample substrates, and laser parameters were the same for the samples listed. The thresholds of the 12-layer reflectors were about 10 to 15% less than those of the 22-layer reflectors. Furthermore, the reflector thresholds were greater than that of the single TiO_2 film and nearly the same as single SiO_2 films.

Table 15. Damage thresholds versus number of layers
of TiO_2 and SiO_2 films (nominal pulsewidth, 11-14 nsec).

Sample	Film materials	Number of layers	Order of layers[a]	Peak energy density by spark	by LIS
				J/cm^2	J/cm^2
O125	SiO_2, $\lambda/4$	1	GLA	>125	117
O127	SiO_2, $\lambda/2$	1	GL^2A	>111	>111
O121	TiO_2, $\lambda/4$	1	GHA	57-71	35-42
O142	TiO_2/SiO_2 (0, 28), (1, 320)) /4	2	$GH'L'A$	74-98	35-42
O109	TiO_2/SiO_2	12	$G(HL)^3HL^2A$	93-113	--
O110	"	12	"	100	--
O103	"	22	$G(HL)^{10}HL^2A$	121-126	--
O104	"	22	"	107-127	--
O104	"	22	"	97-118	--

[a] G: polished BSC2 glass substrate, L: low index film, $\lambda/4$ thick at 6943 Å, H: high index film, $\lambda/4$ thick at 6943 Å and A: air.

5. Damage Thresholds for Coatings on Various Substrates

The possible relationship of substrate material with thin film damage thresholds was investigated for quarter-wave ZnS films and multilayer reflectors of TiO_2/SiO_2. The results are given in Table 16. The ZnS films were deposited on cleaved NaCl crystals and polished BSC-2 glass substrates (samples U201, U202) using resistive-heating. ZnS films were also deposited on BSC-2 glass and polished spinel crystals (U203, U204, U301) by electron-gun evaporation. The thresholds for the ZnS films coated with the electron-gun probably should not be compared with those coated by resistive heating since these were the first films prepared with a new electron gun system. The thresholds for films on NaCl substrates were significantly higher

(by 40-80%) than for the glass substrates; likewise, the thresholds for films on spinel substrates had about 60% higher thresholds than films on glass. No significant differences in the thresholds of the TiO_2/SiO_2 reflectors on polished BSC-2 glass and microscope slides were measured.

Table 16. Damage thresholds for coatings on various substrates

Sample	Substrate description	Spot-size	Peak energy density[e]	Peak power density
Single layer of ZnS.λ/4 thick:		mm	J/cm^2	GW/cm^2
U101	Cleaved NaCl	0.14	17-17.5	1.3-1.4
U102	''	0.165	13-13.5	1.0-1.1
U201	Polished BSC2 glass	0.19	9.3-9.4	0.75-0.80
U202	''	0.19	9.6	0.80
U203		0.14	4.2-5.5	0.30-0.40
U204	'	0.14	3.6-4.1	0.25-0.35
''	''	0.25	3.2-3.8	0.25-0.35
U301	Polished spinel	0.25	5.0-6.1	0.40-0.50
Multilayer TiO_2/SiO_2 reflectors (99+%):				
O103	Polished BSC2 glass	0.056	121-126	9.1-9.3
O104	''	0.056	107-127	6.1-8.9
O111	Glass microscope slide	0.055	105-121	8.4-10.8
O112	''	0.058	95-116	7.9
		0.063		

[e] Thresholds determined by laser-induced scatter (LIS) for single layers and by photoelectric detection of spark emission for multilayers.

Considering substrates in general, there are at least five properties which can affect the film damage threshold: thermal diffusivity D, coefficient of thermal expansion α, optical absorptivity β, film adhesion A and surface preparation. For optimum damage resistance, D should be very large, α should be about equal to that of the adhering film, β should be negligible, A should be maximum, and the density of defects and absorption centers due to surface preparation

should be minimal. Cleaved NaCl crystals were expected to be better substrates than BSC-2 polished glass since NaCl has a thermal diffusivity six times larger than glass ($D = 33 \times 10^{\,?}$ cm^2/sec for NaCl compared to 5×10^{-3} cm^2/sec for glass). Both glass and NaCl have negligible absorption at 6943Å, but the thermal expansion coefficient of NaCl is $4 \times 10^{-5} \, ^0C^{-1}$ which is 3 to 6 times larger than that of several coating materials. BSC-2 glass is more suitable in this property with α equal to $6.5 \times 10^{-6} \, ^0C^{-1}$. Adhesion properties of glass are apparently satisfactory, but the adhesion of films to NaCl substrates is subject to its hygroscopic nature.

The comparable properties of spinel, a face-centered cubic crystal, should make it a better substrate than glass. In addition, it does not have the hygroscopic property like NaCl. The thermal diffusivity is high, $35 \times 10 \, cm^2$/sec and α is $7 \times 10^{-6} \, ^0C^{-1}$, similar to glass and the films. The surface of spinel is not as easily polished as glass, however, as indicated by the 90Å rms roughness specified by the manufacturer. A 15 to 20Å rms value is attainable on glass surfaces.

Because the damage thresholds of ZnS films on NaCl were relatively high despite its large thermal expansion coefficient, it is concluded that either thermal expansion is not an important consideration for Q-switched laser pulses, or that the advantages of a crystal substrate more than compensated for this high coefficient. In order to reach more specific conclusions, further study must be conducted on substrate materials.

6. Evaluation of Absorption as a Damage Mechanism

a. Calculation of Effective Absorption Coefficients

If absorption of a laser pulse causes damage by heating the film to its melting point, what value of the linear absorption coefficient β is required? This question can be answered by a simple

thermal analysis. The energy absorbed W per unit volume necessary to cause film melting is given by

$$ W = \rho \left[C_p (T_{mp} - 300^\circ K) + \Delta H \right], $$

where ρ, C_p, T_{mp}, and ΔH are the film density, specific heat, melting temperature and latent heat of fusion. Another expression for W in terms of the optical field of the laser beam is given by

$$ W(z) = \beta n \left| \frac{E(z)}{E_o^+} \right|^2 W_o \quad, $$

where W_o is assigned the value of the axial energy density at the damage threshold. By equating the two expressions and rearranging terms, the absorption coefficient at a distance z from the air-film surface necessary for melting the film is

$$ \beta(z) = \frac{\rho}{n W_o} \left[C_p (T_{mp} - 300^\circ K) + \Delta H \right] \left| \frac{E(z)}{E_o^+} \right|^{-2} \quad. $$

In this derivation, conduction of heat from the irradiated area was considered negligible during the 12-nsec laser pulses, since $(D\tau)^{\frac{1}{2}} \ll w_o$ for the thin films tested. Thermal radiation and convection losses were also assumed to be small during irradiation.

The physical and thermal properties of the film materials are listed in Table 17. The density ρ of thin films is equal to the packing fraction f times the bulk density ρ_b. The packing fraction can be determined from the formula [32]

$$ f = \frac{(n^2-1)(n_b^2+2)}{(n_b^2-1)(n^2+2)} \quad, $$

where n and n_b are the refractive indices of the film and the bulk material, respectively.

We can now calculate the absorption coefficients that would be required to cause melting of the films at the threshold laser intensities. Using the physical parameters given in Table 17, the threshold values W_o listed in Table 11 for single-layer films and the relative electric-field intensity distributions given in Section IV, these absorption coefficients were determined. The results of the calculation are given in Table 18. Since the electric fields vary with distance z, the absorption coefficient required for melting will vary with film depth.

Table 17. Physical and thermal properties of film materials

Material	Density ρ_b	Packing fraction, f	Specific heat, c_p	Melting temperature T_{mp}	Heat of fusion, ΔH
	gm/cm^3		$J/gm\text{-}^{o}K$	^{o}K	cal/gm
MgF_2	3.2	0.9	1.19	1528	94.7
SiO_2	2.32	0.93	0.73	2001	35.0
ZrO_2	5.60	0.89	0.44	2983	168.8
TiO_2	4.26	0.86	0.71	2093	142.7
ZnS	4.09	0.99	0.49	1293	93.3

Table 18. Summary of analysis of linear film absorption

Material	Calculated β to melt firm	Measured β	Published values of β
	cm^{-1}	cm^{-1}	cm^{-1}
MgF_2	40-55	< 100	- - - - -
SiO_2	25-30	< 100	< 10 [33]
ZrO_2	200-430	< 100	1350 [34]
TiO_2	160-420	100-500	< 40 [33] $\sim$ 1000 [35]
ZnS	270-1400	- - - - -	10-2000 [36]

b.   Measured Absorption at 6943Å

The calculated values of β are very much larger than those cited in the optics literature for bulk crystals in the visible spectrum (typically less than $1.0 \, cm^{-1}$). To determine if these high values were inherent film properties, the transmittance of half-wave films at 6943Å was measured with a Cary 14 spectrophotometer. Within the resolution of the instrument (0.1 - 0.2% in absorption), no absorption was apparent for the SiO_2, MgF_2 and ZrO_2 films. Minimal absorption was observed for TiO_2. A half-wave film of ZnS was not available at the time of measurement.

Abeles' formula [33] for weakly absorbing films was applied to these measurements to compute the absorption coefficient,

$$\beta = \frac{2}{d} \ \frac{n+n_s n}{n^2 + n_s} \ [(T_s / T)^{\frac{1}{2}} - 1] ,$$

where d is the film thickness in half-wavelength multiples, n and n_s are the refractive indices for the film and substrate, and T_s and T are the transmittances of the uncoated, nonabsorbing substrate

and coated substrate, respectively. Assuming that the spectrophoto-
meter resolution corresponded to the maximum possible absorption for
the films that indicated no absorption, β was calculated to be less than
100 cm^{-1} for MgF_2, SiO_2 and ZrO_2. For the TiO_2 film it was possible
for β to be between 100 to 500 cm^{-1}. The precision of the measure-
ments would have been improved if thicker films had been available
and an instrument with finer resolution had been used. These results
can be compared to those of Heitmann [33] who measured β to be less
than 10 cm^{-1} and 40 cm^{-1} at 6328 Å for fully oxidized films of SiO_2
and TiO_2. From previous measurements of ZnS films by Vlasenko [36],
the coefficient at 6943 Å was estimated to be between 100 and 2000 cm^{-1}
depending on the film annealing process. He found that ZnS films,
annealed at elevated temperatures, had increased absorption for wave-
lengths greater than 4000 Å. This may explain the results in which
the damage thresholds of ZnS deposited on heated substrates were much
lower than those with no heating.

c. Comments on Ultraviolet Resonance Absorption.

The absorption of a dielectric for visible wavelengths is
due to the tail of the fundamental absorption resonance in the ultra-
violet region. The theoretical relationship for the extinction coefficient
at a frequency ν_f of an absorption band is of the form

$$k = \frac{c\nu}{(\nu_f^2 - \nu^2)^2 + \nu_f^2 \nu^2}$$

This relation shows that nearer the resonance ν_f is to ν, the greater
the absorption will be. For ZnS the primary resonance is at 2150 Å,
but there is a secondary resonance at 3200 Å The resonance of TiO_2
occurs in the near-UV at 3200 Å, and for ZrO_2 it is at 2480 Å. For
MgF_2 and SiO_2, the absorption edge is below 2000 Å. For a CeO_2
film, the resonance was at 3000 Å with significant absorption extending

to 4600 Å at which k fell below 0.01. With the relative damage resis-
tance of these films in mind, it is apparent that the shorter the wave-
length for resonance, the greater the damage threshold. Acutally, this
statement is equivalent ot the correlation of threshold with refractive
index since n is related to k.

To verify that the thin film samples used in the damage
tests had no secondary absorption resonances between those given above
and the laser wavelength of 6943 Å, the absorption was measured from
3300 to 7000 Å with the Cary 14 spectropnotometer. These spectra for
three film materials are shown in Figure 51. By comparing with the
apparent absorbance of the uncoated glass substrate while taking into
account variations in standing-wave reflections and the index dispersion,
no other regions of absorption are discernible. The ZrO_2 and MgF_2
films are obviously far from their resonances, but the absorption of
TiO_2 increases drastically below 3800Å as the resonance of 3200 Å is
approached.

To further demonstrate the presence or absence of UV
absorption, a quarter-wave thick film of each material was exposed
to the UV emission (3371Å) of a pulsed nitrogen gas laser. The laser
emitted a nominal power of 100 kW (~10 nsec pulses at 100 pps)
which was focused on the samples with a 15 cm lens. No damage
occurred to the MgF_2, SiO_2, and ZrO_2 films, but the beam vaporized
the TiO_2 and ZnS films which have a large value of β at 3371 Å.

d. Conclusions on Linear Absorption

For some of the film materials the limited precision
of the β measurements prevents final conclusions; however, it is
possible to make some reasonable remarks. The possibility of linear
absorption being involved in laser-induced damage at the ruby wave-
length is greatest for the higher-index films. This is almost certain
for ZnS and likely for TiO_2. For MgF_2 and SiO_2, however, other
mechanisms such as nonlinear absorption at the high intensities
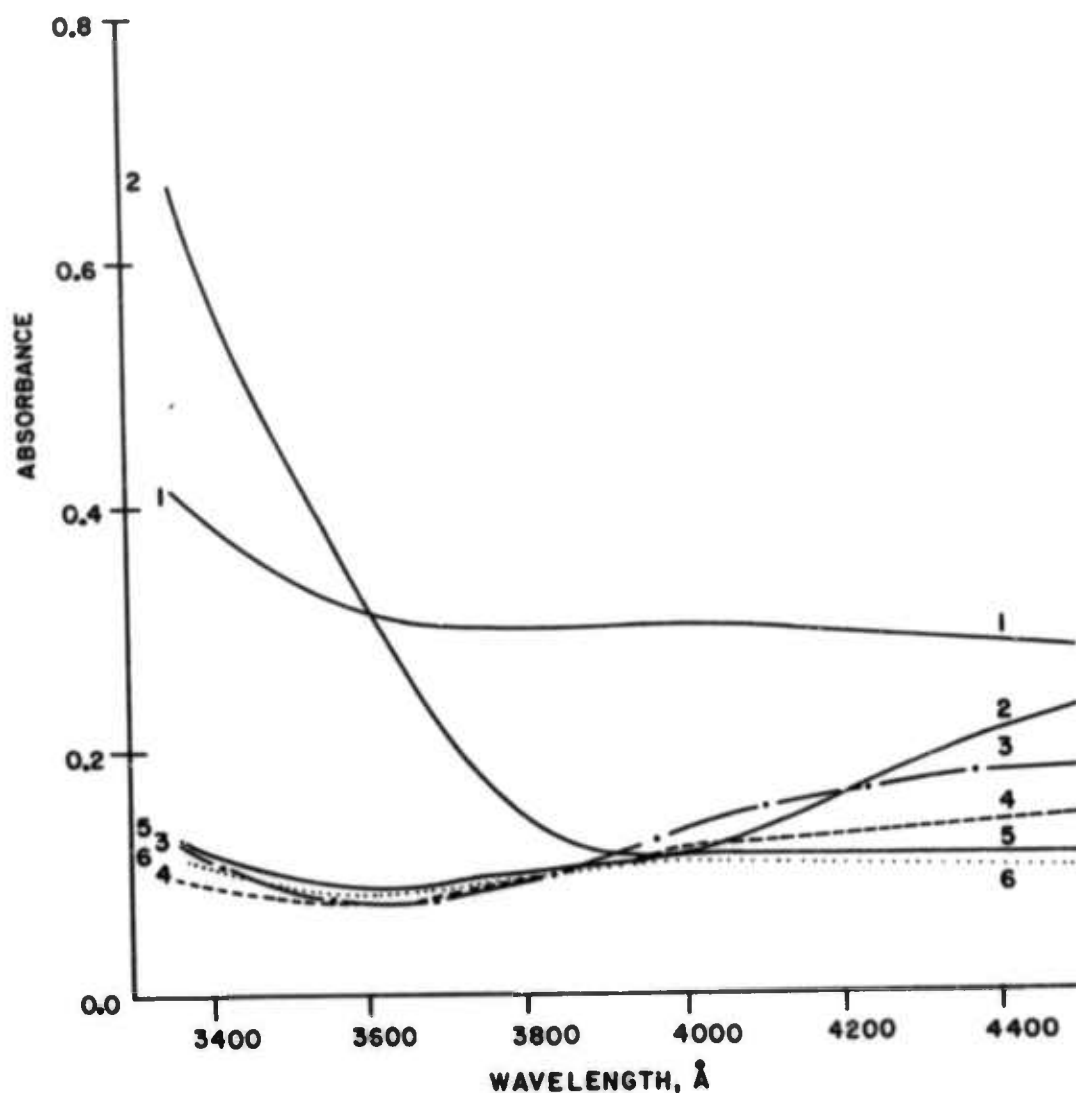
Figure 51.   Apparent absorbance due to absorption and reflection as measured with a Cary 14 spectrophotometer for single-layer films on glass substrates.   Films measured were:

(2) TiO_2 , half-eave thick

(3) ZrO_2 , half-wave thick

(4) ZrO_2 , quarter-wave thick

(5) BK-7 glass substrate

(6) MgF_2 , half-wave thick.

required for damage must be considered. A combination of both may be involved in the damage of ZrO_2 films. To reach definite conclusions regarding the role of linear absorption, measurements of the extinction coefficient more accurate than already obtained in this study would be required. It is not sufficient to use values of β or k published in the literature because film properties, including absorption, are affected significantly by the deposition technique. With some techniques, complete oxidation of the metal ions is not attained, and this deviation from stoichiometry (e.g. Ti, TiO, and Ti_2O_3 rather than TiO_2) results in increased absorption at these "impurity" defects.

7. Film Stresses (inherent and laser-induced)

There are many probable damage mechanisms. Some of the results had characteristics predicted by one or more of several damage mechanisms. For example, Figure 52 displays a damage site above spark threshold on a single quarter-wave thick film of MgF_2. The explanation of this morphology requires more careful analysis.

It is possible that the damage thresholds of thin films may be related to their net residual stresses which are established during the vacuum-deposition process and subsequent exposure to the atmosphere. Ennos [37] and Heitmann [33] have measured the residual stresses in a number of coatings including TiO_2, SiO_2, MgF_2, and ZnS. The stresses in TiO_2 and MgF_2 are tensile with magnitudes of 3×10^9 and 1×10^9 dynes/cm^2, respectively. Those of SiO_2 and ZnS are compressive with magnitudes of about 2×10^9 dynes/cm^2. The stresses in most other materials, including ZrO_2 are tensile. Stress compensation may be effected by proper pairing of films with compressive and tensile stresses. Since very thick films have been observed to cloud or crack without applying other external forces [38], it is apparent that, without compensation, the magnitudes of these stresses can be of the order of the fracture strengths. As a result, the magnitude of additional forces required to cause film rupture may
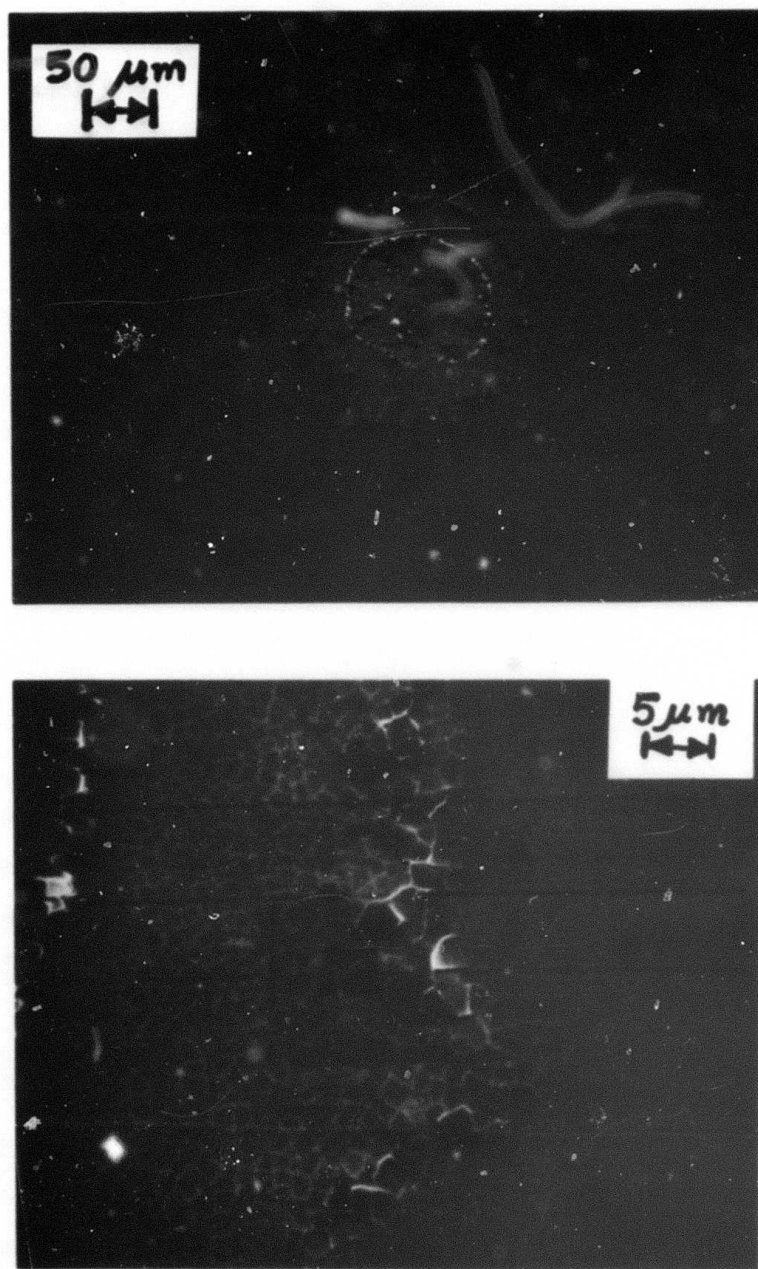
Figure 52.   Damage site on a single quarter-wave film of MgF_2
with (a) overall view of site having dimension of
150 microns diameter and (b) close-up view of the
far right region of the damage site.

be substantially modified.

Since the radial distribution of a laser beam is necessarily nonuniform, e.g. Gaussian, thermostrictive stresses result from film absorption. The temperature rise in the thin film due to absorption of a Gaussian beam is given by

$$\Delta T(r) = \Delta T_o e^{-2r^2/w^2} ,$$

and the resultant stress components for steady-state absorption are given by [39]

$$\sigma_r = -\alpha Y \Delta T_o \left(\frac{w}{2r}\right)^2 [1 - e^{-2r^2/w^2}] ,$$

and

$$\sigma_\theta = -\alpha Y \Delta T_o e^{-2r^2/w^2} \cdot \; _r$$

where α is the coefficient of linear expansion, and Y is Young's modulus. The radial stresses are compressive, whereas the azimuthal stresses are tensile. Although σ_r is always larger than σ_θ, the compressive strength of materials is much greater than the tensile strength (by a factor of 10 or more for glass, for example) [38].

Using a dynamic analysis of thermostriction, Sharma and Rieckhoff [40] determined that mechanical damage of the bulk of silicate glasses whould result from tensile stresses if the effective absorption coefficient was at least 50 cm^{-1}. (Surface damage would require a smaller coefficient). Recalling the large absorption coefficients listed in Table 18 postulated for film melting, it is reasonable that thermostrictive forces could also exceed the fracture strength of thin films with those values.

Electric surface stress, electrostriction, and radiation pressure are other laser-induced stresses which have been considered as possible causes of surface damage [41]. Using the theory of

Stratton [42], Kerr [41] derived an expression for the electric surface stress as

$$S = (n_o + n_o^3 P_{12} - 1/n_o) I/2c ,$$

where S is the pressure directed outwardly normal to the surface P_{12} is of the order of 0.25, I is the laser intensity (watts/cm^2), and c is the velocity of light. For a laser pulse with peak intensity of 10 GW/cm^2 (the maximum value measured for the most damage-resistant coating), the electric stress is equal to 5 atmospheres. This is quite small when compared to the value required to damage glass ($\sim$100 atm) [40]. Radiation pressure and electrostriction within a film would be even lower.

VIII.   SUMMARY AND CONCLUSIONS

Using a single transverse and longitudinal TEM_{00}, Q-switched ruby laser, damage phenomena have been studied in dielectric thin-film systems.   This study included single-, bi-, and multi-layered vacuum-deposited coatings of the materials MgF_2, SiO_2, ZrO_2, TiO_2, ZnS and others on substrates of glass, fused silica, rock salt, and spinel.   Damage thresholds were measured using spark detection system, LIS technique and microscope as a function of many parameters of the laser beam and the coatings. Major experimental results are summarized in the following:

1.   The damage thresholds of thin-film systems, as detected by increased scattering of a He-Ne gas laser (LIS) occurred before or at the spark formation detectable by sensitive photoelectronics.   The presence of a spark gives a very characteristic and unmistakable damage morphology on the coatings.   The LIS technique was most sensitive for detecting damage on single- and bi-layered coatings.   Using the indication of the weak-signal scatter level of an attenuated ruby beam, the damage thresholds were generally higher for multilayer reflectors with the least scattering. Time-resolved measurements of scatter (a He-Ne probe beam) have shown that the thin film damage occurred within the ruby pulsewidth of 20 nsec.

2.   The damage thresholds of thin films were strongly dependent on the standing-wave patterns of the internal electric fields. The entrance-face thresholds were equal to or greater than the exitface thresholds of thin films.   Calculation of the electric-field distribution in thin-film systems was essential to the analysis of damage processes.

100.

3. In correlating the damage thresholds to laser
parameters, one of the important results of this study is that the
damage threshold of the thin film increases as the spot-size of the
laser beam decreases. A simple model has been developed in
correlating the nature and distribution of coating defects to this spot-
size dependence. It has been demonstrated that this is a good model:
the probability of the laser beam striking a defect site is greater for
larger spot-sizes while damage in materials can be distinguished as
defect damage and intrinsic damage.

4. The damage thresholds of coatings irradiated by
a multimode laser were significantly less than by a single-mode laser.
For 10 to 30 nsec laser pulses, energy density rather than power
density was the more proper measure of the damage threshold. The
energy-density threshold for a ZrO_2 film increased with increasing
pulsewidth, but less than that giving a constant power-density threshold.

5. For single-layer dielectric coatings, the damage
thresholds were inversely proportional to refractive indices of the
materials. MgF_2 had the highest damage resistance among all
tested samples. The damage thresholds of half-wave thick films,
except SiO_2, were less than those of quarter-wave films, in good
agreement with electric field predictions at the air-film interface.

6. Thresholds of multi-layer coatings with high damage
resistance were much larger than the thresholds of the low-index
component films and less than or equal to the thresholds of the high-
index components.

7. Damage thresholds of single-layer ZnS films on
crystalline substrates (cleaved NaCl and polished spinel) were greater
than on polished glass substrates.

The analysis indicated that significant linear absorption could raise the film temperature to the melting point or high enough for thermostrictive forces to exceed the tensile fracture strength of the thin films. For high-index films, such as ZnS, linear absorption appeared to be the probable mechanism. However, it was not evident that the thresholds of low-index films, such as MgF_2 or SiO_2, were established by linear absorption. The spot-size effect suggested that local coating defects are playing an important role in the damage processes. Using the defect model, further studies on the parameter of enhancement factor η, and hence either the intrinsic damage threshold I_i or the defect damage threshold I_d, of the materials will uncover one or more of the damage mechanisms in the dielectric thin-film systems. For other laser wavelengths of interest, such as $1.06\mu m$ and $10.6\mu m$, the role of local defects via the spot-size dependence should be explored.

APPENDIX A

CALCULATION OF ELECTRIC FIELDS IN
THIN FILM COATINGS

The configuration of the thin film layers, and the notation to be used in calculations of the electric fields are presented in Figure 53. As shown, the fields and interfaces are numbered starting from the surface nearest the incident wave. For the convenience of the readers, two computer programs (in BASIC language) are included at the end of the Appendix. The square of the absolute values of the electric fields for different cases are summarized in the following:

1. Single Layer Coatings

a. Normal Incidence

$$|E_0 / E_0^+|^2 = (A^2 + B^2) / |D|^2 , \tag{A.1}$$

$$|E_1 / E_0^+|^2 = t_1^2 [1 + r_2^2 + 2r_2 \cos 2 (\delta_1 - k_1 z)] / |D|^2 , \tag{A.2}$$

$$\text{and} \quad |E_2 / E_0^+|^2 = t_1^2 t_2^2 / |D|^2 , \tag{A.3}$$

where $A = (1+r_2) [\cos(\delta_1 - k_0 z) + r_1 \cos(\delta_1 + k_0 z)]$,

$$B = (1-r_2) [\sin(\delta_1 - k_0 z) + r_1 \sin(\delta_1 + k_0 z)] ,$$

$$|D|^2 = 1 + r_1^2 r_2^2 + 2r_1 r_2 \cos 2\delta_1 .$$
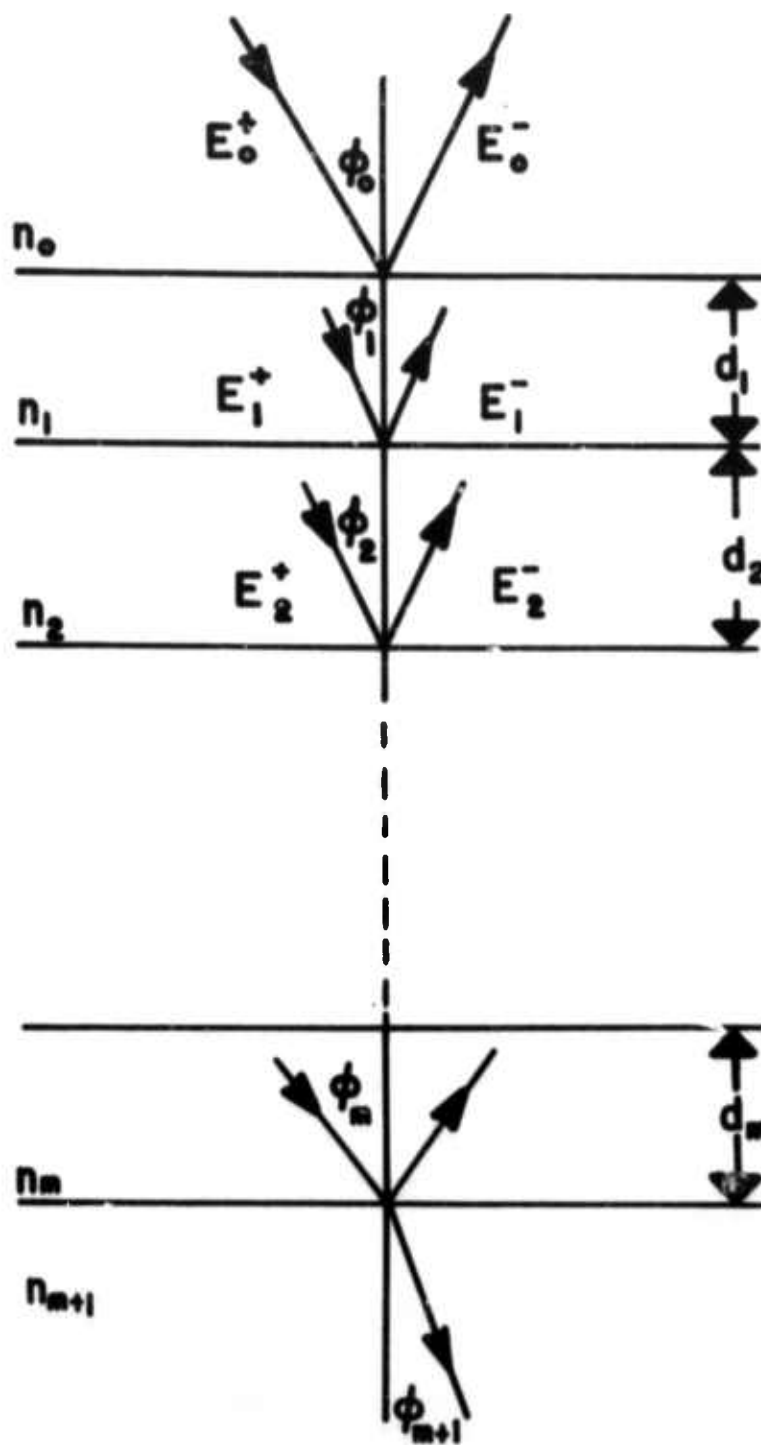
Figure 63. Multilayer thin film coating configuration and notation for electric field calculations.

b. Non-normal Incidence

For example, p-polarization is given here

$$|E_o/E_o^+|^2 = (A^2 + B^2) \ / \ |D|^2 \quad , \tag{A.4}$$

$$|E_1/E_o^+|^2 = t_1^2 \ [1 + r_2^2 + 2r_2 \cos(2k_1z - 2\delta_1 + \pi)] \ / \ n_1^2 \ |D|^2 \tag{A.5}$$

$$\text{and} \quad |E_2/E_o^+|^2 = t_1^2 \ t_2^2 \ / \ n_2^2 \ |D|^2 \quad , \tag{A.6}$$

where $A = (1 + r_2) [\cos(\delta_1 - k_o z - \pi) + r_1 \cos(\delta_1 + k_o z + \pi)]$,

$$B = (1 - r_2) [\sin(\delta_1 - k_o z - \pi) + r_1 \sin(\delta_1 + k_o z + \pi)] \quad ,$$

and $|D|^2 = 1 + r_1^2 r_2^2 + 2r_1 r_2 \cos 2\delta_1$.

with different Fresnel coefficients as

$$r_m = n_m \cos \phi_{m-1} - n_{m-1} \cos \phi_m \ / \ n_m \cos \phi_{m-1} + n_{m-1} \cos \phi_m \ , \tag{A.7}$$

and

$$t_m = 1 + r_m = 2n_m \cos \phi_{m-1} \ / \ n_m \cos \phi_{m-1} + n_{m-1} \cos \phi_m \tag{A.8}$$

2. Bilayer Antireflection Coatings

In the first layer, we obtain

$$|E_1/E_o^+|^2 = (G^2 + H^2) \ / \ (E^2 + F^2) \quad , \tag{A.9}$$

where

$$G = t_1 [\cos k_1 z + r_2 r_3 \cos(2\delta_2 + k_1 z) + r_2 \cos(2\delta_1 - k_1 z)$$

$$+ r_3 \cos(2\delta_1 + 2\delta_2 k_1 z)] \quad ,$$

$$H = t_1 \left[\sin k_1 z + r_2 r_3 \sin(2\delta_2 + k_1 z) + r_2 \sin(2\delta_1 - k_1 z) \right.$$

$$\left. + r_3 \sin(2\delta_1 + 2\delta_2 - k_1 z) \right].$$

$$E = 1 + r_1 r_2 \cos 2\delta_1 + r_1 r_3 \cos 2(\delta_1 + \delta_2) + r_2 r_3 \sin 2\delta_2 \quad,$$

$$F = r_1 r_2 \sin 2\delta_1 + r_1 r_3 \sin 2(\delta_1 + \delta_2) + r_2 r_3 \sin 2\delta_2 \quad,$$

The respective fields in the second layer and in the substrate are

$$|E_2 / E_o^+|^2 = t_1^2 t_2^2 (1 + r_3^2 + 2r_3 \cos 2(\delta_2 - k_2 z) / (E^2 + F^2) \tag{a.10}$$

and

$$|E_3 / E_o^+|^2 = t_1^2 t_2^2 t_3^2 / (E^2 + F^2). \tag{A.11}$$

3. Multilayer Reflectors

Electric field distributions for multilayer reflectors were computed by the matrix method for normal incidence. Such reflectors are usually composed of alternating layers of two materials with different refractive indices. For quarter-wavelength thick films, $n_m d_m = \lambda_o / 4$, so $\delta_m = k_m d_m = 1/2\pi$, except $\delta_o = 0$ as before. The matrix relation for the electric field wave amplitudes at the boundary of the (m-1)th and the mth layers is

$$\begin{pmatrix} E_{m-1}^+ \\ \\ \\ E_{m-1}^- \end{pmatrix} = \frac{i}{t_m} \begin{pmatrix} 1 & r_m \\ \\ -r_m & -1 \end{pmatrix} \begin{pmatrix} E_m^+ \\ \\ \\ E_m^- \end{pmatrix} \tag{A.12}$$

where $0 < m < M+1$ and M is the total number of layers. For the incident medium, $m=0$, so $\delta_0 = 0$ and

$$\begin{pmatrix} E_o^+ \\ \\ E_o^- \end{pmatrix} = \frac{1}{t_1} \begin{pmatrix} 1 & r_1 \\ \\ r_1 & 1 \end{pmatrix} \begin{pmatrix} E_1^+ \\ \\ E_1^- \end{pmatrix} \qquad . \tag{A.13}$$

For the substrate, $m = M+1$, in which there is no reflected wave, i.e., $E_{M+1}^- = 0$, so that

$$E_M^+ = (i/t_{M+1}) E_{M+1}^+ \tag{A.14}$$

and $\qquad E_M^- = - (i r_{M+1} / t_{M+1}) E_{M+1}^+ \tag{A.15}$

To evaluate E_M^+ including E_o^+ by computer, it was necessary to set E_{M+1}^+ equal to a constant number. When the resultant numerical value of the incident field E_o^+ was determined, E_m^+ and E_{M+1}^+ were then properly normalized by division by E_o^+. As in the preceding cases, the electric fields within each layer are given by

$$E_m = E_m^+ e^{-ik_m z} + E_m^- e^{+ik_m z}$$

which, for the present case, yields

$$E_m = (i/t_{m+1}) \left[E_{m+1}^+ (e^{-ik_m z} - r_{m+1} e^{+ik_m z}) \right.$$
$$\left. + E_{m+1}^- (r_{m+1} e^{-ik_m z} - e^{+ik_m z}) \right] \tag{A.16}$$

If a half-wave thick film is used for the first layer, which is a common practice, it may be treated as two adjacent quarter-wave thick films.

Program 1   MULFIL: Calculation of the Electric Field Intensity Distribution for Light Incident Upon a Multilayer Coating of N Quarter-Wave Thick Films

109.

```
LOAD (MULFIL)
?LIST
  10.              DECLARE  N CONTROLLED , A CONTROLLED , B CONTROLLED ;
  20.              IF ALLOCA(N)  THEN FREE N;
  30.              IF ALLOCA(A)  THEN FREE A;
  40.              IF ALLOCA(B)  THEN FREE B;
  50.              GET LIST(M);
  60.              ALLOCATE N(M),A(M),B(M);
  70.              GET LIST(N);
  80.              LET R(I)=(N(I-1)-N(I))/(N(I-1)+N(I));
  90.              B(M)=0;
 100.              A(M)=1;
 110.              LET C(I)=A(I)/A(1);
 120.              LET D(I)=B(I)/A(1);
 130.    LOOP1:    DO I=1 TO M-2;
 140.              A(M-I)=(A(M+1-I)+R(M+1-I)*B(M+1-I))/(1+R(M+1-I));
 150.              B(M-I)=-(A(M+1-I)*R(M+1-I)+B(M+1-I))/(1+R(M+1-I));
 160.              END ;
 170.              A(1)=(A(2)+R(2)*B(2))/(1+R(2));
 180.              B(1)=(A(2)*R(2)+B(2))/(1+R(2));
 190.              LET ES1(I)=(C(I)+D(I))**2;
 200.              LET ES2(I)=C(I)**2+D(I)**2+2*C(I)*D(I)*COSD(30);
 210.              LET ES3(I)=C(I)**2+D(I)**2+2*C(I)*D(I)*COSD(60);
 220.              LET ES4(I)=C(I)**2+D(I)**2;
 230.              LET ES5(I)=C(I)**2+D(I)**2+2*C(I)*D(I)*COSD(120);
 240.              LET ES6(I)=C(I)**2+D(I)**2+2*C(I)*D(I)*COSD(150);
 250.              LET ES7(I)=(C(I)-D(I))**2;
 260.              PUT LIST('');
 270.              PUT LIST('    E. FIELD SQUARE IN I-TH MEDIUM');
 280.              PUT LIST('');
 290.              PUT EDIT(1,ES7(1),ES6(1),ES5(1),ES4(1),ES3(1),ES2(1),ES
(1))(F(2),F(8,3),F(8,3),R(8,3),F(8,3),F(8,3),F(8,3),F(8,3));
 300.    LOOP2:    DO I=2 TO M-1;
 310.              PUT EDIT(I,ES1(I),ES2(I),ES3(I),ES4(I),ES5(I),ES6(I),ES
(I))(F(2),F(8,3),F(8,3),F(8,3),F(8,3),F(8,3),F(8,3),F(8,3));
 320.              END ;
 330.              PUT EDIT(M,ES1(M))(F(2),F(8,3));
 340.              LET NES1(I)=N(I)*ES1(I);
 350.              LET NES2(I)=N(I)*ES2(I);
 360.              LET NES3(I)=N(I)*ES3(I);
 370.              LET NES4(I)=N(I)*ES4(I);
 380.              LET NES5(I)=N(I)*ES5(I);
 390.              LET NES6(I)=N(I)*ES6(I);
 400.              LET NES7(I)=N(I)*ES7(I);
 410.              PUT LIST('');
 420.              PUT LIST('    N*E. FIELD SQUARE IN I-TH MEDIUM');
 430.              PUT LIST('');
 440.              PUT EDIT(1,NES7(1),NES6(1),NES5(1),NES4(1),NES3(1),NES2
1),NES1(1))(F(2),F(8,3),F(8,3),F(8,3),F(8,3),F(8,3),F(8,3),F(8,3));
 450.    LOOP3:    DO I=2 TO M-1;
 460.              PUT EDIT(I,NES1(I),NES2(I),NES3(I),NES4(I),NES5(I),NES6
1),NES7(I))(F(2),F(8,3),F(8,3),F(8,3),F(8,3),F(8,3),F(8,3),F(8,3));
 470.              END ;
 480.              PUT EDIT(M,NES1(M))(F(2),F(8,3));
?
```

Program 2   VCOAT: Calculation of the Electric
Field Intensity Distribution for Light Incident
Upon a Bilayer Antireflection Coating

```
 LOAD (VCOAT)
?LIST 10 THRU 246
  10.            GET LIST(N0,N1,N2,N3,Q1,Q2,D1,D2);
  20.            R1=(N0-N1)/(N0+N1);
  30.            R2=(N1-N2)/(N1+N2);
  40.            R3=(N2-N3)/(N2+N3);
  50.            T1=1+R1;
  60.            T2=1+R2;
  70.            T3=1+R3;
  80.            E=1+R1*R2*COSD(2*Q1)+R1*R3*COSD(2*Q1+2*Q2)+R2*R3*COSD(2
Q2));
  90.            F=R1*R2*SIND(2*Q1)+R1*R3*SIND(2*Q1+2*Q2)+R2*R3*SIND(2*Q
);
 100.            D=E**2+F**2;
 110.            LET EFS0(Z)=(A(Z)**2+B(Z)**2)/D;
 120.            LET A(Z)=(1+R1)*COSD(K0*Z)+R1*R2*COSD(2*Q1-K0*Z)+R1*R3*
OSD(2*Q1+2*Q2-K0*Z)+R2*R3*COSD(2*Q2-K0*Z)+R2*COSD(2*Q1+K0*Z)+R3*COSD(2*Q
+2*Q2+K0*Z)+R1*R2*R3*COSD(2*Q2+K0*Z));
 130.            LET B(Z)=(R1-1)*SIND(K0*Z)+R1*R2*SIND(2*Q1-K0*Z)+R1*R3*
IND(2*Q1+2*Q2-K0*Z)+R2*R3*SIND(2*Q2-K0*Z)+R2*SIND(2*Q1+K0*Z)+R3*SIND(2*Q
+2*Q2+K0*Z)+R1*R2*R3*SIND(2*Q2+K0*Z);
 140.            LET EFS1(Z)=(G(Z)**2+H(Z)**2)/D;
 150.            LET G(Z)=T1*(COSD(K1*Z)+R2*R3*COSD(2*Q2+K1*Z)+R2*COSD(2
Q1-K1*Z)+R3*COSD(2*Q1+2*Q2-K1*Z));
 160.            LET H(Z)=T1*(SIND(K1*Z)+R2*R3*SIND(2*Q2+K1*Z)+R2*SIND(2
Q1-K1*Z)+R3*SIND(2*Q1+2*Q2-K1*Z));
 170.            LET EFS2(Z)=(T1*T2)**2*(1+R3**2+2*R3*COSD(2*Q2-2*K2*Z))
D;
 180.            EFS3=(T1*T2*T3)**2/D;
 190.            L=.6943;
 200.            K0=360*N0/L;
 210.            K1=360*N1/L;
 220.            K2=360*N2/L;
 230.            K3=360*N3/L;
 235.            PUT LIST(' ');
 238.            PUT IMAGE(E,F,D)(IM1);
 240.    IM1:    IMAGE;
     E = -.-----        F = --.-----        D = -.-----
 242.            PUT LIST(' ');
 244.            PUT LIST('   Z         N*Z           E. FIELD SQ.      N*
. FIELD SQ.');
                              E
 246.            PUT LIST('                      MEDIUM NO');
?
```

VCOAT--Continued

```
LIST 250 THRU 580
  250.      LOOP1:   DO Z=0 TO .34715 BY .034715/NO
  260.               AA=A(Z);
  270.               BB=B(Z);
  280.               ESO=EFSO(Z);
  290.               NOESO=NO*EFSO(Z);
  300.               NOZ=NO*Z*4/L;
  310.               PUT EDIT(Z,NOZ,ESO,NOESO)(F(6,4),X(6),F(6,4),X(11),F(6,
),X(12),F(6,4));
  320.               END ;
  325.               PUT LIST(' ');
  328.               PUT LIST('              MEDIUM N1');
  330.      LOOP2:   DO Z=0 TO D1 BY D1/10;
  340.               GG=G(Z);
  350.               HH=H(Z);
  360.               ES1=EFS1(Z);
  370.               N1ES1=N1*EFS1(Z);
  380.               N1Z=N1*Z*4/L;
  390.               PUT EDIT(Z,N1Z,ES1,N1ES1)(F(6,4),X(6),F(6,4),X(11),F(6,
),X(12),F(6,4));
  400.               END ;
  405.               PUT LIST(' ');
  408.               PUT LIST('              MEDIUM N2');
  410.      LOOP3:   DO Z=0 TO D2 BY D2/5;
  420.               ES2=EFS2(Z);
  430.               N2ES2=N2*EFS2(Z);
  440.               N2Z=N2*Z*4/L;
  450.               PUT EDIT(Z,N2Z,ES2,N2ES2)(F(6,4),X(6),F(6,4),X(11),F(6,
),X(12),F(6,4));
  460.               END ;
  470.               PUT LIST(' ');
  480.               PUT LIST('              MEDIUM N3');
  490.               N3EFS3=N3*EFS3;
  500.               PUT EDIT(EFS3,N3EFS3)(X(29),F(6,4),X(12),F(6,4));
  510.               PUT LIST(' ');
  520.               T=N3EFS3;
  530.               PUT LIST('              TRANSMITTANCE,T');
  540.               PUT IMAGE(T)(IM2);
  550.      IM2:     IMAGE;
                          T = -.----
  560.               PUT LIST(' ');
  570.               PUT LIST(' ');
  580.               END ;
?
```

REFERENCES

1. B. E. Newman and L. G. DeShazer, in <u>Damage in Laser Materials: 1971</u>, edited by A. J. Glass and A. H. Guenther (NBS Special Publication 356, 1971), pp. 113-118.

2. L. D. Dickson, Appl. Opt. <u>9</u>, 1854 (1970).

3. G. L. McAllister, M. M. Mann and L. G. DeShazer, IEEE J. Quan. Elect. <u>QE-6</u>, 44 (1970).

4. A. F. Turner, in <u>Damage in Laser Materials: 1971, op. cit.</u>, pp. 119-123.

5. J. P. Campbell and L. G. DeShazer, J. Opt. Soc. Am. <u>59</u>, 1427 (1969).

6. D. A. Holmes, J. E. Korka and P. V. Avizonis, Appl. Opt. <u>11</u>, 565 (1972).

7. J. H. Parks and N. Alyassini, in <u>Laser induced Damage in Optical Materials: 1972</u>, edited by A. J. Glass and A. H. Guenther (NBS Special Publication 372, October 1972), pp. 104-107.

8. O. S. Heavens, <u>Optical Properties of Thin Solid Films</u> (Dover, New York, 1965), Chapter 4.

9. L. P. Mott, OCLI, private communication, 1971. Index measurements were made on single layer films studied in this research project.

10. "Vactron Vacuum Evaporation Materials", Gallard-Schlesinger Chemical Manufacturing Corp., data brochure (1972).

11. T. S. Travina and Yu. A. Mukhin, Sov. Phys. J. <u>9</u>, 40 (1966).

12. A. J. Moses, <u>Optical Materials Properties</u> (IFI/Plenum, New York, 1971).

13. "Catalog of Precision Optical Components", Oriel Optics Corporation, 1970.

14. D. E. Gray, editor, <u>American Institute of Physics Handbook</u> (McGraw-Hill, New York, 1963).

15. "Crystal Products Bulletins: Spinel and YAG", Union Carbide Corporation, San Diego, California, 1972.

References (Continued)

16. J. T. Cos and G. Hass, in Physics of Thin Films, vol. 2, edited by G. Hass and R. E. Thun (Academic Press, New York, 1964), p. 257.

17. L. A. Catalan, J. Opt. Soc. Am. 52, 437 (1962).

18. M. D. Crisp, N. L. Boling and G. Dube, Appl. Phys. Lett. 21, 364 (1972).

19. I. A. Fersman and L. D. Khazov, Soc. Phys. - Tech. Phys. 15, 834 (1970).

20. H. Dupont, A. Donzel and J. Ernest, Appl. Phys. Lett. 11, 271 (1967).

21. C. R. Giuliano, IEEE J. Quantum Electron, QE-8, 749 (1972).

22. N. Bloembergen, Appl. Opt. 12, 661 (1973).

23. D. W. Fradin, E. Yablonovitch and M. Bass, Appl. Opt. 12, 700 (1973).

24. "R" stands for "Rayleigh distance," which is defined as $2a^2/\lambda$ where a is the aperture radius. It is the characteristic distance associated with aperture diffraction. Diffraction at 1R from the aperture locates the pattern in the transition region between the near and far fields.

25. The time-dependent emission of the ruby laser oscillator with Fresnel number of 8.0 was computed for this study by G. L. McAllister using the computation scheme reported by G. L. McAllister, M. M. Mann and L. G. DeShazer, IEEE J. Quan. Elect. QE-6, 44 (1970).

26. T. Izamitani, K. Hosaka and C. Yamanaka, in Laser Induced Damage in Optical Materials: 1972, edited by A. J. Glass and A. H. Guenther (NBS Special Publication 372, October 1972), pp. 3-10.

27. M. Bass, Damage in Laser Materials. edited by A. J. Glass and A. H. Guenther (NBS Special Publication 341, December 1970), pp. 90-96.

28. V. G. Draggoo, C. Y. She, G. L. McAllister and D. F. Edwards, IEEE J. Quan. Elect. 8, 54 (1972).

29. E. S. Bliss and D. Milam, in Damage in Laser Materials: 1972, op. cit., to be published.

References (Continued)

30. E. S. Bliss, in Damage in Laser Materials, op. cit., pp. 105-117.

31. L. I. Maissel and R. Glang, op. cit., p. 12-43.

32. G. Bauer, Ann. Phys. 19, 434 (1934).

33. W. Heitmann, Appl. Opt. 10, 2685 (1971).

34. M. Ruiz-Urbieta, E. M. Sparrow and E. R. G. Eckert, J. Opt. Soc. Am. 61, 351 (1971).

35. W. Heitmann, App. Opt. 10, 2414 (1971).

36. N. A. Vlasenko, Opt. and Spec. 7, 320 (1959).

37. A. E. Ennos, Appl. Opt. 5, 51 (1966).

38. L. I. Maissel and R. Glang, Handbook of Thin Film Technology (McGraw-Hill, New York, 1970), p. 12-36.

39. C. T. Wang, Applied Elasticity, (McGraw-Hill, New York, 1953), pp. 70-74.

40. B. S. Sharma and K. E. Rieckhoff, Can. J. Phys. 48, 1178 (1970).

41. E. L. Kerr, IEEE J. Quantum Electron, QE-8, 723 (1972).

42. J. A. Stratton, Electromagnetic Theory, (McGraw-Hill, New York, 1941), pp. 137-151.